Politecnico di Milano

SCHOOL OF INDUSTRIAL AND INFORMATION ENGINEERING
Master of Science – Nuclear Engineering

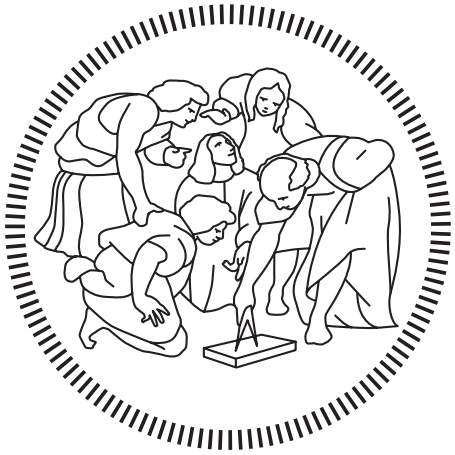

Thermally Rechargeable Supercapacitors

Supervisor
Prof. Roberto Piazza

Co-Supervisor
Prof. René Van Roij

Candidate
PIERFRANCESCO OMBRINI – 913413

Academic Year 2020 – 2021

Questa tesi è stata realizzata durante la pandemia di Covid-19, un momento difficile per tutti. La dedico quindi a tutti coloro i quali mi sono stati "vicino" durante questo periodo, permettendomi di rimanere sereno e di svolgere il lavoro con dedizione ed attenzione.
Ringrazio i miei relatori, il professor Robero Piazza e il professor René van Roij, per l'opportunità, per la libertà concessa nel seguire quello che più mi interessava e per gli indispensabili consigli.
Ringrazio la mia famiglia, non solo per questa tesi, ma sopprattuto per il supporto in questi (quasi) sei anni di studi.
Un grazie va anche agli amici che hanno riso su i miei sguardi nel vuoto di quando stavo pensando alle soluzioni.
Grazie a tutti quelli che mi hanno permesso di rispondere a "Come va la tesi ?" con "Dai, alla fine tutto bene"

"La vocazione dell'uomo di scienza è di spostare in avanti le frontiere della nostra conoscenza in tutte le direzioni, non solo in quelle che promettono più immediati compensi o applausi."

Enrico Fermi

Abstract

The aim of this Thesis Work is to understand the behaviour of a supercapacitor subjected to a temperature gradient and the way in which this gradient can be used to charge the supercapacitor. The application of a temperature gradient to an electrolyte generates a drift motion of the ions, the cations and the anions having different thermal responses, a charge unbalance is generated and consequently a potential difference can be measured. This effect can be used to exploit a temperature difference to charge an electrode-electrolyte system, such as a battery or a supercapacitor. The origin of the ion's thermal drift are not completely clear as well as the inner mechanisms that take place during the thermal charging of a supercapacitor.
Different theoretical approaches can be applied to study these phenomena, but the restricted literature present on this topic coerces to use simple methods, in order to compare the results to physical intuition. More profound knowledge of these systems could help in the development of better thermal energy conversion devices, which exploit low-temperature heat waste to produce carbon-free electrical energy.
In this Thesis Work, I have analysed the thermal charging of a supercapacitor with analytical calculations, numerical simulations and equivalent circuits. Different approximations were made in order to describe a complex three-dimensional system, such it is a supercapacitor, with a computationally fast and conceptually effective one-dimensional model.
The capacity and charging dynamics of a thermally rechargeable supercapacitor were theoretically explained. In particular, surprising analogies between the cases of electrical and thermal charging cycles were found through the development of an equivalent electrical circuit, that can effectively describe thermo-charged systems. With these results, some experimental observations were interpreted and the device was optimized to maximize its energy efficiency.

Sommario

Obbiettivo di questo lavoro di Tesi è capire il comportamento di un supercapacitore sottoposto a un gradiente di temperatura e il modo nel quale questo gradiente può essere usto per caricare un supercapacitore. L'applicazione di un gradiente di temperatura a un elettrolita genera un moto di deriva degli ioni, avendo cationi e anioni riposte differenti ad effetti termici, si genera così uno sbilanciamento di carica e di conseguenza si può misurare una differenza di potenziale. Questo effetto può quindi essere usato per sfruttare una differenza di temperatura per caricare una sistema elettrodo-elettrolita, come una batteria o un supercapacitore. Le origini della deriva termica degli ioni non sono completamente chiare, così come non lo sono i meccanismi interni che accadono durante un ricarica termica di un supercapacitore.
Diversi approcci teorici possono essere applicati allo studio di questo fenomeno, ma la scarsa letteratura in merito obbliga ad usare metodi semplici, per comparare i risultati con l'intuizione fisica. Una conoscenza più profonda di questi sistemi può aiutare nello sviluppo di migliori dispositivi per la conversione dell'energia termica, che sfruttino il calore di scarto a bassa temperatura per produrre energia elettrica carbon-free.
In questo lavoro di Tesi, ho analizzato il caricamento termico di un supercapacitore con calcoli analitici, simulazioni numeriche e circuiti equivalenti. Sono state fatte diverse approssimazioni per descrivere un sistema tridimensionale complesso, tal'è un supercapacitore, con un modello monodimensionale veloce dal punto di vista computazionale e efficace da quello concettuale.
Sono state spiegate la capacità e la dinamica di ricarica di un supercapacitore ricaricabile termicamente. In particolare, attraverso lo sviluppo di un circuito elettrico equivalente che possa descrivere sistemi termo-caricati, sono state trovate sorprendenti analogie tra il caso di ricarica elettrica e quello di ricarica termica. Con questi risultati alcune osservazioni sperimentali sono state interpretate e il dispositivo è stato ottimizzato per massimizzare la sua efficienza energetica.

Estratto

Questo lavoro di Tesi è stato svolto in collaborazione con l'istituto di fisica teorica di Utrecht, in particolare con il gruppo di ricerca del Prof. René van Roij, che si occupa da diversi anni di indagini teorico-simulative nel campo degli elettroliti. Il lavoro verte sull'analisi teorica dei fenomeni che accadono quando un supercapacitore, cioè una capacitare elettrochimico con elettrodi nanotrutturati, è posto in un gradiente termico. In quanto segue, introdurrò dapprima i concetti teorici atti a comprendere i fenomeni fisici in gioco, per poi mostrare come questi siano stati analizzati e modellizzati per ottenere una spiegazione efficace del comportamento di un supercapacitore, nel momento in cui questo viene utilizzato come dispositivo atto a convertire energia termica a bassa temperature in energia elettrica.

É noto come certe sostanze, ad esempio i sali, tendono a dissociare spontaneamente in contatto con un eccesso di solvente, creando cationi positivi e anioni negativi liberi di muoversi all'interno del fluido. Questo fenomeno è dato dal bilanciamento fra la componente entropica dell'energia libera dovuta alla maggiore libertà di movimento degli ioni, e la componente Coulombiana che tende a far si che ioni di carica opposta si attraggano.

Gli ioni in un elettrolita interagiscono quindi principalmente attraverso forze di natura elettrostatica, essendo però influenzati anche da fenomeni di origine statistica, quindi diffusivi, e fenomeni fluidodinamici, in quanto il moto del solvente modifica ed è modificato da quello degli ioni. Tra questi effetti da qualche anno hanno suscitato interesse gli effetti di natura termoforetica. É infatti noto da quasi cento anni che una particella di soluto posta in un solvente non isotermo, ma nel quale è presente un gradiente di temperatura, avrà un moto di deriva lungo la direzione del gradiente. Questo è chiamato effetto Soret. I meccanismi alla base di questo fenomeno non sono completamente chiari, difatti la maggior parte delle sostanze ha un comportamento termofobico, muovendosi quindi verso la zona a temperatura minore; altre hanno invece un comportamento termofilico. Qualche analisi teorica è stata fatta nel caso di ioni in soluzioni acquose, Agar ha difatti usato il modello di Born per l'interazione ione-solvente per calcolare il valore di questo coefficiente Soret. Da questa, seppur basilare, teoria è possibile individuare nel fatto che costante dielettrica del solvente sia dipendente dalla temperatura una delle cuase principali del moto degli ioni sotto gradiente termico.

Nel contesto della transizione energetica verso una produzione più efficiente e meno inquinantne, è importate sfruttare il calore di scarto a bassa temperatura per produrre ulteriore energia elettrica. Nello stesso modo in cui la ricerca ha sviluppato materiali e dispositivi in grado di utilizzare l'effetto Seebeck nei solidi per questo scopo, così negli

ultimi anni è cresciuto l'interesse nello sfruttamento di questo effetto equivalente nei liquidi. Sfruttando le evidenze sperimentali, che mostrano un coefficiente equivalente di Seebeck in alcuni elettroliti di ordini di grandezza superiore a quello dei solidi, sono state progettate e sperimentate numerose tipologie di dispositivi, con lo scopo di raggiungere efficienze di conversione pari o superiori a quelle dei semiconduttori. Oltre all'utilizzo di celle elettrochimiche, le cui specie reagiscono con gli elettrodi per creare una corrente elettrica continua, sono stati studiati anche dispositivi basati su cicli termodinamici. In particolare, interessanti risultati sperimentali sono stati osservati nell'uso di supercapacitori ricaricati tramite una differenza di temperatura fra gli elettrodi. La presenza di elettrodi nanostrutturati, che possono quindi ospitare una rilevante quantità di carica, e l'assenza di reazioni chimiche, rendono i supercapacitori in grado di generare potenze elettriche sufficienti all'uso industriale per quasi infiniti cicli di carica e scarica. Queste loro proprietà, e l'economicità dei loro materiali, li rendono ideali per la conversione energetica sopra citata.

Seppur sono presenti studi sperimentali su questi cicli termodinamici, nessun modello è stato proposto per valutare a priori il comportamento degli stessi in base alla scelta dei materiali e alla configurazione del dispositivo. A tal fine ho cercato di modellizzare un supercapacitore ricaricabile termicamente, con l'utlizzo di calcoli analitici, simulazioni numeriche e circuiti equivalenti. Prima di esporre il lavoro è necessario ricordare che un capacitore elettrochimico conserva la carica in un doppio strato elettronico formato da ioni a contatto con l'elettrodo la cui carica è specchiata nella carica superficiale dello stesso. Va poi presentato il ciclo di ricarica termica di un supercapacitore, che consta di quattro fasi distinte: la fase i in cui si impone la differenza di temperatura ai capi a circuito aperto, in cui quindi si osserva una differenza di potenziale fra gli elettrodi; la fase ii in cui si chiude il circuito lasciando il gradiente termico, caricando così il dispositivo; la fase iii in cui si apre il circuito e si riporta il sistema in condizione isoterma, ottenendo quindi un normale supercapacitore carico; infine l'energia elettrica accumulata viene utilizzata su un carico elettrico durante la fase iv. Per analizzare questo sistema, ho dapprima utilizzato le soluzioni analitiche delle equazioni che governano la fisica dei liquidi carichi (equazioni di Poisson-Nernst-Plank), risolte nel caso di un capacitare elettrochimico ad elettrodi piani e paralleli. Con quei risultati, e le simulazioni numeriche che li confermano, è stato sviluppato un circuito elettrico equivalente che permette di risolvere il sistema dinamico in modo veloce ed efficace. Il circuito equivalente da me ottenuto è quindi composto da due capacitori che rappresentano il doppio strato elettronico, una resistenza per considerare la conducibilità elettrica dell'elettrolita e da un generatore di potenziale che tiene conto dell'effetto Seebeck che si origina quando il gradiente termico è applicato. Osservando successivamente il comportamento di un *super*capacitore è evidente come sia complesso e numericamente oneroso, volendolo simulare nella sua interezza sarebbe richiesta un'analisi tridimensionale che prenda in considerazione la nanostruttura degli elettrodi. Lo "Stack Electrodes Model", usato in questa tesi, considera invece un solo macroporo che idealmente collega la zona centrale del supercapacitore con l'estremo ultimo dell'elettrodo, a cui sono perpendicolarmente collegati n micro o nano pori. La dimensione dei micropori è quindi rappresentata nella distanza fra elettrodi permeabili messi in fila. Questo modello è già stato utilizzato in letteratura per comprendere la dinamica dei supercapacitori caricati da una sorgente elettrica esterna.

Con questo lavoro è stato invece dimostrato come lo Stack Electrodes Model permetta

un'analisi dinamica anche nel caso di ricarica termica. In particolare, si deve considerare che per simulare un supercapacitore intero sarebbe necessario risolvere le equzioni di stato del sistema per un numero n di elettrodi dell'ordine di grandezza dei milioni. Risulterebbe quindi computazionalmente molto oneroso, se non impossibilie. Similmente a quanto fatto nel caso del capacitore piano, si è sfruttato il circuito elettrico equivalente che lo Stack Electrodes Model genera. Il sistema lineare da esso creato è quindi stato risolto, ottenendo relazioni algebriche valide per ogni numero n di elettrodi.

Sono quindi stati ottenuti sia risultati soprendenti e inaspettati che spiegazioni a fenomeni osservati sperimentalmente.

Dapprima si è osservato che durante la prima fase a circuito aperto è presente una particolare distribuzione della densità di carica: all'interno dello stesso elettrodo nanostrutturato sono presenti zone a carica positiva e zone a carica negativa. Questo fenomeno è dovuto al bilanciamento fra la necessità elettrostatica di mantenere la neutralità elettrica nell'elettrodo a circuito aperto e il potenziale generato dall'effetto Seebeck nello stesso. Inoltre le curve che descrivono il potenziale fra gli elettrodi sono ben diverse da quelle che si ottengono solitamente negli studi isotermici, il motivo è stato individuato e dimostrato nella sovrapposizione degli effetti: sommando la funzione del potenziale o della densità di carica della fase i, in cui principalmente dominano gli effetti termici, con quella della fase iii, in cui il sistema è carico ed isotermo, si ottengono le soluzioni per la fase ii che consta sia di effetti termi che di quelli elettrici.

Oltre a queste particolarità fisiche, il circuito sviluppato è stato fondamentale nel calcolo della dinamica delle varie fasi, dimostrando in particolare come i tempi caratteristici della fase ii di carica coincidono con quelli della ricarica "classica" attraverso una batteria esterna. Oltre alla dinamica sono state anche evidenziate le particolarità riguardo la capacità di un sistema caricato con gradiente termico, dato che la presenza del gradiente attraverso gli elettrodi stessi rende la carica superficiale non omogenea. Questo effetto obbliga a riconsiderare la quantità di carica totale accumulabile dal capactiore e rende la stessa dipendente dai parametri strutturali. In particolare si può dimostrare come un supercapacitore con un elettrodo spesso rispetto alla lunghezza totale del sistema perda la metà della capacità originale.

Con queste informazioni è stato infine possibile calcolare l'efficienza del ciclo termodinamico. Dato il ciclo descritto precedentemente composto da quattro fasi, le prime due consumeranno energia termica dovendo mantenere una differenza di temperatura. La dinamica di queste fasi è quindi fondamentale per calcolare l'efficienza, dato che la maggior parte del calore è utilizzato nel come flusso termico la cui energia termica totale sarà quindi direttamente proporzionale al tempo di ricarica. Solo una parte trascurabile di calore è invece assorbita dall'elettrolita, la quale può essere comunque recuperata attraverso cicli rigenerativi. La carica totale accumulata è invece proporzionale alla superficie totale degli elettrodi. Si è quindi potuta ottimizzare la geometria del dispositivo, in base al numero di pori e alle dimensioni degli elettrodi rispetto alla lunghezza totale. Si osserva come l'efficienza non aumenti aumentando il numero di pori dell'elettrodo, in quanto l'energia elettrica accumulata cresce insieme ai tempi di ricarica, ottenendo, imprevedibilmente, che un capacitare ad elettrodi piani ha la stessa efficienza totale di un supercapacitore ad elettrodi nanostrutturati sottili. É invece evidente come l'uso di elettrodi spessi sia svantaggioso in quanto i tempi di ricarica non sono più compensati da un aumento di

capacità dovuto alle considerazioni precedentemente esposte. Da questa ottimizzazione si ricava una semplice relazione che lega l'efficienza assoluta totale al parametro di merito adimensionale ZT^*.

ZT^* è una valore, solitamente utilizzato nell'ambito dei semiconduttori, che mostra quanto quel materiale sia adatto a scopi termoelettrici, è direttamente proporzionale al quadrato del coefficiente di Seebeck, alla conducibilità termica e alla temperatura massima raggiunta dal ciclo termodinamico, è invece inversamente proporzionale alla conducibilità termica. Nonostante gli ottimi valori sperimentali dei coefficienti di Seebeck e la bassa conducibilità termica dei liquidi, la conducibilità elettrica è il fattore limitante che rende l'efficienza totale non ancora in linea con altre tecnologie termoelettriche. In particolare si mostra come attualmente i migliori liquidi termoelettrici abbiano valori di ZT^* di 0.01 quando invece, dall'analisi compiuta, sarebbe necessario raggiungere valori vicini all'unità per ottenere il 20% dell'efficienza di Carnot equivalente e addirittura avvicinarsi a 5 per ottenerne il 100%, il tutto considerando un supercapacitore ideale, privo di reazioni parassite irreversibili.

Va infine considerato che il lavoro svolto è stato ideato e calcolato pensando ad elettroliti diluiti, nei quali è possibile risolvere le direttamente o numericamente le equazioni di Poisson-Nernst-Plank. I migliori risultati sperimentali in termini di efficienza sono invece stati ottenuti con elettroliti più complessi da modellizzare, come polielettroliti semi-solidi o liquidi ionici. Questi ultimi presentano effetti Soret non ancora spiegati a livello teorico e quindi difficili da applicare a un sistema complesso. Sarà quindi compito di futuri studi, una volta poste basi teoriche più solide, adattare il modello qui sviluppato, in modo da ottimizzare ulteriormente il dispositivo e stabilire se questo filone di ricerca potrà produrre un nuovo sistema di conversione di energia da calore di scarto a bassa temperatura.

Contents

List of Figures

Introduction

One of the main challenges of this century is to reach carbon neutrality for the year 2050. This challenge can be addressed in numerous ways, which is the right route to follow is an object of debate all around the world. However, the one thing on which everyone agrees is that it is necessary to use every possible drop of clean energy that is produced. Knowing that, due to the usual thermodynamic cycles applied, almost two-third of the thermal energy produced is lost, a question arises: how can we exploit that energy?

In the last years, countless technologies were proposed to face this challenge, among which thermoelectric materials seem to be the most promising. They use the property of some materials, usually semiconductors, to generate a current or a potential difference when a temperature gradient is applied: this is called *Seebeck effect*. In the context of thermoelectricity, the good experimental results for the Seebeck effect in some electrolytes opened the doors to the use of liquid thermoelectric technologies. A complete theoretical description of the Seebeck effect in electrolytes is still missing, however its origins can be classified as chemical or physical. In the case of a redox reaction, the temperature dependence of the reactions are responsible for the voltage difference between the cold and the hot side. In a non-Faradaic system the Seebeck effect originates only from the *thermophoresis* of the ions. The thermophoresis, also called *Soret effect*, is a particle motion induced by a thermal gradient, the *Soret coefficient* permits to calculate the drift ion velocity knowing the thermal gradient. The mechanisms of thermophoresis are not completely clear, it is only known that the particle-solvent interaction is the main driver of the thermophoresis and that te temperature dependence of the dielectric constant is a key factor in the case of ions in polar solvents. However, the values of the Soret coefficients can be experimentally measured, so that they can be used to calculate the behaviour of an electrolyte posed in a temperature gradient. Nevertheless, the subject remains challenging, almost all the parameters that describe a liquid system, depend on temperature: varying the temperature means changing the dielectric constant, the diffusivity, the density, the thermal conductivity, and the Soret coefficient itself.

For these reasons, namely for possibility to analyse only the physical behaviour and to be able to solve analytically the equations, the study of a *thermally rechargeable supercapacitor* was chosen. A thermally rechargeable supercapacitor is an electrochemical capacitor, with nanoporous electrodes, that is charged with an imposed temperature gradient. From a conceptual point of view, the Soret effect mentioned above, acting with different intensity on anions and cations, permits to charge the supercapacitor. It was

decided to model and simulate a thermodynamic cycle capable of charge the supercapacitor with the least amount of thermal energy, in order to understand the internal behaviour and the impact of the nanoporous electrodes on the system. The analysis of the interactions between a system subjected to thermophoretic forces and a nanostructure is, as far as we know, still missing in literature. To do so, it will be first necessary to solve and model the entire cycle for a planar electrochemical capacitor, and then to expand the model for accommodating the particularities of a nanoporous electrodes device. Analytical solutions, numerical simulation and equivalent circuits analysis will be exposed and the results will be used to optimize the efficiency of the thermodynamic cycle. It is, therefore, worth outlining the structure of this Thesis:

- In the second chapter will be exposed the broad range of solid-based and liquid-based technologies that aim to convert efficiently low-temperature heat waste into electrical energy. The advantages and disadvantages of these methods will be exposed, showing the importance of further study in the liquid-based field. Moreover, specific attention will be placed on the capacitive systems, batteries and especially supercapacitor, to have a clearer picture of the device considered and the models that describe it. Finally, a reference experiment will be exposed.

- The third chapter will be composed of the theoretical framework needed to understand the system quantitatively. The physics of the electrostatic interactions that govern electrolytes will therefore be explained. Moreover, some hints on irreversible thermodynamics will be exposed to describe the cross effects responsible for the Soret effect, and consequently for the Seebeck effect. Various methods to model a charged system will be explained, as well as the original Agar's theory for the Soret effect in electrolytes.

- The actual Thesis Work will start in the fourth chapter, in which it will be presented the study of an electrochemical capacitor, with planar electrodes, subjected to a temperature gradient. Analytical solutions, confirmed by numerical simulations, will placed the basis from which an equivalent electrical circuit will be developed to describe the system.

- The model of the fourth chapter will be expanded in the fifth one. From a simple planar electrode, the complexity will be increased with a stack electrode model that can simulate a nanoporous electrodes system. First, a two-electrodes solution will be done to pose again the basis of this new configuration, then a n-electrodes solution will be achieved using the electrical circuit developed before.

- In the sixth chapter, the linear, low temperature, system of the previous chapters will be taken to extreme conditions, in order to address the validity of the model. Some consideration will then be drawn on the limits of the model.

- The considerations and the relations found above will then be used in the seventh chapter to calculate and optimize the energy conversion efficiency of the thermally rechargeable supercapacitor.

Phenomenology and Applications

Nowadays, the ever-increasing energy demand needs to be shifted towards carbon-free and sustainable production. Due to the economic growth the energy to be produced increases and the majority of that, today, comes from fossil fuels. The fossil fuels emissions are responsible for the global warming due to the high quantity of CO_2 that these technologies produce, and they are also responsible for millions of deaths every year due to the damages the other chemical compounds emitted create.

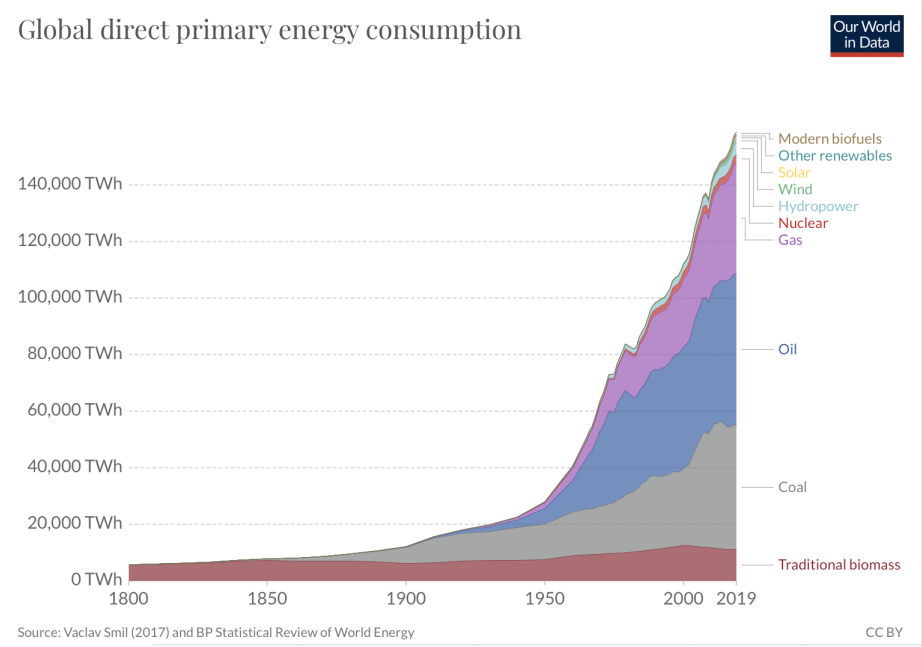

Figure 2.1: Global energy consumption from 1800 to 2019 [1].

As it is possible to see in figure 2.1 the energy sources that emit carbon dioxide are still the vast majority and this needs to be changed in order to prevent the climate crisis. To achieve this goal, we need to change the energy sources (nuclear, wind and solar must be improved), reduce energy consumption, and improve the efficiency of production. Almost two-third of the energy produced is indeed lost due to the low average efficiency of the technologies adopted nowadays, the majority of which is converted into low-temperature heat waste [7].

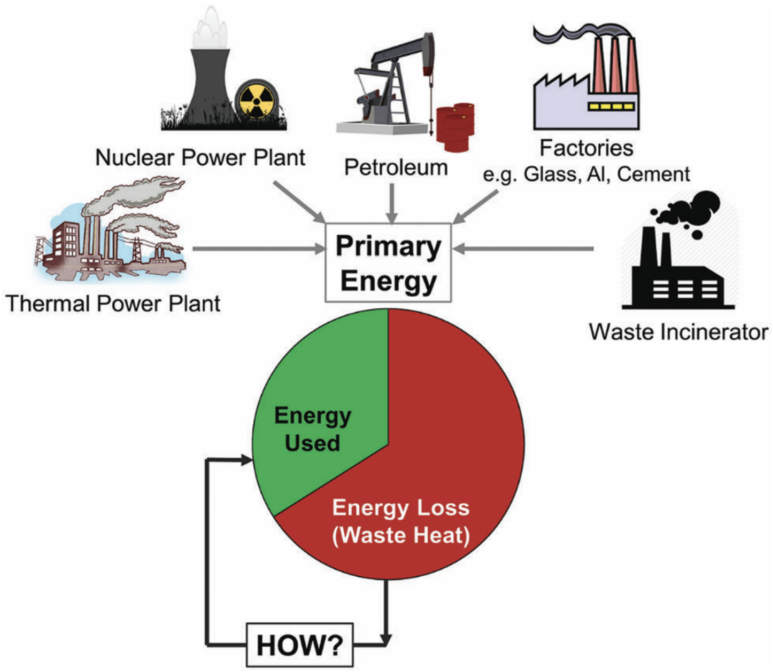

Figure 2.2: Sketch of the main production sources of waste heat.

Some examples could be low-concentration solar heat collectors, household co-generation, low temperature geothermal heat, car engines, industrial and thermal power plants waste heat. These kinds of sources provide fluids with temperatures below 100 °C that are not useful in the usual thermodynamic cycles. Some estimates calculated that only the potential of industrial heat waste in Europe is around 23 TWh/year [7].

Various physical phenomena are studied to develop a device that could convert this heat into electricity, with a good efficiency: thermoelectric materials, heat engines based on Stirling cycle or organic Rankine cycle, thermo-magnetic motors, and thermoelectrochemical processes.

The thermoelectric materials can convert heat directly into electricity; the organic heat engines try to use thermodynamic cycles similar to the water-based ones but with low boiling temperature organic mixtures; the thermo-magnetic motors use the paramagnetic-ferromagnetic transitions at the right temperature to create mechanical torque [8]; the thermoelectrochemical processes combine thermal mechanism and electrochemical ones to convert heat into electricity [9].

The goal of the research is to create small, durable, scalable and cheap devices that produce energy with low maintenance and simple installation.

This work is part of this research. In particular, the solid-state thermoelectric materials have reached a high level of technological advancement and an optimal level of physical comprehension of their mechanisms. By contrast, the thermoelectric technologies based on electrochemical processes are still not optimized and understood. The promising experimental results on this topic create the need for further theoretical comprehension of it. This work will try to understand if a thermoelectrochemical technology is a useful tool for exploiting the low-temperature heat waste, simulating and calculating the behaviour of a thermally rechargeable supercapacitor.

2.1 Solid-State Thermoelectric Technologies

Certainly, the thermoelectric technologies are the most researched technologies that have the scope of exploit the low-temperature heat source. In particular, the historically most studied ones are the thermoelectric solid-state materials.

Phenomenology

The solid-state thermoelectric materials utilize the Seebeck effect to generate a potential difference between the sides of a material when a temperature difference is applied.

The Seebeck effect was discovered by Thomas Johann Seebeck in 1821 who found out that a circuit made from two different metals, with junctions at different temperatures would deflect a compass magnet [10], and then discovered that a temperature difference in the metal could drive an electric current. The Seebeck effect is part of a group of thermoelectric (and magnetic) phenomena that are originated when fluxes of heat or particles are present in a material.

- When we keep the two ends of a conductor at different temperatures, a voltage difference is established, this is called *Seebeck effect*.

- When a current is imposed in a conductor a difference in temperature between the two ends can be measured, this is the *Peltier effect*.

- When a difference in temperature and a current are imposed the material will absorb or release heat, this is the *Thomson effect*.

To explain the phenomena it is possible to imagine the charge carriers inside the material (electrons or holes) as ideal gas particles. When a current is imposed the particles (so the charges) will carry some energy from one side to the other generating a temperature difference, this explains the Peltier effect. Inversely, when a temperature difference ΔT is imposed, the particles will gain kinetic energy in the hot end, so they will accumulate in the cold end, producing a repulsive interaction force. These two forces, balancing each other, are in steady-state when a voltage difference ΔV is generated.

The relation is simple:

$$\Delta V = S_e \Delta T \,, \tag{2.1.1}$$

where S_e is the Seebeck coefficient.

From solid-state physics it is possible to demonstrate that metals are very poor thermoelectric materials, with usually low Seebeck coefficient and high thermal conductivity. The metals are therefore only useful for thermocouples or other instrumentation.

The best choice for energy generations are instead the semiconductors. These materials can be engineered in order to achieve low thermal conductivity, high Seebeck coefficient and high electrical conductivity. Moreover, the possibility exists to chose the signs of S_e: the n-type semiconductors (that uses electrons as charge carriers) have negative S_e, the p-type semiconductor (that uses holes as charge carriers) have positive S_e.

These features allow us to create a thermoelectric generator device (TEG): the thermoelectric elements are connected thermally in parallel and electrically in series (figure 2.3). This setup creates the conditions to either use a heat flux to generate electric power or to use an electric current to cool a device.

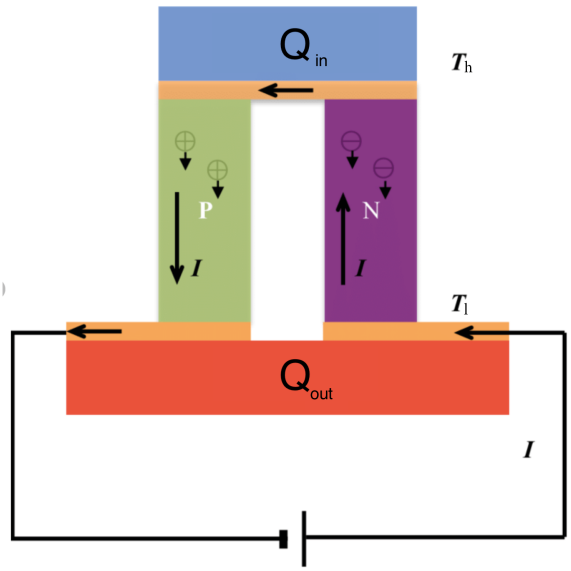

Figure 2.3: Sketch of a thermoelectric current generator device composed by a p semiconductor (green), a n semiconductor (purple) electrically connected and thermally in parallel, in which the heat is absorbed in the blue zone and realised in the orange zone.

Efficiency

Like all heat engines, the TEGs obey the laws of thermodynamics: to calculate the efficiency it is necessary to calculate the ratio between the thermal energy used and the electrical energy produced.

$$\eta_{abs} = \frac{P_{el}}{Q_{in}}\,, \tag{2.1.2}$$

where η_{abs} is the absolute efficiency, P_{el} is the electric power produced per unit area and Q_{in} is the heat flux that goes through the device. The power produced is of course the current times the voltage; the heat flux is composed of the heat conducted by the materials, the joule heat developed by the current and the Peltier heat exchanged.

Selecting an optimal load and optimal dimensions for the modules the overall efficiency can be calculated as:

$$\eta_{max} = \frac{T_h[\sqrt{1+ZT} - \frac{T_h}{T_l}]}{(T_h - T_l)[\sqrt{1+ZT}+1]} \tag{2.1.3}$$

where ZT is called *dimensionless figure of merit*, T_h and T_l are the higher and the lower temperature respectively [11]. The value of ZT can be calculated from the material properties:

$$ZT = \frac{S_e^2 \sigma_{el} T}{k} \,, \tag{2.1.4}$$

where S_e is the Seebeck coefficient, σ_{el} the electrical conductivity, k the thermal conductivity and T the absolute temperature.

To have an idea of the average efficiency of a thermoelectric material, it is necessary consider the usual values that the parameters cited above have: $S_e = 10^2 \mu V K^{-1}$, $\sigma_{el} = 10^5 S/m$ and $k = 1 W m^{-1} K^{-1}$. This leads to an average ZT of 1 for the common materials.

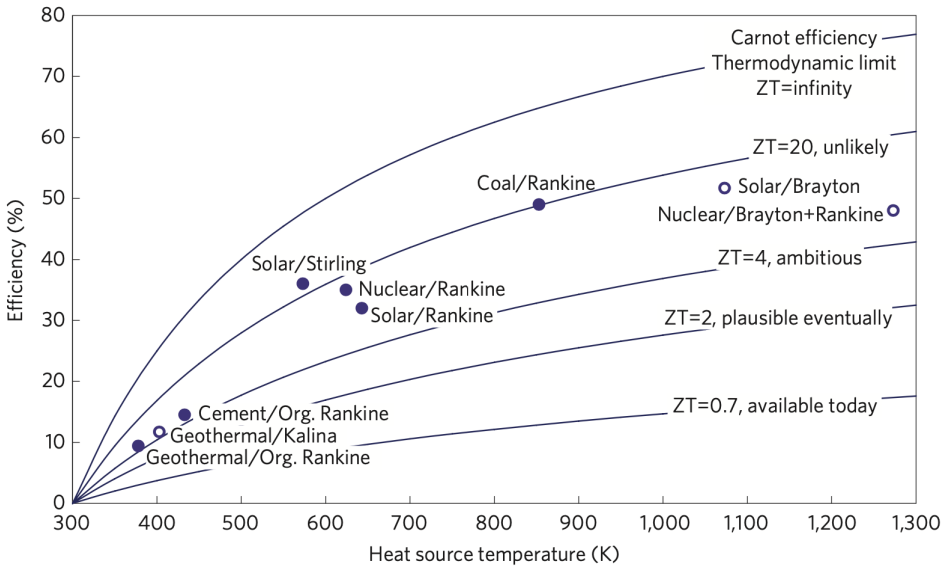

Figure 2.4: Efficiency vs Temperature of the heat source at various theoretical dimensionless figure of merit of thermoelectric materials, compared with the efficiencies of classic thermodynamic cycles [2].

Figure 2.4 shows then the efficiencies that can be reached by the various energy production methods, compared with the equivalent efficiency that a material with a specific ZT can achieve. If the average ZT of 1 is considered, the obtainable efficiency is particularly low, especially if the heat source is in the order of 400 K. In particular the efficiency of a thermoelectric device with $ZT = 1$ working between 300 K and 400 K is $\eta_{max} = 13\%$, which is the 52% of the Carnot efficiency. The Carnot efficiency is the maximum efficiency which can be reached when an ideal thermodynamic cycle is run between two temperature and it is calculated as

$$\eta_{Carnot} = 1 - \frac{T_l}{T_h} \,. \tag{2.1.5}$$

It is clear that, to have competitive energy production from thermoelectric technologies, the figure of merit needs to be improved, at least up to 2 or 3.

Advance Technologies

The research in the field of new and efficient thermoelectric materials is focused on the development of materials with a high Seebeck coefficient, high electrical conductivity, but low thermal conductivity. Stating that the thermal conductivity is related to the mobility of the carries, the goal is ambitious. Two main routes are now researched with the aim to develop a phonon-glass electron-crystal materials (so a material that is disordered for phonon but ordered for electrons).

The first is the use of particular structured materials with cages or substructures that interfere with the motion of phonons, but which leave the electrons travel through the crystalline structure. The second are nanostructured materials which either have grain dimensions between the phonon and electron scattering lengths or utilize band confinement to create superlattices with the use of ordered nanoparticles. These last advancements achieved a ZT of 3.5 at 575 K [2], but the creation of the material is very difficult and expensive in a laboratory and practically impossible at an industrial scale.

A good industrial process can produce a thermoelectric material today that has only a ZT of 1.5, for example a micro-structured bismuth-telluride.

For these reasons the semiconductor thermoelectric materials are now used only in some particular applications such as space or electronics, but not in the exploitation of the large amount of low-temperature heat waste. Given the many years of research and advancements on the solid-state thermoelectric technologies, that have reached incredible, but always expensive, results, one is tempted to believe that the improvements in this field are destined to be limited and an industrial-scale device cannot be achieved.

2.2 Liquid-Based Thermoelectric Technologies

During the last ten years, some experiments opened the doors for new devices [12], based on liquid-based electrochemical cells instead of solid semiconductors.

The thermoelectrochemical technologies developed are various and use a wide range of physical phenomena to convert heat into electricity, going from direct thermoelectric systems to osmotic gradient exploitation. They can be divided into two major groups: direct and indirect utilization of low temperature heat waste. Thermoelectrochemical cells (TECs) [9] , thermo-osmotic conversion devices (TOEC) [13], and thermally regenerative electrochemical cycles (TRECs)[14] use low-grade heat generating directly electrical power. The indirect utilization exploits instead low grade-heat to produce solutions at different concentrations which are used in salinity gradient energy systems (SGE) [15] or thermally regenerative batteries (TRBs) [16]. A summary, taken from the work of Rahimi and Co [4], of the existing methods is presented below, in order to give a wide prospective on the routes the research is following now.

Salinity Gradient Energy Systems

Several technologies have been developed to extract energy from two solutions of different concentrations [17]. These technologies could be used both to extract energy from natural (e.g., seawater – river water) or industrial salinity gradients and to exploit heat waste. The low-grade heat is used in the distillation process to obtain streams with different salinities.

These streams can be used to produce energy with pressure retarded osmosis (PRO) [18], reverse electrodialysis (RED) [19] or capacitive mixing (CapMix) [20]. The modern cheap and effective membranes opened the doors for the first two methods, the renewed nanostructured electrodes allowed CapMix to be a possible way to generate electricity from concentration differences. The overall efficiency of these devices is estimated to be around 5-10% of the Carnot efficiency [4]. Improvements in the salinity gradient technology are so strictly related to improvements in low-grade heat exploitation. In particular, it is interesting to track the development of the supercapacitors because, as this work explains, they can be used both as direct and indirect low-temperature energy conversion devices.

Thermally regenerative batteries

The thermally regenerative batteries (TRB) are based on oxidation and reduction of metal electrodes. The device is composed of two chambers separated of an anion exchange membrane, in one a ligand (e.g., ammonia) is present hat becomes the anode. The cell after the discharging cycle, it is heated to distil the ligand, which is then added to the electrolyte in the other side of the cell, making the other side now the anode.

The TRBs can perform at high temperatures and are relatively cheap. The efficiency nowadays goes from 6.2% to 12% of the Carnot efficiency, but the research on this topic is in its early days (the first proposal was made in 2015). The main challenge is the long term stability of the electrodes that are rapidly damaged by the cycles.

Thermo-osmotic energy conversion

The thermo-osmotic direct energy conversion (TOEC) is based on the use of waste heat to create a temperature difference between two reservoirs divided by a membrane. As the thermo-osmotic liquid of the hot reservoir flows across the membrane the cold reservoir becomes pressurized, the pressurized liquid then flows through a turbine that generates electricity. The membrane transforms thermal energy in hydraulic energy.

Some models have been used to calculate the theoretical efficiency: the maximum one should be 4.1%. The system is not well optimized, other membranes and liquids should be tested. The aim is to achieve a pressure of 50 bar obtaining an efficiency of 6,8% [21].

Thermoelectrochemical Cells

The thermogalvanic effect is very similar to the thermoelectric effect of a semiconductor: a redox electrolyte is positioned in an electrochemical cell and a temperature difference between the electrodes is applied, generating a voltage difference or a current. The current is originated from the temperature dependence of the redox reaction: the redox couple will be oxidized at the hot anode and reduced at the cold cathode. The reduced species are then transported by convection, diffusion, and thermophoresis to the anode creating a continuous current (see figure 2.5).

The magnitude of the voltage difference arising is proportional to the entropy difference of the reactions

$$S_e^* = \frac{dV}{dT} = \frac{(S_B + S_B') - (S_A + S_A') - nS_{el}}{nF}\,, \tag{2.2.1}$$

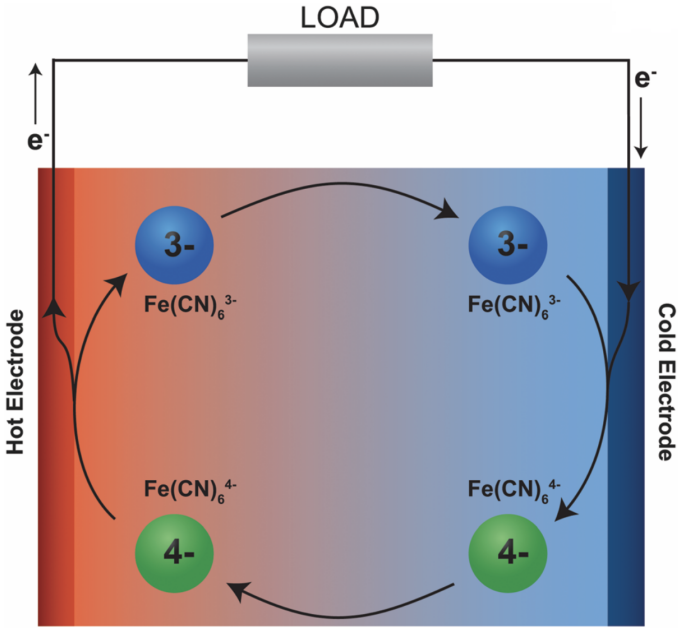

Figure 2.5: Sketch of the mechanism inside of a thermogalvanic cell.

where V is the electrode potential, n is the number of electron involved in the reaction, F is the Faraday's constant, S_A and S_B are the partial molar entropies of species A and B, S'_A and S'_B are the Eastman [1] entropies and S_{el} is the entropy transported by the electrons in the external circuit. Usually S'_A, S'_B and S_{el} are negligible so the Seebeck-like coefficient is approximable as

$$S_e^* = -\frac{\Delta S_{A,B}}{nF} \tag{2.2.2}$$

The main difference between this cell and a solid-state material is that, in this case, the reaction and the material transport are involved. This consideration is important in order to analyse the problems of this technology: the reactions can damage the electrodes in the long run and the limiting factors to optimal efficiency are multiple. The most important ones are the ohmic, charge transfer, and mass transport overpotentials [2], the temperature effects on the solvent and the side reactions. All these aspects are linked together and are non-linearly dependent on the temperature.

To evaluate the performance of a thermogalvanic cell it is possible to adapt the dimensionless figure of merit, considering that the overall conductivity will be proportional to the most limiting factor from the cited above and the concentration of the redox couple. The figure of merit proposed by Abraham et al. [22] is

$$ZT^* = \left(\frac{z^2F^2}{R}\right)\frac{S_e^2 D_{lim} c}{k} \tag{2.2.3}$$

[1] The Eastman entropy is the entropy transported due to the Dufour's heat, this topic will be discussed in details in the next chapter.

[2] The overpotential is the potential difference between the thermodynamic determined potential at which the reaction should take place and the measured potential difference at which it is observed, this effect is due to irresponsibilities of the process taken into account.

where R is the gas constant, D_{lim} is the limiting diffusion coefficient and c is the redox couple concentration. From this figure of merit it is trivial to see that the main problems are the ones related to the overpotentials inside the cell, they could be overcome modifying the electrolyte or the electrodes.

The final setup of the thermogalvanic cells is very similar to the one of the solid-state systems in which we use a sort of p-type and n-type cell, selecting the reactions, to create an electrically in series – thermally in parallel system, which can provide a good amount of voltage and current.

The Seebeck-like coefficient of these kinds of cells are very high with respect to the semiconductor materials, in the order of some mVK^{-1}, but the overall figure of merit is usually limited by the low electric conductivity, so the average efficiency in the research are in the order of 1% with some reported ones near 4% [9].

The thermogalvanic cells can be classified by the redox couple, the solvent, or by the electrodes used.

- The choice of the redox couple can change significantly the magnitude and even the sing of the Seebeck coefficient: these values are determined by the interaction between the species and the salvation shell. One of the most promising and studied redox couple is the ferricyanide/ferrocyanide couple that has a Seebeck coefficient of $-1.4mVK^{-1}$ [23]. The cells obtained with this couples have good electrode resistance and high current densities. Another important redox couple is the I^-/I_3^- couple, it was studied in aqueous and non-aqueous solvent, with stainless steel electrode or with platinum electrodes [23]. Other couples are cobalt-based [24] or mixes of different inorganic redox couples. Some organics redox couples are studied too.

- A wide spectrum of aqueous and non-aqueous solvents are used [25] [24]. The aqueous electrolytes have high power output but the low boiling point of water can limit the use to only certain ranges of temperature. Ionic liquids (ILs) have instead high boiling points, high ionic conductivity and can produce high Seebeck coefficients (up to $2.9mVK^{-1}$), achieving similar ZT to the semiconductor thermoelectric materials, despite the low viscosity. Some additives are tried to overcome this issue. Moreover, organic molecular solvent, gels and quasi-solid-state polyelectrolytes are experimented as promising for application with particular geometry (for example body heat exploitation) having a high viscosity and good Seebeck coefficient of the order of $1mVK^{-1}$.

- The most studied electrode materials are platinum and carbon, but a lot of different materials are now considered [26]. The platinum ones have high catalytic activity but the cost is a limit for industrial application. The most promising ones are the carbon nanostructured that posses a large surface area, increasing the number of reaction sites, this provides higher specific power and an efficiency of 3.95% was achieved [27]. The carbon nanostructures can be doped or coated to improve the catalytic characteristic or the conductivity. The orientation and the thickness of the cell can be varied depending on the balance between the thermal and electrical conductivity improvements due to the convection effect. Similar considerations can

be applied to the use of selective membranes that can block the heat flux of the solvent but can also reduce ion mobility.

The list of new technologies is far larger than the one cited above, for example, interesting studies are trying to combine membranes or colloidal effects with the right redox couples. The aim of this section is therefore only to give some hints on the vast research present in the field of thermoelectrochemical cells.

Thermally Regenerative Electrochemical Cycles

The final direct method to convert heat into electricity is based on a more conventional strategy, but applied to electrochemical cells: thermodynamic cycles.

It is called thermally regenerative electrochemical cycle (TREC). The core of the process is to create a Stirling-like thermodynamic cycle using a capacitor or a battery. In particular, the usual cycle uses the difference in charging energy obtainable when the device is charged at high temperature and discharged at low temperature [28]. The cycle is so composed of cooling-discharging-heating-charging. This mechanism produces electrical power because the charging voltage is lower than the discharging one. The cycle is called regenerative because is possible to regenerate part of the heat absorbed inn order to heat the upcoming cold fluid, improving the efficiency.

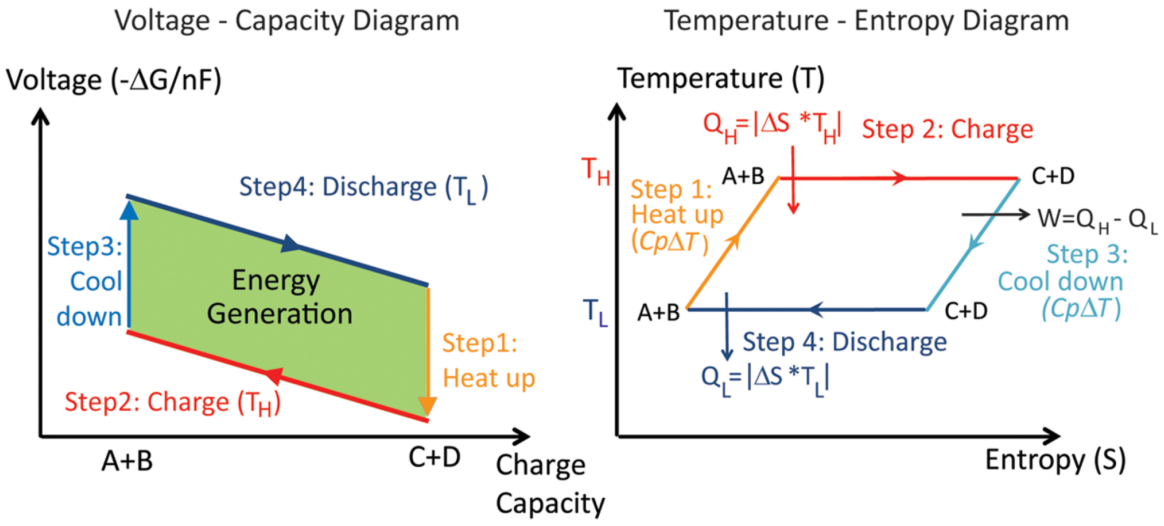

Figure 2.6: V-Q and T-S thermodynamic cycles of a TREC based device [3].

Even if the main framework is the same, several other similar mechanisms are studied.

Batteries or the supercapacitors can be also charged using a temperature gradient in the cell, or using a mix of thermal and electrical charge. It is so possible to modify the temperature of just one electrode in order to use the Seebeck effect to let the cell charge itself.

Other systems use membranes inside to limit the heat transfer or to modify the ionic motion. The problem with the membranes is that they are temperature sensitive and can lose effectiveness or be damaged by the high temperatures. The membranes can so be replaced by ion separators, which are less expensive ad more durable.

Moreover, several electrode-electrolyte interaction mechanisms can be chosen. A battery-type cell will use intercalation and chemical reaction of ions at the surface, instead, a supercapacitor-like cell will have more capacitive or pseudocapacitive mechanisms.

The advantages of these technologies are mainly in the efficiency that can be ideally calculated to be up to 50% of the Carnot efficiency. Some drawbacks are the cost and the maintenance of the membranes systems, the need for an external charge or the complex thermohydraulic design. These problems prevent the use in light and transportable applications such as cars or body heat recovery.

Some experimental examples of different devices proposed are listed below:

Author	**Year**	**Description**
Hartel [28]	2015	Supercapacitor with porous carbon electrode and organic electrolyte, immersed in a temperature changing fluid. Theoretical efficiency: 80% w.r.t. Carnot efficiency
Linford [29]	2018	$LiCoO_2/Li$ self-charging cells in two configurations, one with the cells under temperature gradient and one with the cells at the same temperature that varies with time. Efficiency: 0,22%
Reynold [30]	2018	New develop redox flow battery based with Vanadium salts in a heating-charging-cooling-discharging cycle obtaining an increase in energy density and efficiency of the battery
Yang [3]	2014	Membrane free $NiHCF$ cathode and $Ag/AgCl$ anode with cheat porous separator. Efficiency 30% w.r.t Carnot efficiency
Yang [31]	2014	External charging-free cycle with $Fe(CN)_6^{3-/4-}$ redox pair and solid Prussian blue which has the particular propriety of inversing the reaction under a certain temperature.
Atlas [32]	2018	Supercapacitor with one electrode at fixed temperature and the other at varying temperature keeping the potential difference with an external charge
Wang [33]	2017	Ionic thermoelectric supercapacitor with poly-electrolyte polystyrene sulfonate sodium
Zhao [34]	2016	Polymeric electrolyte supercapacitor charged with a temperature gradient

As stated above the examples reported are just a hint of the studies done on the topic, both theoretical thermodynamic cycles studies and experimental examples are present in literature.

Prospects

The advantages of liquid-based technologies with respect to the solid-state ones are multiple. Within the first years of research good power densities, efficiencies and cost-effectiveness are already developed.

A brief comparison can be made between these new technologies in terms of power den-

sity and efficiency (fig. 2.7). It can be noticed how the TRB, which are the newest are also the ones that now obtain the better (theoretical) performances. The theoretical efficiency is already at the levels of the solid-state materials, and it will only improve during the years. Focusing now on the TRECs, it is obvious that these efficiencies seem promising but a lot of work must be done in order to bring it to practical use. It is necessary to improve power density and reduce the cost of materials. The improvements in power density can be made by optimizing the cell configuration, charge concentration, and transport kinetics. In this context, a better physical model of the behaviour of these devices is needed.

This work aims so to develop a theoretical model that can describe the physical interactions inside a thermo-charged system, in particular a supercapacitor. This model must be sufficiently precise and simple, so that it can be used to optimize the supercapacitor, hoping that a further theoretical and numerical analysis permits to reach higher levels of power density and efficiency.

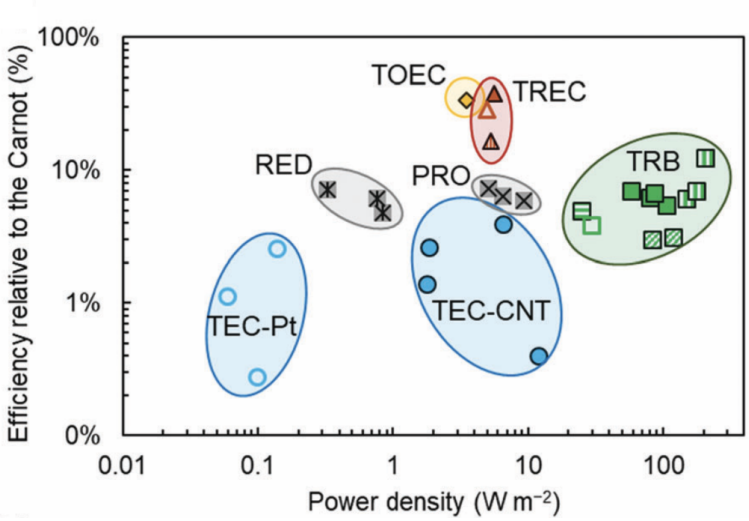

Figure 2.7: Comparison in terms of efficiency w.r.t Canot efficiency and power density of the various liquid-base thermoelectric technologies [4].

2.3 Thermocapacitive Systems

As stated above, within all the possible systems available that can extract electrical energy from a low-temperature heat source, this works focuses on the thermally regenerative electrochemical cycle techniques.

The proposed devices are usually based on capacitive systems such as batteries and capacitors. In particular, the electrical energy is extracted either using the difference in charging potential between a hot and a cold state, or using the voltage generated by the temperature difference between the electrodes. This last mechanism was used in the inspiring work of Zhao and al. and can be seen as a Seebeck-like coefficient in electrolytes [34]. There is however a main difference: a capacitive system under a temperature gradient creates a potential difference, but the current cannot flow continuously. Therefore,

energy storage devices can be recharged by a temperature difference, leading to the *thermocapacitive effect*.

The roots of this effect are to be found in the multiples phenomena governing the physics of charged liquids: diffusion, thermophoresis, electrophoresis, convection, dispersion, depletion forces, etc.

To understand the principles of these approaches is first necessary to analyse the energy storage systems available. This chapter aims so to depict the working mechanisms of an energy storage system so that it will be easier to understand the effects of a temperature gradient on them.

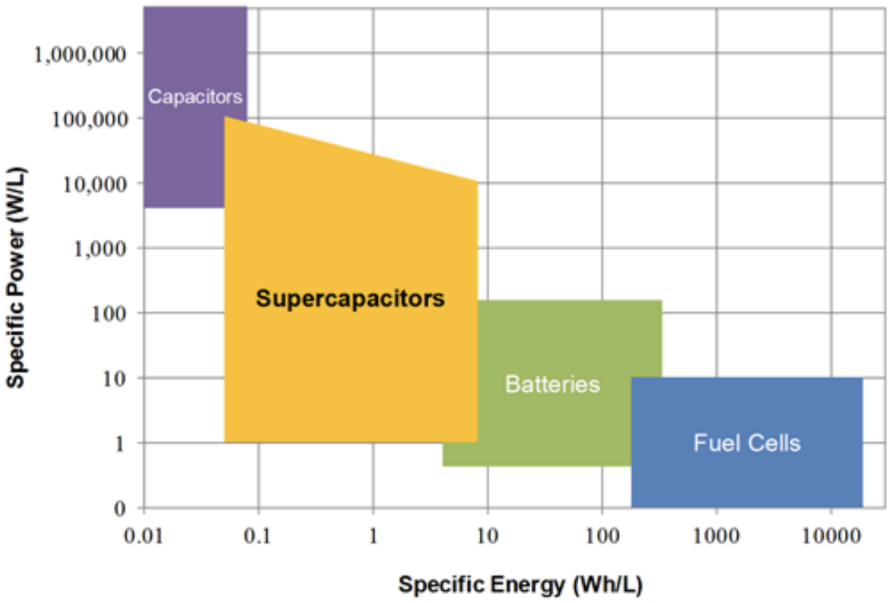

Figure 2.8: Ragone plot, the classic energy storage systems are compared in terms of specific power and specific energy.

The need for energy storage systems is growing in recent years due to the development of renewable energy sources that are aleatory and to the growing need for the automotive and IT sectors. The electrical energy can be stored directly in two ways: in batteries as chemical energy that require Faradaic oxidation and reduction, or in a non-Faradaic way as negative and positive charges on the plates of a capacitor. The former has large capacity but low specific power due to the slow kinetics of the redox reactions, the latter has low capacity but can deliver stored charges very rapidly as it is possible to see in the Ragone plot (figure 2.8).

2.3.1 Batteries

Batteries are the most used energy storage system, they are capable of store a good amount of energy per unit volume and are reliable for a high number of charge-discharge cycles.

They are usually made of two electrodes divided by a membrane that contains the electrolyte. During the charging cycle, the ions contained in the electrolyte are attracted

by the potential difference according to their sign. Once reached the electrode they react with it, changing their oxidation state, these compounds created are now stable and available to invert their oxidation state. This charged battery will have its own voltage and a maximum discharge rate. When the battery is then connected to an external load, the voltage difference between the two electrodes lets the compound counter-react and release electrons in the circuit and ions in the solution.

There are different types of batteries available now and countless ones in development. Depending on the goal it is necessary to choose the right type of battery. Considering that a part of them are not rechargeable (zinc-carbon, alkaline, metallic lithium) it is obvious that they cannot be useful for a TREC, which needs a high number of cycles without losing capacity. The origins of the impossibility to recharge them are in the non-reversible reactions that take place, it is therefore important to select the right type of reaction to have a compact and durable battery.

Other important characteristics to consider are the discharge power and the charging times. These values are related: the diffusion of the ions in the electrolyte and the reactions rates are the main factors to consider in order to improve those aspects. For the case of a thermally recharged battery, the time needed to charge the system is directly proportional to the thermal energy used, so it is a very important factor.

To give a complete description of a battery can be useful to explain the working principle of the most used ones. Lithium-ion batteries (LIBs) rely on ion intercalation rather then simple surface reaction. Intercalation is a physical phenomenon that can be described as ions of small sizes, such as the lithium ones, going into the various layer of layered materials. In particular, in the LIBs the anode is usually made by graphite powder and the cathode by a $LiCoO_2$ compound, both are 2D-layered materials. During the charging cycle, the lithium ions intercalate in the graphite with a reaction that can be described as

$$C_x + Li^+ + e^- \longrightarrow LiC_x$$

during multiples of these reactions, the LiC_6 compound is formed such that every graphite cell contains a lithium-ion. During the discharge, a similar intercalation happens in the $LiCoO_2$ cathode electrode. This battery has so a good charging rate thanks to this particular reaction, and the high energy density of the lithium ions makes it the most used in the world.

A specification must be made: the batteries commercially available are composed of thin foils of conductive materials and electrolytes wrapped in spiral form. This does not allow to apply directly a temperature difference, to be so studied for this scope it is also necessary to rethink the geometry of a battery, which creates other interesting challenges.

2.3.2 Supercapacitors

If the batteries use chemical reactions to store electrical energy, the supercapacitors are instead based on purely physical phenomena. The classical capacitors are made by two conducting plates divided by a dielectric, applying an external voltage, one side will have an excess of electrons and the other will have a deficiency. The energy is stored then in the electric field in the dielectric.

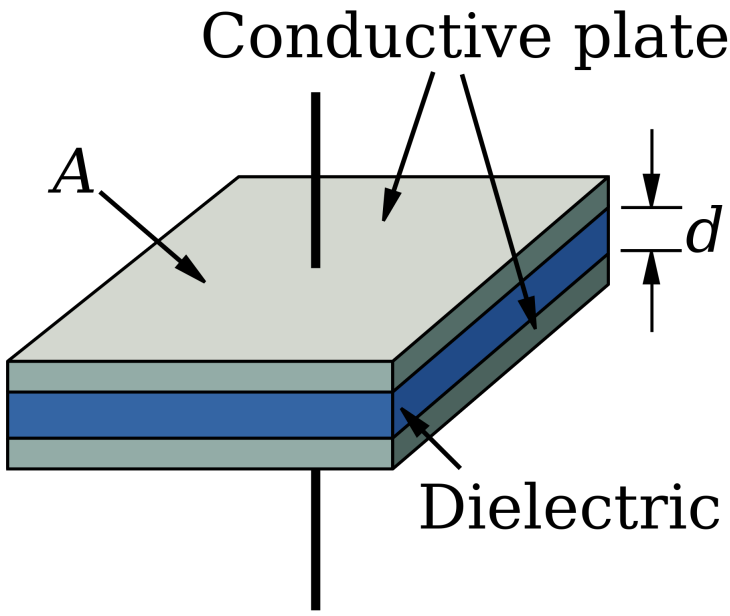

Figure 2.9: Sketch of a capacitor of area A and distance between the conductive plates d, separated by a dielectric.

The relation between the voltage applied (ΔV) and the charge accumulated (Q) is called capacitance (C), so that

$$Q = C\Delta V \tag{2.3.1}$$

In a planar capacitor as the one in figure 2.9 the capacitance can be simply calculated as

$$C = A\frac{\varepsilon}{d} \tag{2.3.2}$$

where d is the distance between the plate, A is the area of the capacitors, and ε is the total dielectric constant the is calculated as $\varepsilon = \varepsilon_0\varepsilon_r$: ε_0 is the void vacuum permittivity and ε_r is the relative permittivity of the dielectric material. These kinds of planar dielectric capacitors are only useful in electronic context because the energy that can be stored is limited.

In order to use the capacitors to store a good amount of energy for other scopes, such as cars, electrochemical capacitors were developed. Instead of a dielectric solid material an electrolytic solution is present between two electrodes. Imposing an external potential difference between the electrodes, the ions migrate towards electrodes according to their sign, but instead of reacting with the conductive parts, they remain on the surface, attracted by the surface charge. What is created at the interface between the electrodes and the electrolyte is called "*electric double layer*" (EDL) which is a well defined-structure created by the ions in this conditions. This EDL is the most important part of the capacitor because it is the zone in which the charges accumulate and the electrical energy is conserved. The precise physical description of the structure and the properties of an EDL will be carried out in the next chapter, but in order to understand the behaviour of a supercapacitor is necessary to give a simple phenomenological description.

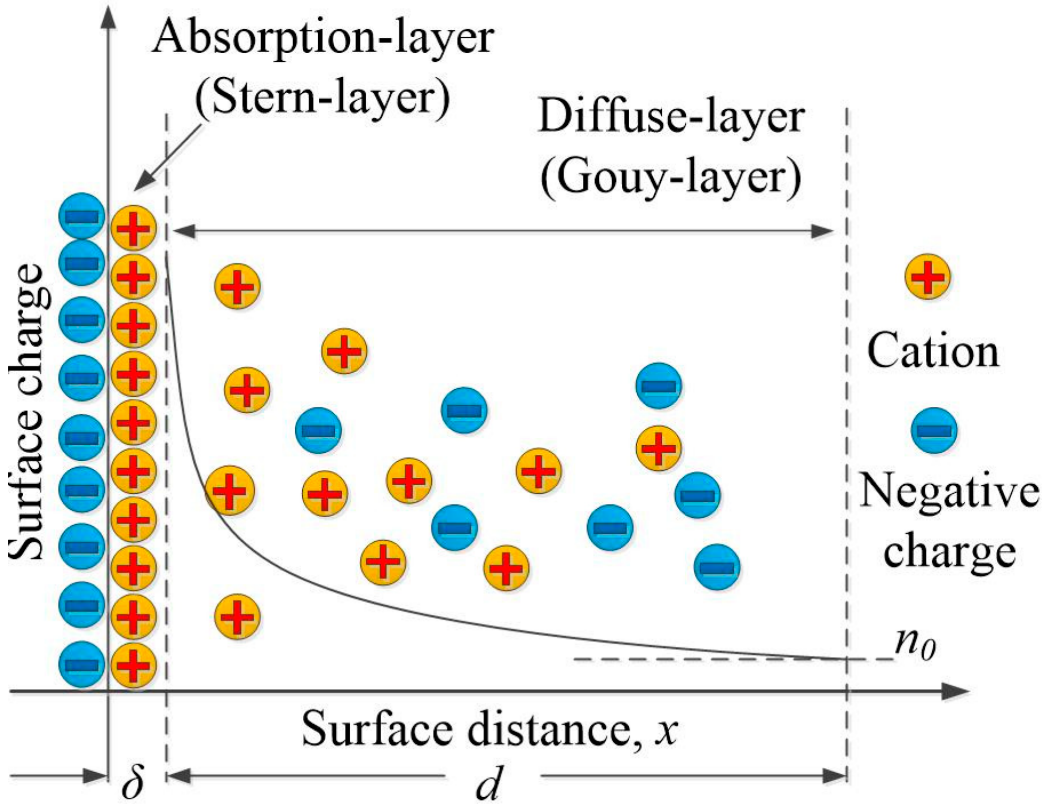

Figure 2.10: Sketch of an EDL created by a negative charged surface in contact with an electrolyte. It is possible to visualize the Stern layer of thickness δ and the diffuse layer which charge density decays in the distance d.

In general, when a charged object is placed in an electrolyte, the electric field it generates will attract the ions of opposite charge with respect to the surface charge of the object (counter-ions). When the system reaches equilibrium near the charged object there will be a charged cloud of ions that, in general, will counterbalance the surface charge. This zone of the electrolyte it is the *diffuse layer*. Depending on the characteristic of the electrolyte (type of solvent and ions and concentration) different theories explain the phenomena mathematically.

One of the first that was developed is based on the Poisson-Boltzmann equations and the results for both the potential and the ion densities result in exponential-shaped functions. Thus, the potential decays from the value that it has on the surface to the bulk potential with a precise characteristic length. This length is called *Debye length* and, if the ions in the solution have the same valency z, it can be calculated as:

$$\lambda_D = \sqrt{\frac{\varepsilon k_B T}{2e^2 n_0 z^2}} \tag{2.3.3}$$

where k_B is the Boltzmann constant, e is the electron charge and n_0 is the bulk ion concentration. Also a Stern theory exists, which is visible in figure 2.10, that includes also a layer of adsorbed ions at the surface which length (in this case δ) is the diameter of the ions and its solvation shell. In fact, it must be remembered that the charged ions in a

polar solvent will attract strongly the solvent molecules on them creating a sphere which radius include also the molecule's dimension.

A capacitance of the diffuse layer can be defined as well because the quantity of charges inside of it is proportional to the potential difference between the electrode and the bulk fluid. The simplest way to model the EDL capacitance is to imagine it as a capacitor with plates at a distance λ_D so that the capacitance of the single EDL is

$$C = A\frac{\varepsilon}{\lambda_D} \tag{2.3.4}$$

This model of capacitance only holds for dilute solutions, more complex descriptions are needed if the ions cannot be considered dilute.

A planar electrode electrochemical capacitor can then be thought of as an electrical circuit composed by a resistance R, that accounts for the ion limited mobility in the electrolyte, and two capacitors with capacitance C representing the EDLs. This model is called "*equivalent electrical circuit*" (EEC) and it is commonly used in electrochemistry to model dilute solutions.

Finally, a supercapacitor is simply an electrochemical capacitor with nanostructured electrodes. This electrodes permit the capacitor to have a very high electrode surface area. Usually, nanoporous carbon electrodes are used, they can provide a surface area exceeding 1000 m^2g^{-1}. The supercapacitors, as can be seen in figure 2.8, have high power densities and good charge-discharge rates, with an industrial-scale useful energy density. The absence of the reactions at the electrodes permits an almost indefinite use of the device because the process is quasi completely reversible. These devices are usually implemented in couple with lithium-ion batteries to realize high energy - high power systems.

Nanoporous Electrodes

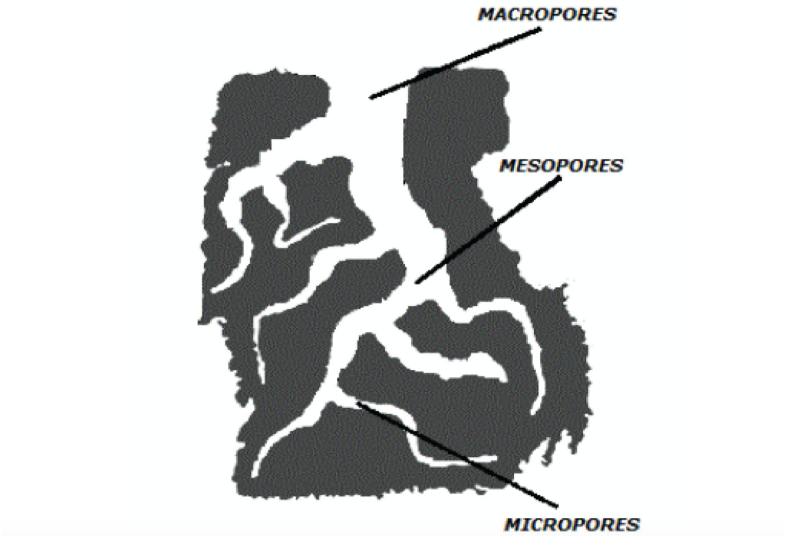

Figure 2.11: Sketch of a the nanopores present usually in a nanoporous carbon electrode.

Specific attention must be paid to the structure of a nanoporous electrode. Remembering that the electric double layer is formed only on the surface of a conductive medium in an

electrolyte, it is trivial to realize that it is important to have the higher possible specific surface area in an electrode to maximize the presence of double layers and consequently the capacitance of the device. To do so, nanostructuring an electrode with a large network of interconnected holes permits the optimization of the specific surface area, preserving an optimal electrical conductivity of both the electrolyte and the electrode. The process is made possible from the enormous technological advancements made in the last years in the nanotechnology field, leading to cheap and size controllable nanoporous electrodes.

The carbon nanoporous electrodes are produced in different forms [35]. The most common ones are: activated carbon, produced from physical or chemical activation of carbonaceous materials, carbon nanotubes, which are deposited after the formation in solution, templated carbon, which offers well-controlled narrow pores size, and other less used carbon structures as carbon aerogels.

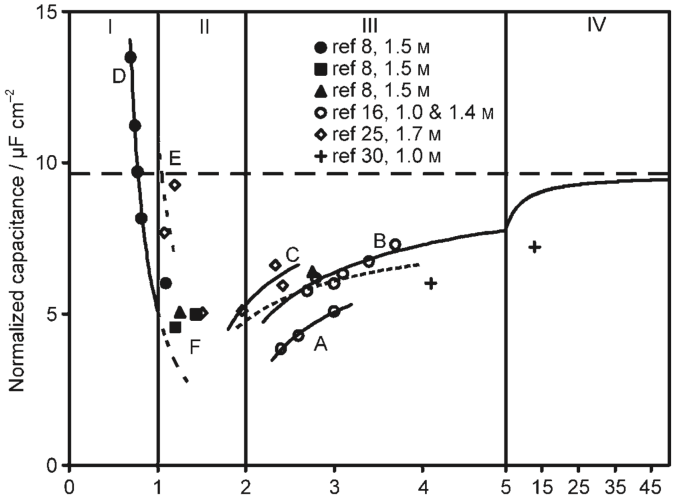

Figure 2.12: Experimental data from and fitting curves from ref [5], the normalized capacitance vs the average pore size of a nanoporous electrodes are represented.

The pore can be classified in macropores, mesopores and micropores which have respectively average dimensions over 50 nm, between 50 nm and 2 nm and under 2 nm. The capacitance of the device can be so studied by modifying the average pore size, obtaining the results in figure 2.12. These results underlined the fact that when the pore size it is under 5 nm the normalized capacitance (so taking into account the fact that the surface area changes) it is reduced because the electric double layers cannot be fully developed. When the size goes under 1 nm instead the normalized capacitance grows, this seems to originate from the presence of a single ion species in the pore that it is not screened by the counter-ions that are physically blocked by the pores [5].

The number and the size of the nanopores affect the charging time, in particular, it is known that a supercapacitor with a high number of pores takes a long time to be charged, as it is possible for example to see in the experiment of Janssen and al.[36].

The model that explains these results, and in general a model that describes a nanoporous carbon device, is not unique. The models are optimized for different times and length scales, for example, it is possible to use a molecular dynamics model to

understand the precise interaction between the electrolyte and the carbon structure, but the simulation is confined in a few nanometres [37]. To understand, instead, the overall capacitance a good method is to calculate the pores-electrolyte interaction with classical density functional theory [38] and average it on the entire electrode [39].

The simulation techniques expressed so far are not useful in the charging time calculations. The reason for the slow charging of a supercapacitor is still not completely modelled, but a good approximation was done by Lian and Co [40]. Starting from the transmission line (TL) models [41], in which the pores and the electrolyte in between are represented respectively by series of capacitor in parallel and by a linear resistor, they modified the system, in order to have a direct interpretation of the microscopic properties of the supercapacitor. In particular, the TL models fit the curve with experimental data, instead, the *stack-electrode model* (SEM) of Lian and Co, use a series of planar permeable electrodes posed at a distance h that represent the pores mean size.

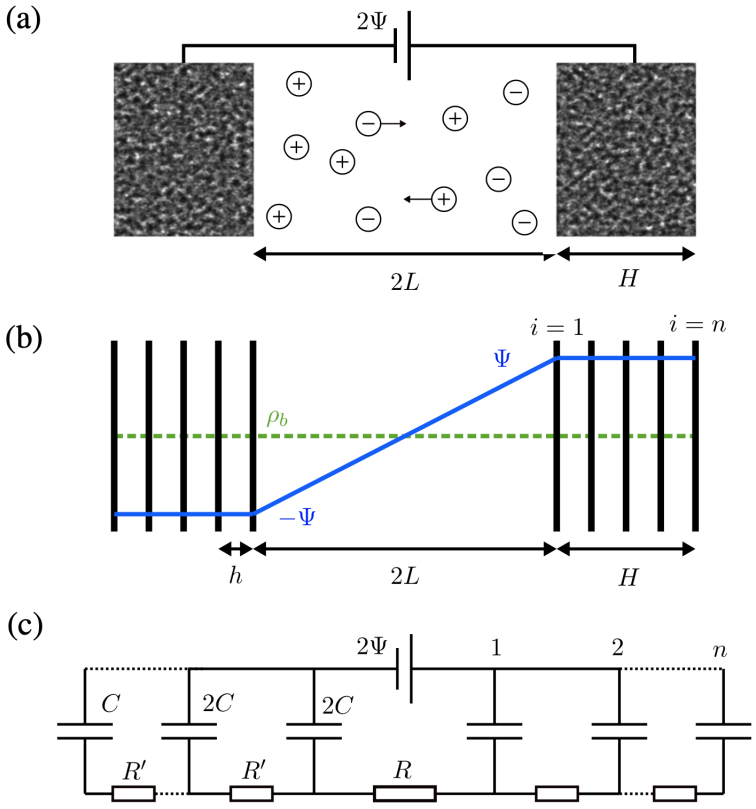

Figure 2.13: (a) Sketch of a supercapacitor containing 1:1 electrolyte, the porous electrodes and an external power source providing a potential difference of 2Ψ*. (b) Stack electrode model sketch in which the* n *electrodes per side are divided by the distance* h*, stating from* $\pm L$ *and reaching* $\pm L \pm H$*. The initial ions concentrations are* ρ_b *for both anions and cations (green dashed line) and the time 0 applied potential* $\pm\Psi$ *(blue line). (c) Equivalent electrical circuit with reservoir resistance* R*, pore resistance* R'*, electrode capacitance* $2C$*, a part from the last electrode of capacitance* C*.*

The model is physically explained by a macropore that goes from the reservoir to the end of the electrode with a series of parallel micro or nanopores perpendicular to it. It is so

possible to understand microscopically the behaviour of a supercapacitor during charging, expanding then the results for a macroscopic system. Being also a one-dimensional model the visualization of the space dependants motion of the ions permits to grasp the physical reason for the slow charging times. The calculations are also made easier developing an equivalent electrical circuit, that works similarly to the TL models, but the values of the capacitance and the resistance are calculated from the physical governing equations of the electrolyte, giving the possibility to model in principle every type of supercapacitor just changing the electrolytes and geometrical parameters.

The EEC of the SEM permits so to calculate the charging time as a function of the number of electrodes n, so the number of pores, the size of the pores h, and the ratio between the part occupied by the nanoporous electrode and the reservoir part H/L. The function found is

$$\tau_n = \frac{L\lambda_D}{D} \cdot \left[\left(2 + 0.75\frac{H}{L}\right) n - 1 - 0.91\frac{H}{L}\right] \tag{2.3.5}$$

This value is found solving the ordinary differential equations system the solution of the circuit in figure 2.13 creates. It must be stated that the time calculated, even if much closer than the rest of the methods, does not match the experimental results quantitatively. In particular, the τ_n found is one order of magnitude less than the experimental one. These results are however satisfying, mostly because, in principle, the model can be improved if a more profound understanding of the diffusivity and the permittivity of the electrolyte in the electrodes will be developed. With these improvements the SEM is able to simulate a very complex system such as a nanoporous carbon electrode in an electrolyte. The SEM will be essential to the aim of this work because being a one-dimensional model permits to simulate the behaviour of the ions throughout the length of the cell. This makes it easy to impose a temperature difference between the electrodes and so simulate a thermal charging.

2.3.3 Thermo-charging

Once the energy storage devices are explained, it is relatively simple to understand what happens when a temperature gradient is imposed across them.

To be more precise, it is necessary to explain the physical origin of the motion of the ions in a temperature gradient: the Soret effect. The Soret effect can be described phenomenologically as the motion of particles driven by a temperature gradient. The nature of the of the particle-solvent interaction is responsible for this effect. The majority of the particles are pushed by the Soret effect towards the colder side of the system. There are exceptions to this behaviour because the totality of the phenomena happening is more complicated and not totally known. However it will be discussed within the limits of the current knowledge in the next chapter. With this notions is however possible to describe the concept of thermo-charging, which differs from the thermoelectrochemical cells explained before. If the TECs rely on the entropy difference in the reactions, a thermo-charged battery or supercapacitor are moved only by the Soret effect, but the mechanisms at the interface are different.

The battery-type electrochemical cells are composed of two electrodes made of the

same active material and an electrolyte with one ionic specie. This material can also be a layered material in which the ions intercalates. The intercalation is driven by the temperature difference: simplifying, the Soret effect drives the ions to the cold electrodes and the chemical potential created allows the intercalation and the reaction. The battery results now charged, so that the energy used to establish the temperature difference is now stored as electrochemical energy, the battery can so be used as a current generator. The Seebeck-like coefficients of these processes go from -6.8 $\mu V K^{-1}$ up to -29.7 $\mu V K^{-1}$[42]. These mechanisms promise possible high charging efficiency once the other parameters are optimized.

The thermally-chargeable supercapacitors work differently. Due to the charged nature of the ions and the difference in their Soret motion, an electric potential difference can be measured between the hot and the cold electrode. This can so be classified as a Seebeck-like effect. So that when a temperature gradient is applied a potential difference and a non-neutral zone are created near the electrodes. Then when the circuit is closed, and the electrons can flow to equilibrate the charge unbalance, an EDL is formed on the surface, and the supercapacitor results charged. Some experiments were made regarding this phenomena and are listed in a review from Al-zubaidi and al. [43]: Qiao 2008 [44], Lim 2013 [45], Lim 2018 [46], Bonetti 2015 [47], Zhao 2016 [34], Kim 2016 [48]. To understand the choice of focusing in particular to the thermo-charging of a supercapacitor is useful to review a particular experiment.

Analysis of a TREC with a supercapacitor

Zhao and al. experimentally evaluated the efficiency of a TREC using a supercapacitor [34]. The supercapacitor was composed of a polymeric electrolyte based on polyethyleneoxide (PEO) treated by $NaOH$ posed in between two electrodes.

The PEO-$NaOH$ was characterized and a Seebeck coefficient of 11.1 $mV\ K^{-1}$ was measured. This value is remarkably high with respect to the usual Seebeck coefficients values found in literature, and it is origin are not well explained by the few physical relations known.

The electrodes were also structured and characterized. Three kinds of electrodes were used: planar gold electrode, a thin carbon nanotubes electrode and a thick carbon nanotubes electrode. The carbon nanotubes posed on the gold electrode improve the surface area and so the capacitance of the device. The capacitances C of the various electrodes were measured with classical electrochemical methods such as impedance spectroscopy and cyclic voltammetry. These characterizations revealed a leakage current present (that can be modelled as a parallel resistance R_p) and gave also the values for the equivalent internal resistance of the electrolyte (R_s).

Once the system was known it was charged in two ways: the first was a simple charging from an external voltage applied ΔV_{ext}, and the second was a thermo-charging, with a temperature difference that generated the same voltage $\Delta T = \Delta V_{ext}/S_e$.

To be more specific PEO-$NaOH$ has a particular characteristic: the OH^- ions remain absorbed in the polymer, letting only the Na^+ diffuse and so be affected by the Soret effect. This means that the cold side will be full of positive ions.

The thermo-charging process was divided into four phases:

i) A temperature gradient is applied over the supercapacitor, maintaining the electrodes isolated. This moves the ions present in the electrolyte towards the cold side and, to balance the charge accumulation, a voltage difference is established and measured with an external voltmeter $V_{thermo} = S_e \Delta T$. The fact that the electrodes are isolated means that no charge is accumulated inside of them.

ii) Charging phase: keeping the temperature difference applied the electrodes are connected through a load R_{load} and the thermo-voltage is used to charge the supercapacitor. Having now the possibility to move, the electrons go into the cold electrode and create a surface charge. This consequently let the positive ions minimize their energy creating an EDL. The supercapacitor can be now considered charged. The detected presence of the leakage current does not allow the measured potential difference to go to 0, limiting the efficiency of the cycle. Without this leakage current, the final condition would be a short circuit condition in which the potential difference is 0 and no current flows.

iii) Once the electrodes are charged the load is disconnected, creating an open circuit condition, and the heater can be switched off. The charge that remained in the electrodes will now be stored and can be used for generating electrical power.

iv) When the supercapacitor is connected to a load it will discharge returning to the initial condition.

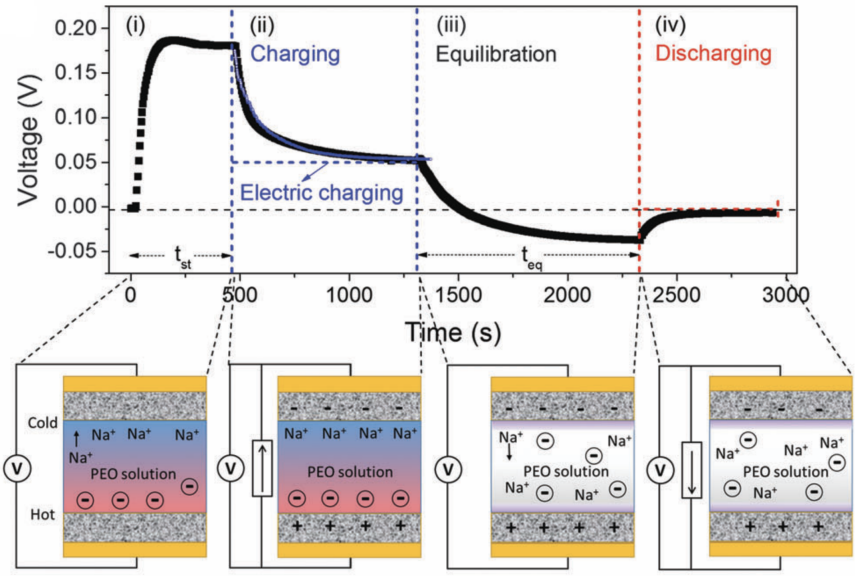

Figure 2.14: Graph of the voltage measured across the supercapacitor in the various phases of the experiment. The internal behaviour of the supercapacitor is also sketched.

The thermally regenerative electrochemical cycle is now completed.

The voltage difference across the device is recorded and it is compared to the charging behaviour of the supercapacitor charged with the external ΔV.

As it is possible to see in figure 2.14 the voltage vs time curves coincide, this means that it is possible to consider the thermo-voltage as an effective potential generator inside the supercapacitor. An equivalent circuit is so modelled.

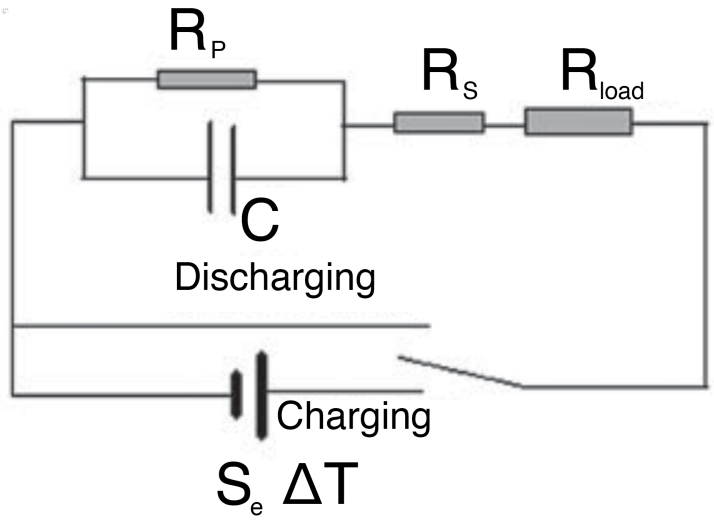

Figure 2.15: Circuit used to model the charging behaviour of the supercapacitor under a temperature gradient.

From this circuit is possible to simply calculate the efficiency, considering the leakage current too. Solving the circuit, the effective voltage difference $V_{effective}$ that can be used in the discharging phase is

$$V_{effective} = S_e \Delta T \left(1 - \frac{R_{load} + R_s}{R_{load} + R_p + R_s}\right) , \tag{2.3.6}$$

and the total charge accumulated is

$$Q_{ch} = C V_{effective} \tag{2.3.7}$$

During phase iii a self-discharge mechanism was detected, with the final charge accumulated before the discharging measured to be 27% of the Q_{ch}, lowering further the efficiency. Considering this factor the final potential difference across the cell after phase iii ($V_{equilibration}$) is far less than the original thermo-voltage. The electrical energy accumulated is so $E_{el} = 1/2 C V^2_{equilibration}$.

The thermal energy required to charge the capacitor $E_{thermal}$ can be calculated by integrating the thermal flux during the time required to complete phases i and ii and summing the heat absorbed by the electrolyte, neglecting other contributions.

The ratio between the two energies is the efficiency of the cycle, the measured efficiency is $6 \cdot 10^{-6}\%$. It is important to consider that the device is not optimized, so the heat used in phase i is not the minimum possible and the leakages can be improved with better dynamics optimization and materials choice. An optimized device can reach an

efficiency of 0.1%, which is not commercially useful, but it is 2500 times higher than that of a supercapacitor charged with the potential obtained by a standard thermoelectric generator. Moreover, this is one of the first experiments in the field, and both electrolytes and electrodes can be improved with the goal to obtain higher Seebeck coefficients, lower thermal conductivity, lower charging times, and higher ionic conductivity.

This experiment is particularly important to the aim of this thesis because the pure physical behaviour of the system, without important chemical reaction, permits to isolate the phenomena. In particular, the precise thermo-diffusion of the ions can be understood and modelled with the equations governing the behaviour of an electrolyte in a thermal gradient.

The main problem is on the nature of the Seebeck coefficient in polyelectrolytes which is not known yet. It is then convenient to start analysing the behaviour of a supercapacitor with aqueous solvent, so that the larger literature on the Seebeck effect in this field can be used as starting point.

Theoretical Framework

To complete the background necessary to fully understand the results of the present work, here is presented an overview of the basic physical phenomena that take place in an electrolyte subjected to a temperature gradient or an applied electric potential.

3.1 Electrostatics in charged fluids

If a charged object is posed in a polar liquid containing ions, the ions with opposite charge with respect to the surface charge present on the object (*counterions*) will be attracted by its surface, but for entropic reasons, they have also a tendency to distribute as homogeneously as possible [6]. The balance between the electrostatic and the entropic effects creates the so-called *electric double layer* (EDL). It consists in a well-localized charge and a diffusely distributed cloud of ions with a typical thickness, called *Debye length*.

The structure of the EDL and the nature of the phenomena it produces are well studied with a variety of theories. The most important works are form Guoy [49], Chapman [50], Debye nd Huckel [51]. The first and more simple solutions are based on mean-field theories that ignore ion-ion correlations, the modern and more complete ones utilize innovative methods like classical density functional theory [52] or molecular simulations [53].

This work aims to develop a basic model of thermoelectricity in electrolytes, so the mean-field theories are sufficient to describe the system and they are so used and explained below.

The Poisson-Boltzmann Equation

Considering now a planar homogeneous impenetrable surface of area A in a plane in $z = 0$, in contact with a solvent in the half-space $z > 0$, it is possible to calculate the behaviour of the ions in the solvent once the surface charge density σ is known, the function of the surface charge density is so $\sigma\delta(z)$. The solvent is viewed as a structureless medium of dielectric constant $\varepsilon_0\varepsilon_r = \varepsilon$ and temperature T, and the solute is composed by monovalent pointlike (no finite-size effects) cations and anions of charge $\pm e$ with a concentration n_0. The calculation aims to find the electrostatic potential $\phi(z)$ and the ionic density profiles $n_\pm(z)$. The system can be modelled with a set of three equations. The first links the potential of the system with the charges present in it, it is called *Poisson equation*:

$$\varepsilon\nabla^2\phi = -Q_{ext} - e\sum_i z_i n_i \tag{3.1.1}$$

where Q_{ext} is an external charge and, in general, ez_in_i are the products for every specie i of valencies z_i, the electron charge e and the local number density n_i.

For the purposes of the one-dimensional problem, with two ions species of valency $z = \pm 1$ and no external charge, the Poisson equation can be restated as

$$\frac{\partial^2\phi}{\partial z^2} = -\frac{e}{\varepsilon}(n_+(z) - n_-(z)) \tag{3.1.2}$$

The next relations are the *mean-field Boltzmann distributions* of the ions:

$$n_\pm(z) = n_0 \exp\left[\mp\frac{e\phi(z)}{k_BT}\right] \tag{3.1.3}$$

To solve the problem two boundary conditions (BCs) are needed. The need for the ionic densities of reach, far from the plane ($z \to \infty$), the initial concentration n_0, translates into

$$\lim_{z\to\infty} \phi(z) = 0 \tag{3.1.4}$$

The global charge neutrality expect moreover that the total ionic charge is the exact opposite of the total charge on the surface:

$$\sigma = -\int_0^\infty e(n_+(z) - n_-(z))dz = \varepsilon\int_0^\infty \frac{\partial^2\phi}{\partial z^2}dz = -\varepsilon\left.\frac{\partial\phi}{\partial z}\right|_{z=0^+} \tag{3.1.5}$$

The relations (3.1.2)-(3.1.5) form a closed set of equations for $\phi(z)$ and $n_\pm(z)$. In particular the last one is important to calculate the charge density of the surface knowing the potential function and vice versa. It is convenient to introduce the dimensionless potential $\psi(z) = e\phi(z)/k_BT$ so that the Poisson-Boltzmann equation (PB) and its boundary conditions (B.C.s) can be cast in the form

$$\frac{\partial^2\psi}{\partial z^2} = \kappa^2 \sinh\psi(z)\,, \tag{3.1.6}$$

$$\psi(z \to \infty) = 0\,, \tag{3.1.7}$$

$$\left.\frac{\partial\psi}{\partial z}\right|_{z=0^+} = -\frac{e^2\sigma}{\varepsilon k_BT}\,, \tag{3.1.8}$$

with the *screening length* $\lambda_D = \kappa^{-1}$, also called Debye length defined by

$$\lambda_D = \sqrt{\frac{\varepsilon k_BT}{2e^2n_0}} \tag{3.1.9}$$

The Debye length λ_D is, for a given solvent and temperature, a function of the salt concentration n_0, and it sets the length scale over which charge imbalance can persist. To give a sense of the value of this parameter, if a solution with a concentration of $1\,mM$ is taken, the Debye length results $9.6\,nm$.

The nonlinear Poisson-Boltzmann problem in equations (3.1.6)-(3.1.8) can be solved analytically, finding the Guoy-Chapman solution

$$\psi(z) = 2\ln\frac{1 + \gamma\exp[-\kappa z]}{1 - \gamma\exp[-\kappa z]} \tag{3.1.10}$$

where γ is an integration constant fized by the surface charge so that

$$\frac{4\gamma}{1-\gamma^2} = \frac{\sigma}{\sqrt{2\varepsilon k_B T n_0}} \equiv y \tag{3.1.11}$$

The variable y can be seen as a dimensionless surface charge density and it is useful because with a simple calculation it can be seen that the far-field (κz) solution for small $y << 1$ is simply

$$\psi(z) = y \exp(-\kappa z) \tag{3.1.12}$$

The ion density profiles are so

$$n_{\pm}(z) = n_0 \left(\frac{1 \mp \gamma \exp(-\kappa z)}{1 \pm \gamma(-\kappa z)} \right)^2 \tag{3.1.13}$$

From these solutions, it is shown that the Debye length λ_D sets the length scale of the decay of both the potential and the ionic densities.

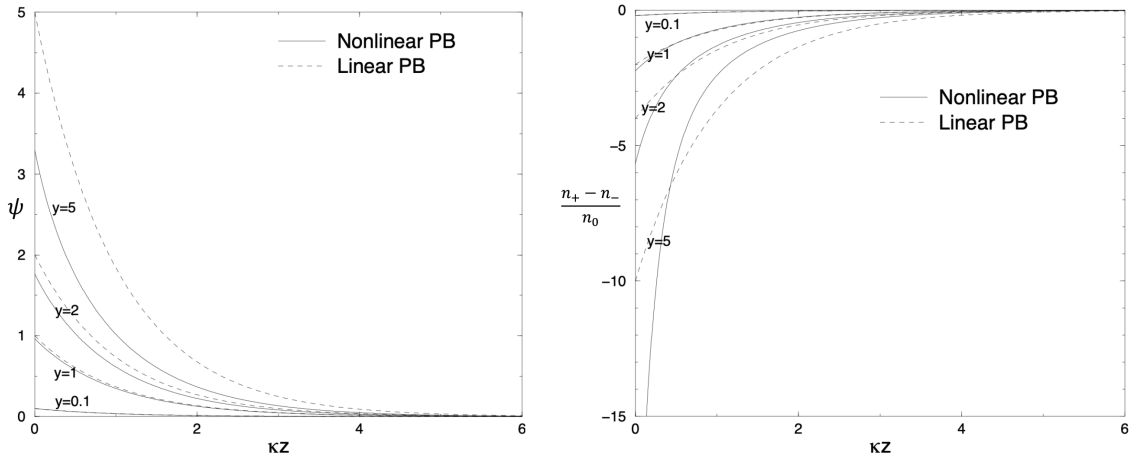

Figure 3.1: Dimensionless electrostatic potential ϕ and charge density $(n_+ - n_-)/n_0$ as obtained from the nonlinear and the linear PB equations for different values of dimensionless surface charge y. It can be notice how the linear solution is accurate only for $y < 1$. [6]

The geometry chosen, a single charged planar wall, is the only geometry from which the analytical solution can be found exactly. The other geometries create nonlinear Poisson-Boltzmann sets of equations which must be linearised for small absolute values of the dimensionless potential $\psi(z)$. The equation (3.1.6) can so be written as

$$\frac{\partial^2 \psi}{\partial z^2} = \kappa^2 \psi(z) \,, \tag{3.1.14}$$

which can now be solved not only for an imposed surface charge, but for an imposed potential difference between the electrolyte and the electrodes. So if the electrolyte is considered at 0 potential and the electrode is posed at ψ_0 the solution of the previous equation is simply $\psi(z) = \psi_0 \exp(-\kappa z)$. This trivial solution is important because from

it it is possible to calculate what is the surface charge that the electrodes accumulates deriving it in $z = 0^+$, so from equation (3.1.5) which always holds,

$$\sigma = -\varepsilon \left.\frac{\partial \psi(z)}{\partial z}\right|_{z=0^+} = \varepsilon \kappa \psi_0 \,, \tag{3.1.15}$$

Recalling the concept of capacitance of equation 2.3.1 the capacitance of the EDL is demonstrated to be

$$C = \frac{\partial \sigma}{\partial \psi_0} = \frac{\varepsilon}{\lambda_D} \tag{3.1.16}$$

Advanced EDLs Models

As stated above, the Poisson-Boltzmann solution, and in particular the linearised one, it is valid only for small potentials and low salt concentration. The structure and the properties of the EDL are more complicated and some models are summarized below, so that a clearer picture of the system is depicted.

Remaining in the Gouy-Chapman approximation a more complete calculation of the capacitance of the EDL reveals that the former it is not independent on the potential applied. In particular, it is possible to demonstrate the capacitance is proportional to $\cosh \psi_0$. For low potentials, this term is approximable to 1, but when the potential grows it is no more valid. This model's limits are consistent, it is in fact easy to see that for a high value of ψ_0 the capacitance grows indefinitely. This comes from the pointlike ion approach that permits an infinite number of ions to be accumulated at the surface. In the real system, the ion's volume or the volume of the ion and its solvation shell (the polar solvent it is attracted by the charge) prevents the ions to reach certain densities.

An important improvement can be found in Stern's theory for the EDL. He united the primitive Helmholtz concept of a compact layer of counterions that fill the charged surface, with the diffuse layer found above. This approximation is valid when the potential is high enough to attract almost an entire layer of ions on the surface, it has its own capacitance dependent on the thickness of the layer itself (so the radius of the ions plus solvation shell). The rest of the electrolyte behaves as depicted in the PB theory with a maximum potential that is reduced by the Helmholz layer. The final capacitance will be modelled as two capacitors in series.

In the case of a high concentration of ions the pointlike approximation fails completely in the capacitance calculations. To overcome this barrier different methods are used. The simpler ones maintain the mean-field approach adding simply a repulsive hard-sphere term. These methods are called Modified Poisson-Boltzmann methods [54]. The most precise one is the Carnahan-Starling model which considers a steric force of

$$\boldsymbol{F}^{CS} = -k_B T \frac{8 - 2\chi}{(1-\chi)^4} \nabla \chi \tag{3.1.17}$$

where χ is the volume fraction of the ions. This model reproduce the experimental results of the capacitance in the range of $\chi \sim 0.5$ and $\phi \sim 0 - 200\, mV$.

The most precise and modern approaches overcome the mean-field theories and use the classical density functional theory to calculate the density profile of the ions in proximity of a charged surface. This approach is based on the iterative minimization of the grand-canonical potential and it permits to find the correlations between the positions of the ions and to apply a more precise hard-sphere potential. The results are very precise and usually reproduce the molecular simulations with far less numerical operations. it is so used to model ionic liquids, which high concentrations require advanced methods [52].

The summary of the models that explain the behaviour of the EDLs has just an informational purpose, in this thesis, the potentials and the concentrations are sufficiently low to permits the PB solution to hold.

3.2 Irreversible Thermodynamics

The phenomena that are present in this thesis are out of thermal equilibrium. This implies that the equilibrium thermodynamics cannot describe the system in analysis, it is so necessary to complete the theoretical framework with some basic concepts on irreversible thermodynamics.

Starting from the first principle of thermodynamics for a mono component system of N particles in a volume V, pressure p, temperature T, chemical potential μ and internal energy U

$$dU = TdS - pdV + \mu dN \,, \tag{3.2.1}$$

isolating the entropy S,

$$dS = \frac{dU}{T} + \frac{pdV}{T} - \frac{\mu dN}{T} \,, \tag{3.2.2}$$

applying then the concept of local equilibrium, so analysing what happened in the small volume dV

$$ds = \frac{1}{T}du - \frac{\mu}{T}dn \,, \tag{3.2.3}$$

where s is the entropy per unit volume and n is the number of particle per unit volume. ds can be seen as sum of a *generalized force* $F_k = \frac{ds}{dx_k}$ ($\frac{ds}{du} = \frac{1}{T}$; $\frac{ds}{dn} = -\frac{\mu}{T}$) times an extensive parameters dx_k:

$$ds = \sum_k F_k dx_k \tag{3.2.4}$$

Defining now a flux of entropy, $\boldsymbol{J}_s$, the previous formula lead us to

$$\boldsymbol{J}_s = \sum_k F_k \boldsymbol{J}_k \tag{3.2.5}$$

In which $\boldsymbol{J}_k$ is the current density of the extensive parameter x_k. In the same way an entropy production can be defined as $\sigma_s = \frac{ds}{dt}$ obtaining

$$\sigma_s = \frac{\partial s}{\partial t} + \nabla \cdot \boldsymbol{J}_s \tag{3.2.6}$$

It can be notice how the irreversible phenomena that take place in the volume dV increase the entropy of the system. If the extensive parameter of interest are conserved, for the continuity equation

$$0 = \frac{\partial x_k}{\partial t} + \nabla \cdot \boldsymbol{J}_k \tag{3.2.7}$$

Using the previous definitions and equations it is easy to see how σ_s can be written as

$$\sigma_s = \sum_k \nabla F_k \cdot \boldsymbol{J}_k \tag{3.2.8}$$

The ∇F_k are called *thermodynamic affinities*, written usually as χ_k, and they can be calculated, as done before, from the entropy production of the system. For a purely resistive system, by definition, each local flux depends on all the local affinities and upon the local intensive parameter $J_k = J_k(\chi_1, \chi_2, \ldots, \chi_j, \ldots; F_1, F_2, \ldots, F_j, \ldots)$.

In particular in linear or linearised systems

$$\boldsymbol{J}_k = \sum_j L_{jk}\chi_j \ , \tag{3.2.9}$$

when L_{jk} is known as *kinetic coefficient* and it is a function of the local intensive parameter. A matrix that connects the fluxes $\boldsymbol{J}_k$ and affinities χ_j is so created with the kinetic coefficients L_{jk} as elements.

For the *Osanger theorem* it is possible to state that

$$L_{jk}(\boldsymbol{B}_e) = L_{kj}(-\boldsymbol{B}_e) \ , \tag{3.2.10}$$

when $\boldsymbol{B}_e$ is the external magnetic field. For our purposes the external magnetic field is always 0 so the matrix of the kinetic coefficients is symmetrical.

Thermoelectric Effects

Recalling equation (3.2.8), for the case considered in equation (3.2.3), it becomes

$$\sigma_s = \nabla\frac{1}{T} \cdot \boldsymbol{J}_u - \nabla\frac{\mu}{T} \cdot \boldsymbol{J}_n \tag{3.2.11}$$

So the affinities are $\nabla\frac{1}{T}$ and $\nabla\frac{\mu}{T}$. Assuming a single component flux in direction x the linear laws become

$$-\boldsymbol{J}_n = L_{nn}^{'}\nabla\frac{\mu}{T} + L_{nu}^{'}\nabla\frac{1}{T} \tag{3.2.12}$$

$$\boldsymbol{J}_u = L_{un}^{'}\nabla\frac{\mu}{T} + L_{uu}^{'}\nabla\frac{1}{T} \tag{3.2.13}$$

In analogy with the fundamental relation $dQ = TdS$ we can define

$$\boldsymbol{J}_Q = T\boldsymbol{J}_s \ , \tag{3.2.14}$$

and so by equation (3.2.5),

$$\boldsymbol{J}_u = \boldsymbol{J}_Q + \mu\boldsymbol{J}_n \tag{3.2.15}$$

With the current definition of the internal energy flux the entropy production of eq. (3.2.11) can be recalculated so that new affinities are found , it is so possible to rewrite the equations (3.2.12) and (3.2.13) as

$$-\boldsymbol{J}_n = L_{nn}\frac{1}{T}\nabla\mu + L_{nq}\nabla\frac{1}{T} \tag{3.2.16}$$

$$\boldsymbol{J}_Q = L_{qn}\frac{1}{T}\nabla\mu + L_{qq}\nabla\frac{1}{T} \tag{3.2.17}$$

Where $L_{nq} = L_{qn}$ for the Onsager relations.

When an electric field, $E = -\nabla\psi$ is present and acts on the particles of valency z, the system's energy depends also on the energy generated by it in the volume dV, so that

$$du = Tds + \mu_0 dn + ze\phi dn \tag{3.2.18}$$

The *electrochemical potential* is now defined as

$$\mu \equiv \mu_0 + ze\phi \tag{3.2.19}$$

The electrochemical potential is so composed by a ideal gas term μ_0 and a electrostatic term $ze\phi$, remembering that the ideal gas term is known to be

$$\mu_0(\boldsymbol{r}, t) = k_B T \ln n(\boldsymbol{r}, t) \tag{3.2.20}$$

In order to determine the values of the kinetic coefficients, it must be stated that the flux equations have to be equal to the phenomenological equations derived from the isolated cases. Following this route it is simple to state that the heat flux must follow the Fourier's law $\boldsymbol{J}_Q = -k\nabla T$ in absence of chemical potential differences, so

$$L_{qq} = kT^2\,. \tag{3.2.21}$$

In absence of a temperature gradient and electric fields the particle flux follow the Fick's law of diffusion $\boldsymbol{J}_n = -D\nabla n$ so that, using equation (3.2.20), it is trivial to find

$$L_{nn} = \frac{D}{k_B}n \tag{3.2.22}$$

The direct parts of the matrix are so defined in terms phenomenological equations and experimental parameters.

It can be notice that, in the case of an isothermal system, the particle flux results now

$$\boldsymbol{J}_n = -D\left(\nabla n + \frac{ze}{k_B T}n\nabla\phi\right) \tag{3.2.23}$$

This is the Nernst-Planck equation for static electromagnetic conditions. It is important to state this because the Nernst-Planck equation, coupled with the Poisson equation, regulates the dilute electrolytes behaviour, forming the famous set of *Poisson-Nernst-Plank equations* (PNP).

For the sake of clearness, the complete formulation of this problem can also involve external potentials and convective contribution, modelled usually with an extra term. The general potential U adds a generic term $\boldsymbol{J}_n^{ext} = -(D/k_BT)n\nabla U$, the convective contribution is instead more complicated and can be summarised by $\boldsymbol{J}_n^{conv} = n\boldsymbol{u}$, when u is the fluid velocity and can be calculated with the Navier-Stokes equations. The complete set of equations for mixtures of different species i is so

$$\frac{\partial n_i(\boldsymbol{r},t)}{\partial t} + \nabla \cdot \boldsymbol{J}_{n_i}(\boldsymbol{r},t) = 0 \,, \tag{3.2.24}$$

$$\boldsymbol{J}_{n_i} = -D_i(\nabla n_i + \frac{z_i e}{k_B T} n_i \nabla\phi + \frac{1}{k_B T} n_i \nabla U_i) + n_i \boldsymbol{u} \,, \tag{3.2.25}$$

$$\varepsilon\nabla^2\phi = -Q_{ext} - e\sum_i z_i n_i \,, \tag{3.2.26}$$

$$m\frac{\partial \boldsymbol{u}}{\partial t} + m(\boldsymbol{u}\cdot\nabla)\boldsymbol{u} = -\nabla p + \eta\nabla^2\boldsymbol{u} + \boldsymbol{f} \,, \tag{3.2.27}$$

$$\nabla \cdot \boldsymbol{u} = 0 \,, \tag{3.2.28}$$

where $\boldsymbol{f}$ is an additional body force that may act on fluid elements, m is the mass density of the fluid and η is the viscosity.

The set of equations just mentioned works for constant temperature systems. To understand the physics of an electrolyte in the presence of a temperature gradient it is so necessary to find a phenomenological description of the last kinetic coefficients remained L_{qn} and L_{nq}.

A two species mixtures is taken into account with a solute of density n_1 and a solvent of density n_2, at constant pressure, no convective motion and no viscous dissipation, the entropy production is rewritten as follow

$$\sigma_s = \nabla\frac{1}{T}\cdot\boldsymbol{J}_u - \nabla\frac{\mu_1}{T}\cdot\boldsymbol{J}_{n_1} - \nabla\frac{\mu_2}{T}\cdot\boldsymbol{J}_{n_2} \tag{3.2.29}$$

From the Gibbs-Duhem relation,

$$n_1\nabla\mu_1 + n_2\nabla\mu_2 = 0 \,, \tag{3.2.30}$$

and for the assumption of no convective motion

$$M_1\boldsymbol{J}_{n_1} + M_2\boldsymbol{J}_{n_2} = 0 \,, \tag{3.2.31}$$

where M_1 and M_2 are molecular weights respectively of the solute and the solvent, the entropy production can be rewrote as function of the solute flux

$$\sigma_s = \nabla\frac{1}{T}\cdot\boldsymbol{J}_u - \left(1 + \frac{n_1 M_1}{n_2 M_2}\right)\nabla\frac{\mu_1}{T}\cdot\boldsymbol{J}_{n_1} \tag{3.2.32}$$

In a dilute system the solvent is the dominant specie present so $n_1 << n_2$. Neglecting also the thermal expansions of the solvent leads to the possibility to approximate the thermodynamic affinity of the system again as

$$\chi'_{n_1} = \nabla\frac{\mu_1}{T} \,, \tag{3.2.33}$$

if the entropy production rate σ_s is again rewritten in terms of the heat flux $\boldsymbol{J}_Q$ it returns to be

$$\chi_{n_1} = \frac{1}{T}\nabla\mu_1 \ , \tag{3.2.34}$$

In this way the bi-component system studied is reduced to a mono-component one, giving also the possibility to drop the subscript "1". The flux of the solute is so composed :

$$\boldsymbol{J}_n = -L_{nq}\frac{\nabla T}{T^2} - D\left(\nabla n + \frac{ze}{k_B T}n\nabla\phi\right) \tag{3.2.35}$$

In the same spirit of the Fick's law, which helped define L_{nn} in equation (3.2.22), another phenomenological coefficient can be linked to the non diagonal term of the L_{nq}:

$$D_T = \frac{L_{nq}}{nT^2} \tag{3.2.36}$$

D_T is called *thermophoretic mobility*.
Thus, the solute flow can finally be written as:

$$\boldsymbol{J}_n = -D\left(\nabla n + \frac{ze}{k_B T}n\nabla\phi + \frac{D_T}{D}n\nabla T\right) \tag{3.2.37}$$

The ratio between the thermophoretic mobility D_T and the diffusivity of the solute D is defined as the *Soret coefficinet*:

$$S_T = \frac{D_T}{D} \tag{3.2.38}$$

The Soret coefficient it is a very important quantity in the context of the study of the Seebeck effect in the electrolytes. It can be experimentally measured by applying a temperature difference and analysing the particle densities once the system reached the steady-state. Its unit of measure is $1/K$.

The Soret effect acts on a various range of particles, from gasses to colloids. Its sign is not always positive, it depends on the particle and the solvent considered. The reasons are not completely clear and a physical model that can calculate it is still missing. For the special case of dilute ions in a solvent, a primitive model was however developed by Agar [55].

It deserves a note the possibility to think of the Soret effect as an external potential that acts on the particles, so that eq.(3.2.25) still holds with a potential U which gradient is

$$\nabla U = k_B T S_T \nabla T \tag{3.2.39}$$

Before going in-depth with Agar's model for the Soret coefficient, other general considerations about cross effects in the framework of irreversible thermodynamics should be mentioned.

Taking a more general approach, the equality of the off-diagonal kinetic coefficients $L_{qn} = L_{nq}$ make evident how, for example in (3.2.17), the presence of a chemical potential gradient $\nabla\mu$ between two part of a system, besides creating a particle flux, creates also a heat flux following the kinetic coefficient L_{qn} which can now be written in terms of the thermophoretic mobility D_T. When the chemical potential difference is only due to

the concentration gradient, so only when the ideal part μ_0 of the chemical potential is considered, this effect is called *Dufour effect*.

When instead an electric field is present and the particles are charged, as in the case of eq.(3.2.23), the heat flux generated by the chemical potential gradient is also due to the potential difference. So the heat flow is directly connected to the electric field, this is the *Peltier effect*.

Finally, a charged particle flux can be seen as an electric current where $\boldsymbol{J}_e = -ze\boldsymbol{J}_n$. It is so clear how from this perspective the kinetic coefficient L_{nq} multiplied by ze can link an electric current to a temperature difference. This effect is called *Seebeck effect*.

If to find the phenomenological connection between the heat and the particle flux was sufficient to take the case of no electric field, the correlation between the heat flux and the electric current cannot be found in the same way because the diffusion term is always present, so that the phenomenological coefficients found cannot be put together to return a precise function for the Seebeck coefficient (and so the Peltier coefficient). It will be necessary to solve the overall problem to find the correct solution, in the case of electrolyte, the PNP set of equations will be solved.

Agar's Theory of Soret Coefficient

In order to have a useful quantity to model the Soret effect it is frequent in literature to use the *reduced Soret coefficient* α, defined as

$$\alpha = \frac{TD_T}{2D} \tag{3.2.40}$$

It is usually defined for the advantage to have a dimensionless coefficient and because it takes values of the order of the unity for common ions in an electrolyte. For example the reduced Soret coefficient of KCl in water are $\alpha_K = 0.5$ and $\alpha_{Cl} = 0.1$.

The reduced Soret coefficient, from now on called only Soret coefficient because it is the only one used in this work, is in turn defined from the Eastman's heat of transport Q^*, as

$$\alpha = \frac{Q^*}{2k_BT} \tag{3.2.41}$$

This definition comes from the ideas of Eastman [56]. He understood that in a non-isothermal solution the transport of matter and heat are connected. When a solute particle is transferred between regions at different temperatures a quantity of heat $Q*$ must be absorbed by the particle from the heat reservoir and transported ahead. This concept is a simple statement that comes from the Onsager relations of the cross phenomenological coefficients. Q^* must be identical to the Dufour heat because, if the system must remain isothermal during a particle motion, the energy transported by the particles has to be compensated by equivalent thermal energy. Quoting Agar himself: "Q^* may be regarded as the amount of heat which must be supplied behind or evolved ahead of the diffusing particle in order to keep the temperature constant". Agar tried so to calculate this value from hydrodynamic consideration, starting from the thermodynamic formula founded by Eastman:

$$Q* = -\left(\frac{\partial\mu}{\partial m}\right)_{P,T}\left(\frac{dm}{d\ln T}\right)_{s.s.} \tag{3.2.42}$$

where m is the molality of the solute specie and $s.s.$ denote the steady state. The hydrodynamic theory relies on the idea of analysing a spherical ion motion, which volume includes the solvation shell, in an solvent along the axis x across the plane BB as sketched in figure 3.2.

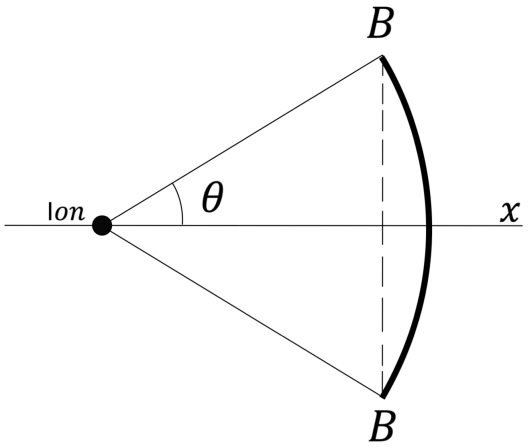

Figure 3.2: Sketch of the ion position along the x axis, considering the plane BB and the angle θ.

The ion moves a constant velocity $\boldsymbol{V}$ under a force $\boldsymbol{F}$. The solvent relative velocity is $\boldsymbol{U}$ so that in stationary state

$$\frac{dS}{dt} = \frac{\partial S}{\partial t} + \boldsymbol{U} \cdot \nabla S = \boldsymbol{U} \cdot \nabla S \tag{3.2.43}$$

The local heat rate evolution q is so

$$-T\frac{dS}{dt} = q = -TU_r\frac{\partial S}{\partial r} \tag{3.2.44}$$

where $\partial S/\partial r$ is the entropy density gradient induced by the ionic motions and U_r is the radial velocity of the solvent with respect to the ion and can be expressed as

$$U_r = U_\infty f(r)\cos\theta \tag{3.2.45}$$

where θ is the angle between $\boldsymbol{V}$ and $\boldsymbol{r}$, $U_\infty = -V$ is the velocity at infinite distance and $f(r)$ determines the solvent velocity field induced by the ionic motion. To determine the entropy gradient the Born theory for the ion-solvent interaction [57] was used, so that

$$S(r) - S(\infty) = \frac{e^2z^2}{8\pi r^4\varepsilon^2}\frac{\partial\varepsilon}{\partial T} \tag{3.2.46}$$

This equation allowed Agar to integrate equation (3.2.44) for θ that goes from $\theta = 0$ to $\theta = \pi$, t that goes from $t = -r/V$ to $t = r/V$ and for r that goes from the ion radius R_i to infinite. These integrations lead to

$$Q^* = -\frac{T}{bR_i}\frac{e^2z^2}{\varepsilon^2}\frac{\partial\varepsilon}{\partial T} \tag{3.2.47}$$

where b is 3 for stick hydrodynamic boundary condition and 4 for slip boundary condition.

This demonstration shows the limits of this approach. The Born model is a simplification of the physics of the system, it is only valid for an isolated ion and it does not consider the collective interactions in a finite concentration solution. This model is just a way to understand what is the most important factor for the heat of transport, so the dielectric constant, without the aim of calculating the values precisely. It also gives the right order of magnitude for simple ions in aqueous solvent, as it's possible to see in the table below, but it is completely out of scale for more complicated electrolytes such as the polymeric electrolyte used in the experiments cited.

Ion	Q^* theoretical	Q^* experimental	Reference
K^+	$2.131 \cdot 10^{-21}$	$4.11 \cdot 10^{-21}$	[58]
Na^+	$2.893 \cdot 10^{-21}$	$4.98 \cdot 10^{-21}$	[34]
Cl^-	$1.566 \cdot 10^{-21}$	$0.823 \cdot 10^{-21}$	[58]

To overcome this limitation some computational approaches were developed, for example, the work of Di Lecce [59] permitted to calculate the Soret coefficient of a 0.5 M solution of $LiCl$, varying the temperature and the concentration.

The explanation for the value of the Eastman heat of transport, ergo for the Soret coefficient, is not essential to the aim of this work, but it shows the amount of work that is still necessary to understand deeply the behaviour of electrolyte subjected to a temperature gradient. It is also explained why the simulations, made with the theoretical framework now available in literature, cannot match the experimental values, but they can only understand the behaviour of the system. It seems however promising the possibility to overcome these theoretical limits to predict the values of the coefficients and so to optimize solvents and solutes.

Planar Electrochemical Capacitor Under Temperature Gradient

Henceforward it will be discussed the Thesis Work done. The following model was developed aiming to understand the behaviour of a supercapacitor subjected to a temperature gradient .

The experiment cited in Chapter 2 is taken as reference and an equivalent water-based system was modelled and simulated focusing on the internal behaviour of the system. This overcomes the limits of the experimental procedure that can only base the information on the parameters obtained measuring the system from an external point of view.

The experiment, as explained, was divided into four phases. The same approach was taken in this work, in which the phases behaviours are first analytically calculated, then simulated, and finally modelled with an equivalent circuit. The main difference between the experiment and the model here explained, besides the electrolyte, is the choice not to pose any resistance in the external circuit. If the experiment needed it to measure a voltage difference between the electrode once the circuit was closed, the simulation permits to "observe" the system in short circuit even without the load, this also permits to understand the pure internal dynamics that can then be coupled with an external load when necessary.

In order to fully understand what happens in a thermally rechargeable supercapacitor, it is first necessary to start solving the PNP equations in a simpler case: a planar electrochemical capacitor subjected to a temperature gradient.

The solution adopted was developed originally by Stout and Khair [58] that linearised the PNP equations for a dilute electrolyte in a small temperature gradient in order to calculate the dynamics of the potential and the charge density. That solution can be perfectly applied to a planar electrochemical capacitor during phase i in open circuit. Using that method, it is then possible to analytically solve the distribution of charges and potentials in the other phases of the recharge cycle.

4.1 Analytical Results

Considering an electrolytic cell (figure 4.1) with the two parallel flat electrodes positioned at $x = \pm L$, with L much larger than their separation, the edge effects can be neglected and the system can be solved as one-dimensional. The convection effect is ignored due to the L being sufficiently small to avoid these phenomena. A system composed of monovalent

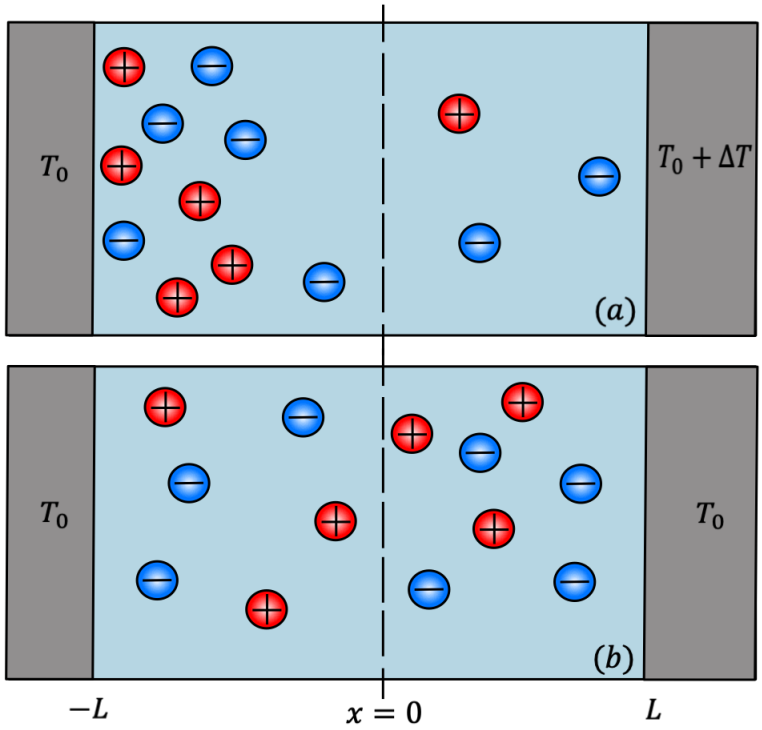

Figure 4.1: Sketch of a planar electrochemical capacitor: visualization of the intuitive difference between heated condition (a) and initial state (b).

ions, which data are based on the values of KCl in an aqueous solute. The solute has a dielectric permittivity $\varepsilon = \varepsilon_0 \cdot \varepsilon_r$, a density η and a specific thermal capacitance c_p. The cations and the anions have a Soret coefficient α_+ and α_- respectively and a diffusion coefficient $D_+ = D_- = D$. The electrostatic potential $\phi(x,t)$, the ionic number densities $n_\pm(x,t)$, the ionic particle fluxes $j_\pm$ and the local temperature $T(x,t)$ are studied with the following equations:

$$\frac{\partial n_\pm(x,t)}{\partial t} = -\frac{\partial j_\pm(x,t)}{\partial x} \tag{4.1.1}$$

$$j_\pm(x,t) = -D\left(\frac{\partial n_\pm}{\partial x} \pm \frac{e}{k_B T} n_\pm \frac{\partial \phi}{\partial x} + \frac{2\alpha_\pm n_\pm}{T}\frac{\partial T}{\partial x}\right) \tag{4.1.2}$$

$$-\frac{\partial}{\partial x}\left(\varepsilon \frac{\partial \phi(x,t)}{\partial x}\right) = e(n_+ - n_-) \tag{4.1.3}$$

$$\frac{\partial}{\partial t}\left(\eta c_p T(x,t)\right) = \frac{\partial}{\partial x}\left(k\frac{\partial T(x,t)}{\partial x}\right) - e(j_+ - j_-)\frac{\partial \phi(x,t)}{\partial x} \tag{4.1.4}$$

The continuity equation (4.1.1), the Nernst-Plank equation (4.1.2) and the Poisson equation (4.1.3) are used as stated, instead the heat equation (4.1.4) contains a heat source term that is discussed in in the works of Janssen and Co [60] [61] . This contribution will

be neglected in the present work because it can be demonstrated to be a second-order term which only complicates calculus without adding more precision. Moreover, these equations are valid in the linear dilute regime used to create them, as exposed in the introduction. From that type of approximation, another consideration must be made: the Debye length is much smaller than the length of the system ($\kappa L >> 1$) and the electric double layers are fully developed (thin diffuse layer condition). This holds for the geometries used in this work and has some implication on the results that will be exposed later.

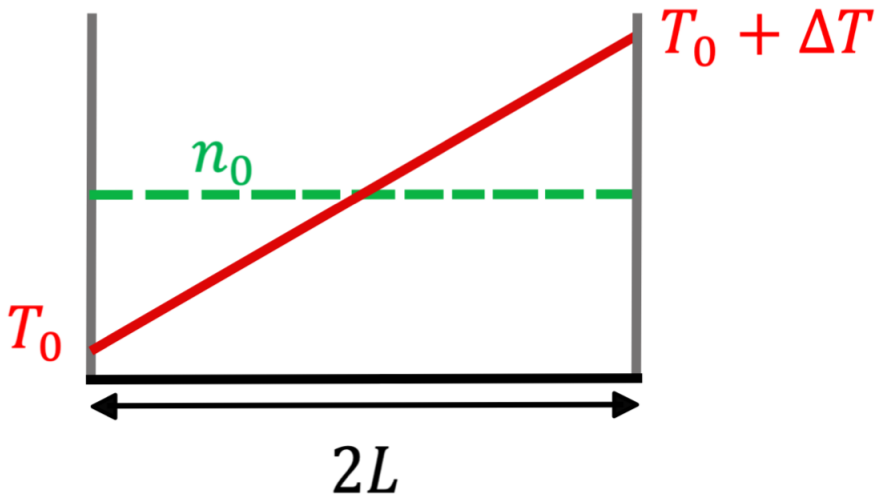

Figure 4.2: Sketch of planar electrodes electrochemical capacitor. The green line represent the initial ion concentration n_0, the red line represent the temperature gradient established inside the cell after the beginning of the cycle. The dimension of the cell is $2L$ with the origin $x = 0$ is posed in the center.

The initial conditions consider impermeable and inert boundaries, no surface charge or potential applied, a charge neutral electrolyte with equal ions densities n_0 and constant initial ambient temperature T_0:

$$T(x, t < 0) = T_0$$
$$n_{\pm}(x, t < 0) = n_0$$
$$j_{\pm}(x = \pm L, t) = 0$$

As done by Putnam and Cahill [62], as first approximation ,for a binary electrolyte in small temperature gradient, it is possible to consider that

$$\frac{\partial n_+}{\partial x}\frac{1}{n_+} \simeq \frac{\partial n_-}{\partial x}\frac{1}{n_-}$$

the physical reason is that the Soret effect acts on both the ion species, creating similar density profiles and the need for local charge neutrality maintains the ions densities coupled.

By subtracting the single ion particle flux of the positive ions from the one of the negative ions, it is possible to relate a potential difference between tow points of the electrolyte ΔV and the temperature difference between the same points ΔT:

$$\Delta V = -\frac{(\alpha_+ - \alpha_-)k_B}{e}\Delta T \tag{4.1.5}$$

The Seebeck coefficient (S_e) for a binary mixture can so be estimated to be

$$S_e = \frac{(\alpha_+ - \alpha_-)}{e}k_B \tag{4.1.6}$$

From now on the Seebeck coefficient will be defined in this way, even if the overall electric potential generated by the system may vary from the former approximated result.

To be more precise, it is necessary to solve the complete set of equations, considering the time and space dependence of the temperature and densities distributions. Being the temperature an important part of the physics it is necessary to do some clarifications. The temperature on the right side (in $+L$) will be modelled as brought instantly from T_0 to $T_0 + \Delta T$, not considering the thermal flux and the time necessary to heat the electrode itself.

To reach an analytical time-dependent solution of the previous equation another strong assumption is made: the time constant for the build-up of the temperature gradient inside the electrolyte is much smaller than the diffusion time. This approximation is usually valid in an electrolyte due to the heat diffusivity being much greater than the ion diffusion coefficient: $k/\eta c_p >> D$. $T(x,t)$ becomes now a time-independent linear equation:

$$T(x,t) = T_0 + \frac{\Delta T}{2L}(x + L) \tag{4.1.7}$$

that it is instantly applied to the system when the thermodynamic cycle starts. In order to have a clearer picture, the time constants of the heat equation and of the PNP equations will be compared in the next sections. It is so important to cite Jannsen's temperature timescale constant [63]:

$$\tau_T = \frac{4L^2\eta c_p}{\pi^2 k}\ , \tag{4.1.8}$$

to have a reference time to compare.

Successively, assuming a weak temperature gradient, in particular assuming $\Delta T/T_0 << 1$, it is possible to linearise the equations and consider ε, k, η ,c_p, $\alpha_\pm$ and D as temperate independent, and consequently space and time independent. For convenience the potential can be restated in its dimensionless form $\psi = e\phi/k_B T_0$.

The linearisation permits to consider the ion densities as composed by the initial value plus a perturbation term $n_\pm(x,t) = n_0 + \delta n_\pm(x,t)$, so that, it is possible to neglect second order terms as $\delta n_\pm \cdot \Delta T/(T_0 2L)$ and $\delta n_\pm \cdot \partial\psi/\partial x$.

The flux equation can now be written a linear equation:

$$j_\pm = -D\left(\frac{\partial \delta n_\pm}{\partial x} \pm n_0\frac{\partial \psi}{\partial x} + \frac{\alpha_\pm n_0}{T_0}\frac{\Delta T}{L}\right) \tag{4.1.9}$$

Rephrasing the problem with dimensionless variables:

$$\rho = \frac{n_+ - n_-}{2n_0} = \frac{\delta n_+ - \delta n_-}{2n_0}\ , \tag{4.1.10}$$

$$c_{abs} = \frac{n_+ + n_-}{2n_0} = \frac{\delta n_+ + \delta n_- + 2n_0}{2n_0} = \frac{\delta n_+ + \delta n_-}{2n_0} + 1\,, \tag{4.1.11}$$

where ρ is the dimensionless charge density and c_{abs} is the dimensionless absolute neutral density. It is also convenient to call c the dimensionless difference of the neutral density with respect to the bulk initial state

$$c = \frac{\delta n_+ + \delta n_-}{2n_0} = c_{abs} - 1 \tag{4.1.12}$$

A new set of equations is so obtained:

$$\frac{\partial c}{\partial t} = D\frac{\partial^2 c}{\partial x^2} \tag{4.1.13}$$

$$\frac{\partial \rho}{\partial t} = D\frac{\partial^2 \rho}{\partial x^2} - D\kappa^2\rho \tag{4.1.14}$$

$$\frac{\partial^2 \psi}{\partial x^2} = -\kappa^2\rho \tag{4.1.15}$$

defining $\kappa = 1/\lambda_D$, where $\lambda_D = \sqrt{(\varepsilon k_B T)/(2e^2 n_0)}$ is the Debye Length. The impermeable electrode conditions are consequently rephrased as

$$\left.\frac{\partial \rho}{\partial x}\right|_{x=\pm L} = -\left.\frac{\partial \psi}{\partial x}\right|_{x=\pm L} - \frac{\alpha_d}{L}\frac{\Delta T}{T_0} \tag{4.1.16}$$

$$\left.\frac{\partial c}{\partial x}\right|_{x=\pm L} = -\frac{\alpha_m}{L}\frac{\Delta T}{T_0} \tag{4.1.17}$$

where $\alpha_m = (\alpha_+ + \alpha_-)/2$ and $\alpha_d = (\alpha_+ - \alpha_-)/2$.

The Soret coefficients are now present only in the boundary conditions, and the derivative of the charge density ρ is different from 0 at the electrodes, even in case the surface is 0 (ergo $\partial\psi/\partial x = 0$). This implies that the system will have a charge density at the boundaries even with the absence of a surface charge in the electrode material.

In order to calculate the variables during the phases of the recharge cycle, it is now sufficient to select the right boundary conditions.

Phase i

As exposed in the work of Stout and Khair in case of no surface charge, ergo open circuit condition the B.C.s become:

$$\left.\frac{\partial c}{\partial x}\right|_{x=\pm L} = -\frac{\alpha_m}{L}\frac{\Delta T}{T_0} \tag{4.1.18}$$

$$\left.\frac{\partial \rho}{\partial x}\right|_{x=\pm L} = -\frac{\alpha_d}{L}\frac{\Delta T}{T_0} \tag{4.1.19}$$

$$T(x, t \geq 0) = T_0 + \frac{\Delta T}{2L}(x + L) \tag{4.1.20}$$

$$\psi(L) = 0 \tag{4.1.21}$$

when the right electrode in L is grounded and the temperature is imposed instantly.

The solutions for phase i are reported considering the space dependent behaviour after the transient and the time dependent behaviour in the left electrode in -L:

$$c_i(x) = -\alpha_m \frac{\Delta T}{T_0} \frac{x}{L} \tag{4.1.22}$$

$$c_i(-L,t) = \alpha_m \frac{\Delta T}{T_0}(1 - e^{-t/\tau_c}) \tag{4.1.23}$$

$$\rho_i(x) = -\frac{\alpha_d \Delta T}{\kappa L T_0} \frac{\sinh \kappa x}{\cosh \kappa L} \tag{4.1.24}$$

$$\rho_i(-L,t) = \frac{\alpha_d \Delta T \tanh(\kappa L)}{T_0 \kappa L}(1 - e^{t/\tau_\rho}) \tag{4.1.25}$$

$$\psi_i(x) = -\frac{\alpha_d \Delta T}{L T_0}\left(\frac{\sinh \kappa L}{\kappa \cosh \kappa L} - \frac{\sinh \kappa x}{\kappa \cosh \kappa L} - L + x\right) \tag{4.1.26}$$

$$\psi_i(-L,t) = -\frac{2\alpha_d \Delta T}{T_0}\left(1 - \frac{\tanh \kappa L}{\kappa L}\right)(1 - e^{-t/\tau_\psi}) \tag{4.1.27}$$

The neutral density, which solution is a simple linear plot proportional to $\alpha_m \Delta T/T_0$, is poorly affected by the temperature gradient applied, being $\Delta T << T_0$. This permits the validation of the approximation made to find equation (4.1.5).

The charge density follows a "sinh profile" with characteristic length $1/\kappa = \lambda_D$, the value in the left electrode (in $-L$) is proportional to $\alpha_d \Delta T/T_0$ divided by $1/\kappa L$, which, for hypothesis, is much bigger than 1. This means that the charge density at the boundary is different from 0, but it is very low due to the physical repulsion between same-sign ions not balanced by a surface charge.

Rewriting the potential to calculate the absolute potential difference between the electrodes as $\Delta V = -\frac{(\alpha_+ - \alpha_-)k_B}{e}\Delta T\left(1 - \frac{tanh(\kappa L)}{\kappa L}\right)$, it is possible to see how the Seebeck coefficient defined in equation (4.1.5) is confirmed, due to the possibility to approximate $\tanh(\kappa L)/\kappa L$ as 0. We can now be sure to define the Seebeck coefficient $S_e = (\alpha_+ - \alpha_-)k_B/e$ as a constant of the system.

The characteristic times were also found in literature:

$$\tau_c = \frac{L^2}{3D} \tag{4.1.28}$$

$$\tau_\rho = \frac{1}{2D\kappa^2}\left(1 - \frac{2\kappa L}{\sinh 2\kappa L}\right) \tag{4.1.29}$$

$$\tau_\psi = \frac{1}{2D\kappa^2}\frac{3\tanh\kappa L + \kappa L(\tanh^2\kappa L - 3)}{\tanh\kappa L - \kappa L} \tag{4.1.30}$$

The time constants make clear how the dynamics of the neutral charge is a pure diffusion dynamics, instead the potential and charge density dynamics are less trivial. They depend on the square of the Debye length, in particular considering that $\kappa L >> 1$, $\tau_\rho \sim \lambda_D^2/2D$ and $\tau_\psi \sim \lambda_D^2/D$.

This condition is usually satisfied in a microscopical electrochemical capacitor in which the Debye length is of the order of the nanometres and the thickness of the device is of micrometers or millimetres. These time constants imply that the times required to obtain a potential difference from the Seebeck effect in an electrolyte is much shorter than the diffusion time leading to an optimal condition for the use of this technology in various field, among which the production of electrical energy.

Must be also stated that the time constants were found considering a late-time approximation and neglecting the temperature gradient dynamics, in particular, the Laplace transform of the solution was expanded for $s \sim 0$. This leads to a good approximation for the time required to reach the steady-state once the temperature profile is stable, leaving some uncertainty in the initial phase of the transient.

Regarding this issue the work of Jannsen and Bier [63] analysed the short term dynamics more precisely and the temperature timescales, but this level of precision goes beyond the scope of this work, where it is sufficient to consider the order magnitude of the time constants found.

Pase ii

Considering now a new configuration in which the electrodes are connected in short circuit and the temperature gradient is still active, it is necessary to apply new boundary conditions. The surface charge is now present so the equation (4.1.16) hold, but the potential is 0 in both sides: $\psi(\pm L, t) = 0$. This leads to new solutions, in which the neutral charge is unaffected, not being dependent on the electrical configuration of the system, but the potential and the charge density are modified. Starting analysing the steady state, the solutions are:

$$c_i(x) = c_{ii}(x) = -\alpha_m\frac{\Delta T}{T_0}\frac{x}{L} \tag{4.1.31}$$

$$\rho_{ii}(x) = -\frac{\alpha_d\Delta T}{T_0}\frac{\sinh\kappa x}{\sinh\kappa L} \tag{4.1.32}$$

$$\psi_{ii}(x) = \frac{\alpha_d\Delta T}{T_0}\left(\frac{\sinh\kappa x}{\sinh\kappa L} - \frac{x}{L}\right) \tag{4.1.33}$$

The solution for the neutral density difference is unchanged. The charge density and the potential are instead modified from the new boundary conditions. The charge density is still proportional to $\alpha_d\Delta T/T_0$, but it is now present at the denominator only a $\sinh\kappa L$ term. This means that at $-L$ the charge density will be

$$\rho_{ii}(-L) = \frac{\alpha_d\Delta T}{T_0} \tag{4.1.34}$$

which is κL times greater than the one of the phase i solution. In the case of thin double layer, this difference is of some order of magnitude. The physical interpretation of this difference is that the presence of a surface charge permits the ions to approach closer the electrode, being attracted by the opposite charges. The potential function is a combination of a sinh term and a linear trend which are physically related to the electrostatic field and the thermal effects respectively.

It is now possible to find the surface charge that is collected, and so stored, in the supercapacitor:

$$\sigma_{ii}(\pm L) = \pm\varepsilon\frac{S_e\Delta T}{2}\left(\frac{\kappa\cosh\kappa L}{\sinh\kappa L} - \frac{1}{L}\right) \tag{4.1.35}$$

Considering the potential difference close to the electrode $\Delta V_{local} = S_e\Delta T/2$, already thinking about the EDL created as a capacitor in a two capacitor system powered by $S_e\Delta V$, the specific capacitance $C = \partial\sigma_s/\partial\Delta V_{loacal}$, in thin diffusion layer condition, is

$$C = \varepsilon\left(\frac{1}{\lambda_D} - \frac{1}{L}\right) \tag{4.1.36}$$

Neglecting the $1/L$ term the capacitance coincides with the specific capacitance of a double layer in a normal electrolyte system with an imposed potential. This demonstrates the experimental results, that observe how the behaviour of a thermally recharged electrochemical capacitor is the same as the one of a capacitor charged externally imposing the same potential $\Delta V = S_e\Delta T$.

It is interesting to notice how both the charge density and the surface charge are not dependent on the temperature gradient $\Delta T/2L$ but only on the absolute temperature difference between the extremes. This means that it is not important the length of the system in order to obtain the maximum charge stored. Unfortunately, the Laplace transform of equations (4.1.13)-(4.1.15) can be solved, but not anti-transformed, this implies that the dynamic behaviour of the phase ii must be found in other ways.

Phase iii

Once the capacitor is charged, it is sufficient to open the circuit so that, when the temperature gradient is removed, the surface charge is maintained, and the capacitor is ready to be used to power an external device. The ion densities distribution respond now as a simple Gouy-Chapman solution for a double layer with an imposed surface charge equal to the one found in the phase ii solution. The temperature profile is now flat $T(x) = T_0$ and the neutral density has of course a flat solution in absence of a temperature gradient.

Regarding the charge density and the potential, the cited boundary conditions lead to the following solutions:

$$\rho_{iii}(x) = -\frac{\alpha_d\Delta T}{T_0}\left(\frac{1}{\sinh\kappa L} - \frac{1}{\kappa L\cosh\kappa L}\right)\sinh\kappa x \tag{4.1.37}$$

$$\psi_{iii}(x) = \frac{\alpha_d\Delta T}{T_0}\left(\frac{\kappa L - \tanh\kappa L}{\kappa L\sinh\kappa L}\right)(\sinh\kappa x - \sinh\kappa L) \tag{4.1.38}$$

Can be also noticed how $\psi_i(-L)$ of the charged capacitor is equal in modulus and opposite in sign of the $\psi_{iii}(-L)$ of phase i. This trivial result further confirms how the mechanism of charging is comparable to an external potential of value ΔV, despite the very different potential profile for the phase i potential.

Considering the dynamics, we can affirm that the double layer is already formed so it does not affect the time behaviour, instead, the charge density and the neutral density should change following the time scale found in the phase i solution.

4.2 Numerical Results

In order to confirm the analytical results, it is necessary to solve the equations numerically. In particular, Comsol Multiphysics® was used. It is a finite element method (FEM) dynamic multiphysics simulation program. The FEM guarantees optimal results once the mesh and the time stepping is correctly set: the mesh was chosen to be of ~ 3000 domains taking care of positioning a higher number of elements near the boundaries so that the EDL can be better calculated. The dynamic solution was obtained using a backward differentiation formula method of order 5. Some issued occurred due to computational and program limits: it was not possible to store and plot a high number of time steps, due to the limit of the computer (low RAM), and the program is not optimized for different steps simulations in which the boundary conditions charges multiple times. These limits were overcome by balancing mesh and time-stepping, and simulating one step at a time.

The solution was carried out for a specific set of parameter in order to obtain results which are comparable with the approximation made in the analytic formulation and permits a clear view of the solution. In particular, the length of the cell was chosen in a way that the EDL can be seen but there is no risk of overlapping: $\kappa L = 100$. The other parameters were chosen to represent an KCl solution of 1 mol/m^3: $T_0 = 298.15\,K$, $\Delta T = 0.3\,K$, $z_+ = -z_- = 1$ (from ref. [58]). Particular attention was given to the choice of the temperature-dependent properties of the solution: the diffusion coefficient, the Soret coefficient, the thermal conductivity and the dielectric constant are dependent on both temperature and, especially for the dielectric constant, ion concentration. Some simulations were made using this dependence but the results were identical (within the numerical error margin) to the ones made with constant properties. The only sensible difference was in the case of concentration-dependent dielectric constant, but only in the case of high concentration ($1000\,mol/m^3$) and high temperature differences ($80\,K$).Instead, for the previous data the concentration shift, due to the temperature gradient, was not sufficient to obtain a change in the results. The parameter were so posed constant of values: $\alpha_+ = 0.5$, $\alpha_- = 0.1$ [64] , $D_+ = D_- = 10^{-9} m^2/s$ [65] , $\varepsilon_r = 78.5$, $k = 0.6\,W/(m \cdot K)$, $\eta_{H_2O} = 1000\,kg/m^3$, $c_p = 4186\,J/(Kg \cdot K)$. Where ε_r is the relative permittivity, k the thermal conductivity, η_{H_2O} the density of the electrolyte and c_p the specific heat of water. With the previous values the Debye length results to be $\lambda_D = 9.62nm$.

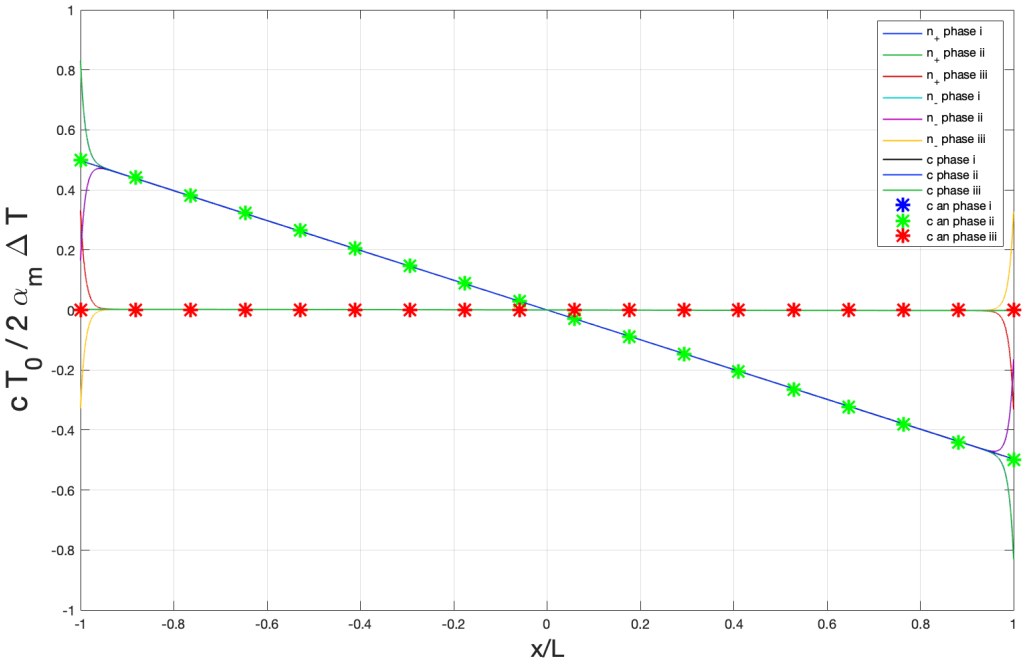

Figure 4.3: Numerical solution (solid lines) and analytical solution (symbols) of the dimensionless neutral density difference $cT_0/2\alpha_m\Delta T$ vs the dimensionless length x/L, the single decoupled positive and negative ions density profiles are also plotted.

The solution for the neutral density, as represented in figure 4.3, is a trivial linear profile. The slope is directly proportional to the temperature difference and the Soret coefficients. Physically this variable can be easily described as a neutral set of particles pushed by the Soret force against the impenetrable electrode. The absence of electromagnetic effects on this variable guarantees the same solution for phase i and ii, in phase iii c returns to the flat profile initial condition ($c(x) = 0$). It is also possible to analyse the behaviour of the single positive and negative species noticing how they follow a linear trend up to the electrode in which, separating due to the electric forces, give origin to the charge density profile.

More interesting is the behaviour of the charge density in figure 4.4. During phase i the charge density near the electrode is different from 0, even in case of no surface charge in the electrode, as visible in the zoom of the phase i solution in figure 4.4. The reason is that the Soret coefficient for the positive ion is greater than the one of the negative ones permitting a charge unbalance to be sustained in steady-state. The ρ function goes to 0 in some Debye length as confirming that the characteristic length in which the charge density can be different from 0 is the Debye length even in the case of a temperature gradient. The absolute value of this charge density is much lower than its value in phases ii and iii because the absence of a counter charge on the surface does not allow the positive ions to get closer to the electrode due to the electrostatic repulsion.

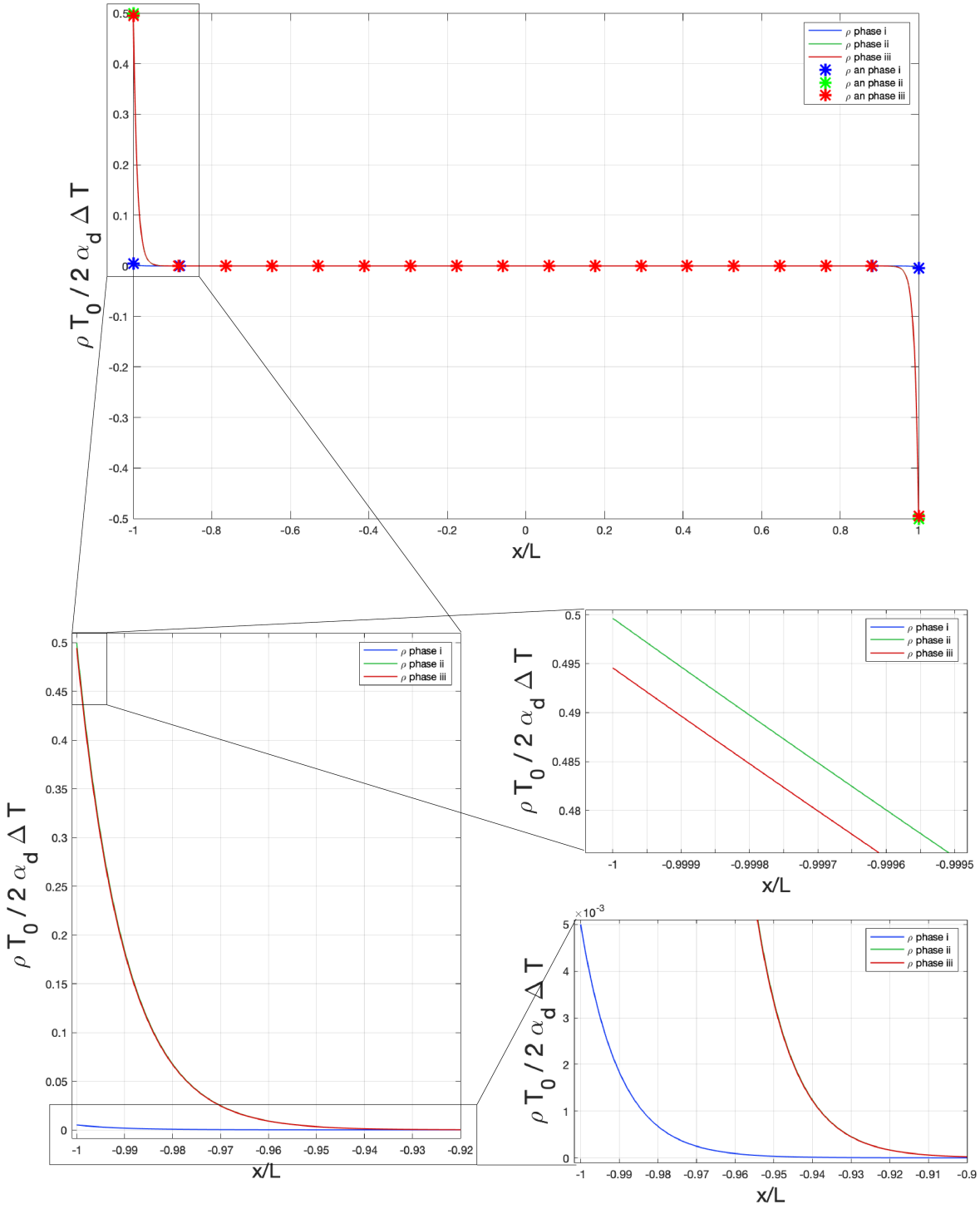

Figure 4.4: Numerical solution (solid lines) and analytical solution (symbols) of the dimensionless surface charge $\rho T_0/2\alpha_d\Delta T$ vs the dimensionless length x/L in the three phases of the cycle: phase i blue, phase ii green, phase iii red. Differences between phase i, phase ii and phase iii are represented in the zoom schemes.

The phase ii solution for the charge density is instead similar to a more classical solution for an EDL of an electrolyte in contact with a charged electrode, because in this phase the electrons can flow in the circuit and the electrode can be charged.

Remembering that in phase ii, the temperature gradient is still applied, it is not so trivial to state that the shape of the ρ function near the electrodes is the same of the classical Guoy-Chapman one.

This effect is due to the high κL chosen and to the low ΔT present. A lot of interesting theoretical work could be done indeed on temperature gradients inside the EDL, especially for high ion concentrations. For the aim of this thesis, it is not necessary to go further than state the presence of the $\sinh \kappa L$ in the denominator of the analytical solution that shows a difference with respect to the usual $\cosh \kappa L$. This difference is, as previously stated, negligible for a thin EDL.

As it is possible to see in the zoom of figure 4.4, there is a difference between the phase ii and phase iii solution. This difference can be analytically calculated to be

$$\rho_{ii}(-L) - \rho_{iii}(-L) = \frac{\alpha_d \Delta T}{T_0} \frac{\tanh \kappa L}{\kappa L} = \rho_i(-L) \, ,$$

that is exactly the value of the charge density in on the electrode during phase i. This can be physically explained as a superposition of the electrostatic effect and the Soret effect that acts on the charge density. This is confirmed thinking that the surface charge of phase ii and iii is the same and the only difference is due to the temperature gradient that creates the Soret effect.

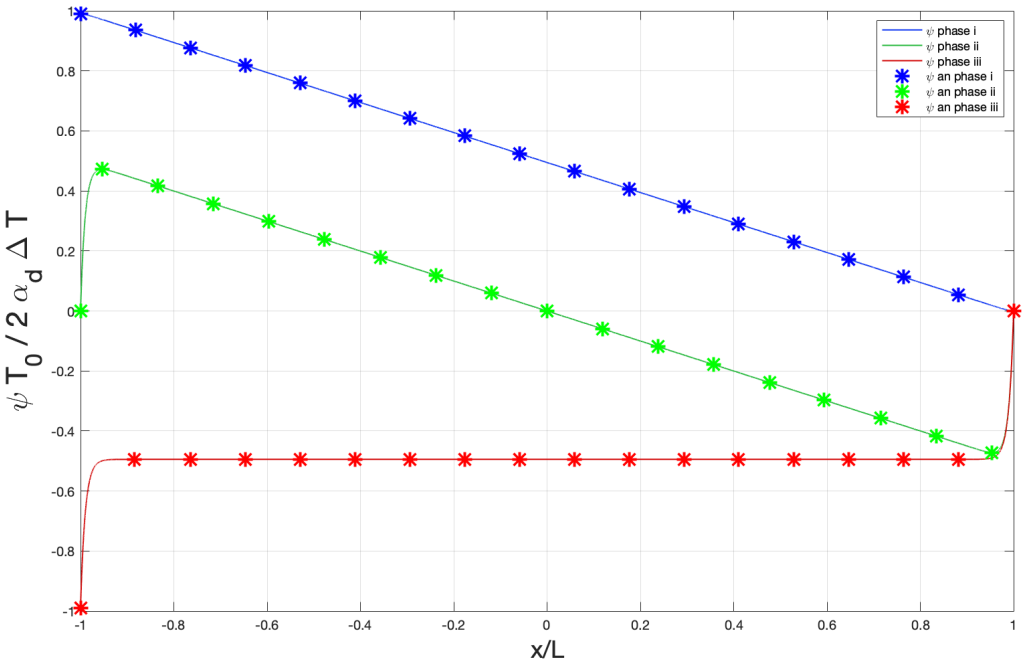

Figure 4.5: Numerical solutions (solid lines) and analytical solutions (symbols) of the dimensionless potential $\psi T_0/2\alpha_d \Delta T$ vs the dimensionless length x/L, in the three phases of the cycle: phase i blue, phase ii green, phase iii red.

The dimensionless potential ψ plotted in figure 4.5 shows the particular behaviour that is obtained in the presence of a temperature gradient. To be clearer is necessary to note that $\psi T_0/2\alpha_d\Delta T = V/S_e\Delta T$ so that it is obvious to check that $S_e\Delta T$ can be used as the maximum potential for the system.

The phase i solution is strongly different from a usual potential shape in an electrolyte. The profile is almost perfectly straight, apart from the zone near the electrodes in which it must become flat to accommodate the 0 surface charge condition. This particular potential shape is due to the necessity of the system to equilibrate itself in order to compensate for the charge unbalance created.

The phase ii potential behaviour is particular too. Near the electrodes, it is an almost perfect EDL solution, apart from the fact that the EDL appears to be not completely developed because its peak is not at $S_e\Delta T/2$. This is due to the presence of the Seebeck potential that, being proportional to $-x/L$, deflects the curve before the complete development of the exponential part.

The phase iii it is instead a usual Gouy-Chapman solution for a double EDL system with imposed surface charge. The superposition of the effect is clearly visible in the potential shape too, the phase ii solution is analytically equivalent to $\psi_{ii}(x) = \psi_i(x) + \psi_{iii}(x)$, as in the the case of the charge density.

The numerical results confirm perfectly the analytical approximation made and assure the possibility to treat the system as a sum of Soret-driven and electrostatic driven effects. The superposition of effects found is fundamental in order to simplify the equations in a more complex system in which, as we will soon see, the electrodes can be multiples.

4.3 Equivalent Electrical Circuit

A well-established method to analyse an electrode-electrolyte system consists of comparing the latter to an equivalent electrical circuit (EEC). Regarding a simple electrochemical capacitor it is sufficient to represent the electrode-EDL interaction on either side, with a capacitor of specific capacitance C, the value of which depends on the Debye length. The electrolyte in between becomes a resistance that accounts for the conductivity of the electrolyte and the distance between the electrodes.

The value of the capacitance per unit area can be simply considered $C = \varepsilon/\lambda_D$ as usually done in a dilute electrochemical system, this approximation was previously demonstrated to be valid in the thermal charging case too, so it will be used in this work.

The value of the resistance can be calculated starting from the Nernst-Plank equations. The specific electrical current J_{el} is proportional to the difference between the flux of positive and negative ions,

$$J_{el} = e(j_+ - j-) \tag{4.3.1}$$

Considering now the potential and the temperature functions as linear profiles the derivatives can be approximated as follow: $\partial\phi/\partial x \simeq \Delta\phi/d$ and $\partial T/\partial x \simeq \Delta T/d$ where d is the distance in which the gradient is calculated.

This consideration allows us to write the specific electrical current in terms of the electrolyte parameters:

$$J_{el} = -\frac{2\sigma_{el}}{d}(\Delta\phi + S_e\Delta T) \tag{4.3.2}$$

where $\sigma_{el} = (De^2n_0)/(k_BT_0)$ is the electrical conductivity of the electrolyte and the overall resistance per unit area of the electrolyte is confirmed to be

$$R = \frac{d}{2\sigma_{el}} \tag{4.3.3}$$

as in the usual electrolyte system.

The particularity regarding this system is that the potential is not applied by an external source, but it can be modelled as an internal voltage generator of value $\Phi_0 = S_e\Delta T$ positioned in the lower connector, ergo in the electrolyte.

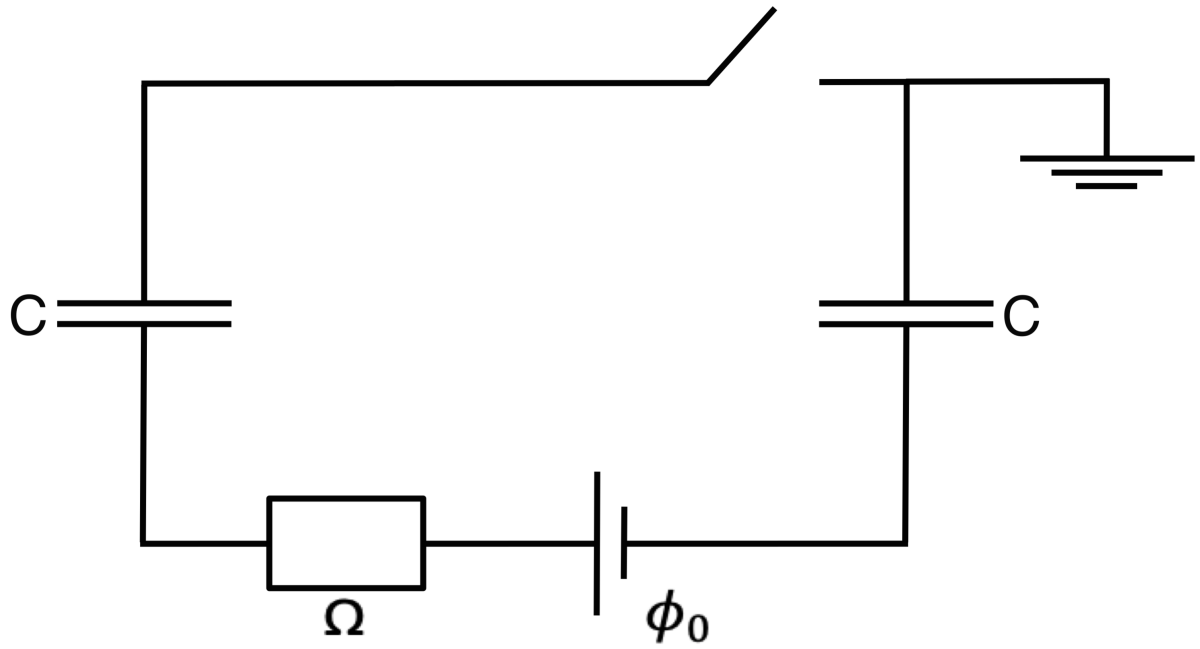

Figure 4.6: Equivalent electrical circuit for a planar electrode capacitor subjected to a temperature gradient.

Applying the previous formulas to the geometry of this device, Ω, the resistance of the electrolyte reservoir, is $\Omega = L/\sigma_{el}$. ΩC, the time constant of the system, is equal to $2L/\kappa D$.

The electrical circuit can be solved in the various phases of the cycle, giving the possibility to obtain rapidly the behaviour of the thermally charged capacitor with simple algebraic equations. ΔV is defined as the potential experimentally measured connecting the 2 electrodes of the electrochemical capacitor to a voltameter, it is so possible to rapidly calculate ΔV considering the difference between the upper part of the fictitious capacitors, ergo the part representing the electrodes. To distinguish the analytical results for the surface charge from the EEC ones the charge per unit area accumulated in the electrodes will be referred as Q instead of σ and the absolute value of voltage over the capacitors is $\Delta\Psi$ so that $Q = C\Delta\Psi$.

4.3.1 EEC Solutions

The phase i circuit configuration is composed of the switch positioned on "open" and the voltage generator on. In open circuit no current is flowing so the capacitor will not be charged. This prevents the EEC to be useful in the study of the phase i dynamics, but it predicts efficiently the steady-state:

$$Q = C\Delta\Psi = 0 \longrightarrow \Delta\Psi = 0 \tag{4.3.4}$$

$$\Delta V = \Phi_0 = S_e \Delta T \tag{4.3.5}$$

The interesting part of this representation is mostly in the phase ii dynamic solution: the current can now flow because the circuit is closed and the solution can be achieved using Ohm's law.

$$\Phi_0 - \Omega I - 2\Delta\Psi = 0 \tag{4.3.6}$$

$$\frac{dQ}{dt} = I = C\frac{d\Delta\Psi}{dt} \tag{4.3.7}$$

$$\Delta\dot{\Psi} = \frac{\Phi_0 - 2\Delta\Psi}{\Omega C} \tag{4.3.8}$$

This ordinary differential equation is readily solved,

$$\Delta\Psi = \frac{\Phi_0}{2}(1 - e^{\frac{2t}{\Omega C}}) \tag{4.3.9}$$

It is so possible to calculate the charge stored at the end of the transient as $Q = C\Phi_0/2$. For clearness here rewritten in explicit form:

$$Q = -\frac{\varepsilon}{\lambda_D}\frac{S_e\Delta T}{2}(1 - e^{-\frac{tD}{L\lambda_D}}) \tag{4.3.10}$$

This equation, in thin double layer condition, coincides with the equation 4.1.35, confirming the possibility to use the equivalent electrical circuit.

The characteristic time of the system is therefore

$$\tau_{RC} = \frac{\Omega C}{2} = \frac{L\lambda_D}{D} \tag{4.3.11}$$

that, from now on, will be the reference time that will be compared to the others in the nano-structured electrode cases. After the transient, the voltage measured ΔV will be 0 and its time behaviour will coincide with the one of $\Delta\Psi$.

The phase iii starts when the switch is again open and the internal voltage generator is removed, corresponding to the temperature gradient removal. In open circuit the charge accumulated in the capacitors remains stored, it is therefore equivalent to the charge of the previous phase Q. The potential measured ΔV will be calculated as the sum of the two potentials drops, resulting in $\Delta V = -S_e\Delta T$, as expected from the simulations. Unfortunately, the phase iii dynamics too is not grasped by the EEC because there is no

current flow.

The EEC confirms the possibility to use this kind of simplification for electrochemical systems subjected to temperature gradients, both from a dynamics (in case of flowing current) and a steady-state points of view.

4.4 Dynamics

In order to verify the accuracy of the solutions, a complete comparison between the analytical solutions, numerical simulation and equivalent circuit representation must be made in the time domain.

Phase i

The phase i dynamics for a planar electrode capacitor was already studied both by Janssen [63] and Stout [58]. The comparison is here made to have a clearer view, especially in the comparison between an "instant temperature gradient" approximation, in which the temperature gradient in the electrolyte is considered built instantaneously, and "dynamic temperature gradient", in which the right electrode temperature is imposed to be $T_0 + \Delta T$ and the electrolyte approaches the thermal final steady-state dynamically.

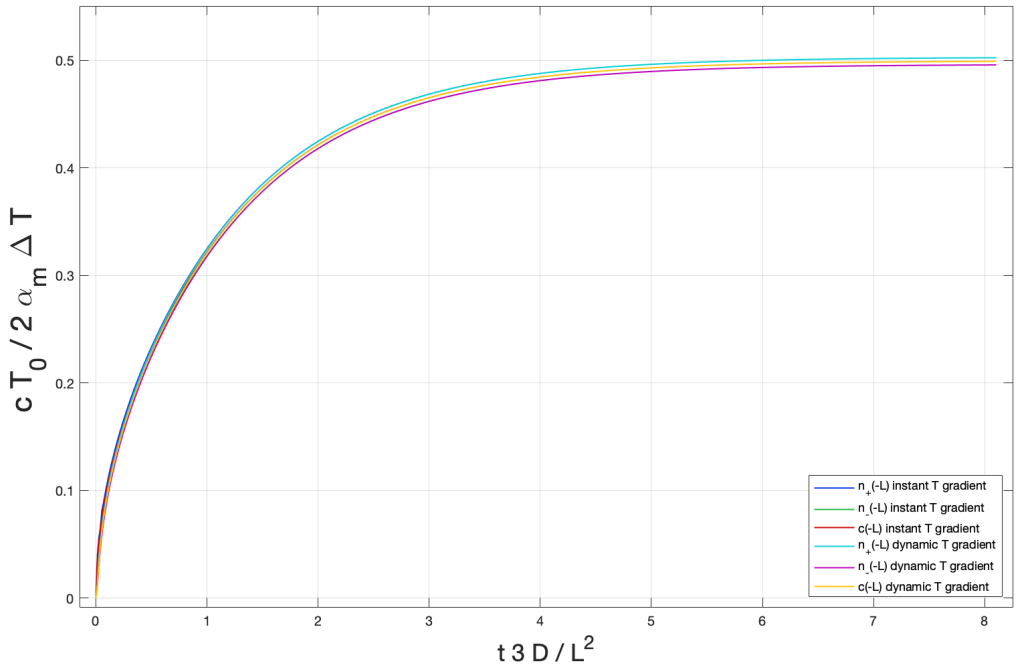

Figure 4.7: Dimensionless neutral density $cT_0/2\alpha_m\Delta T$ at the left electrode surface $(-L)$ vs the dimensionless time $3Dt/L^2$, in the two case: "instant temperature gradient" and "dynamic temperature gradient". The single positive and negative dimensionless ion densities $((n_\pm(-L)/n_0 - 1)T_0/2\alpha_m\Delta T)$at the left electrode are plotted too.

Regarding the EEC, phase i cannot be studied with that method due to the absence of surface charge development, so only a comparison between simulations and analytical results will be made.

The time behaviour of the neutral density at the left electrode was taken into account and plotted in figure 4.7. The simulation was carried out considering both the possible time behaviour of temperature profile. The analytical solution indicated a time constant of $L^2/3D$, which is confirmed by the simulation, both in the case of instantaneous and dynamic temperature gradient. This is due to the long time required to reach the equilibrium for the neutral charge which is much longer than τ_T (eq 4.1.8). The differences between the two cases is so negligible, so, from now, on the neutral charge will be considered respecting the analytical time constant found.

A last comment can be done on the single-ions densities at the electrode which grows almost identically in phase i, both pushed by the Soret force. Even if the force is different due to different Soret coefficients, the electrostatic attraction between the two species imposes a common dynamic, the separation is present only when the two species are in contact with a surface as the electrode.

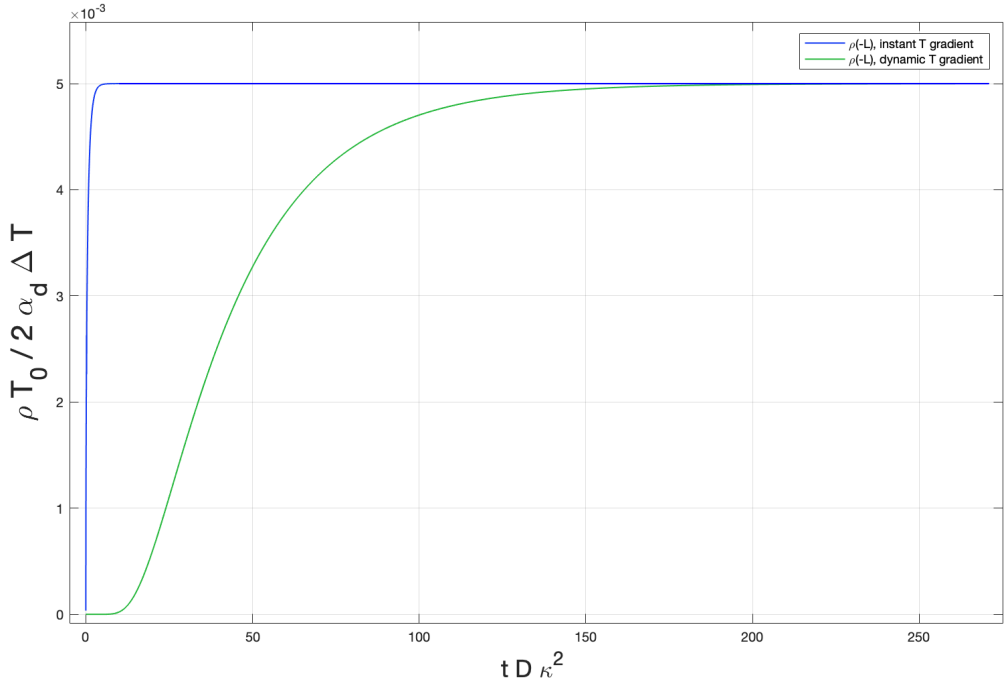

Figure 4.8: Dimensionless charge density in the left electrode $\rho(-L)T_0/2\alpha_d\Delta T$ vs the dimensionless time $tD\kappa^2$. In blue is represented the dynamics in case of instant temperature gradient, in green in case of dynamic temperature gradient.

The charge density behaviour (fig. 4.8) is instead strongly affected by the temperature time constant. The dynamics of the instant temperature gradient case respect precisely the time constant analytically found $(1/\kappa^2 D)$. Instead, if the simulation is done simply imposing the right electrode to be at $T_0+\Delta T$ at $t = 0$, the need to wait for the temperature profile to be developed shifts the charge density dynamics toward much higher times. In particular, calculating the temperature's time constant with the data inserted in the

simulation $\tau_T = 2.8 \cdot 10^6 L^2$ and the charge density time constant $\tau_\rho = 10^9/\kappa^2$, having chosen $L\kappa = 100$, results

$$\tau_T \simeq 28\tau_\rho \tag{4.4.1}$$

Considering $5 \cdot \tau_T$ as the time needed to reach the steady-state, it is clear when the $140/D\kappa^2$ visible in the graph comes from. The surface charge is 0 in phase i, so its time behaviour cannot be analysed.

The dynamics of the potential was already found in the analytic solution and the Poisson equation, that connects the functions, is time-independent so the dynamics of the potential and the charge density are linked. The work of Stout and al. already demonstrated that, in the case of instantaneous temperature gradient, the characteristic time is half of one for the charge density. If a dynamic temperature gradient is considered, the limiting factor will be again the temperature time.

Phase ii

The phase ii is, instead, a good field in which the equivalent electrical circuit can be tested, in order to assure its feasibility for the next improvements to the model.

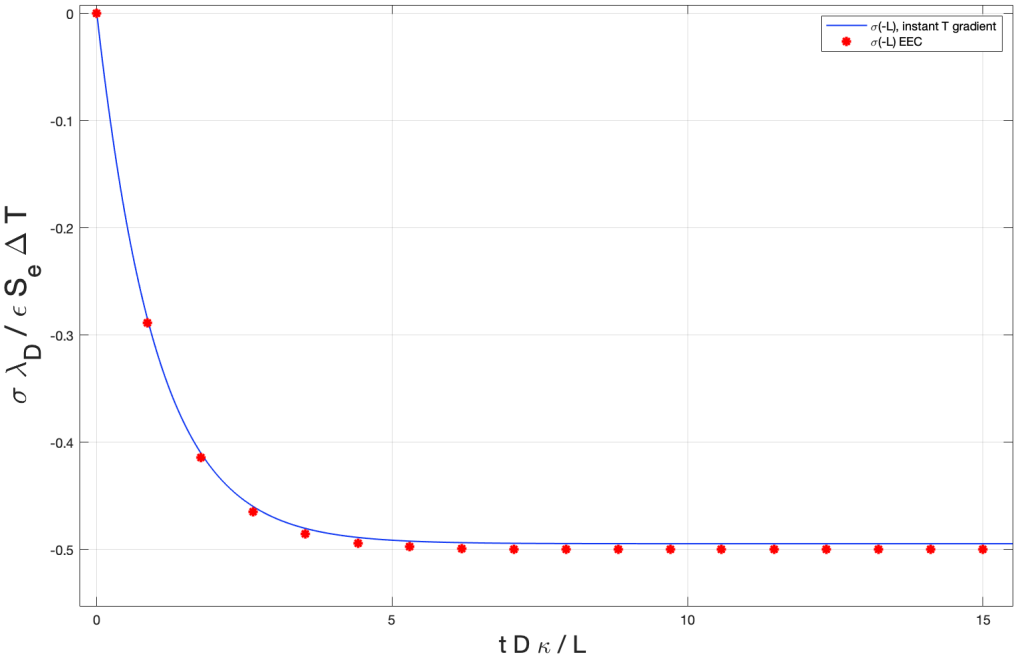

Figure 4.9: Dimensionless surface charge density in the left electrode $\sigma\lambda_D/\epsilon S_e \Delta T$) is plotted vs the dimensionless time $tD\kappa/L$. The numerical result is plotted with the blue solid line, the equivalent electrical circuit solution is plotted with the red asterisks.

As it is possible to see in figure 4.9, the evolution in time of phase ii is well approximated by the circuit solution which final equation is eq.(4.3.10). It is important to state that,

for the phase ii, only the solution in which the temperature gradient is applied instantly has sense, since in the experiments the system passes in phase ii only when phase i is completed and so the temperature gradient is established.

The time needed to reach the steady-state is $5 \cdot L/D\kappa$ in the numerical simulation and in the EEC solution. The final value is almost perfectly in accordance between the simulation and the analytical result: 0.492 in dimensionless units from the simulation and 0.495 from the equations. A slight difference between with the EEC solution is present (the value is 0.5), but it must be considered that the circuit resulting use an electrode capacitance that holds perfectly only for a completely ideal EDL (eq. 4.3.10), but it is already been underlined the particular shape of the potential in phase ii and the presence of the term $1/L$ in the analytic solution, which explains the differences obtained.

The overall approximation with the EEC it is satisfying, so it can be used from now on as a reference method.

The electrical potential will follow necessarily the same dynamics as the surface charge, but a comparison between numerical and analytical results cannot be made here due to the necessity of the FEM program. Comsol can support two steps solution, but in this specific case the B.C. changes abruptly between the steps, it is so necessary to choose for the second steps $\psi(-L) = 0$, so that the dynamics of the other variables is physically realistic. This provides a step-like function for the potential that goes from $S_e\Delta T$ to 0 instantly. The other possibility was to choose a change of the surface charge, from 0 to the steady-state value of phase ii, imposed by the program user, but it would modify the physical dynamic behaviour of the system.

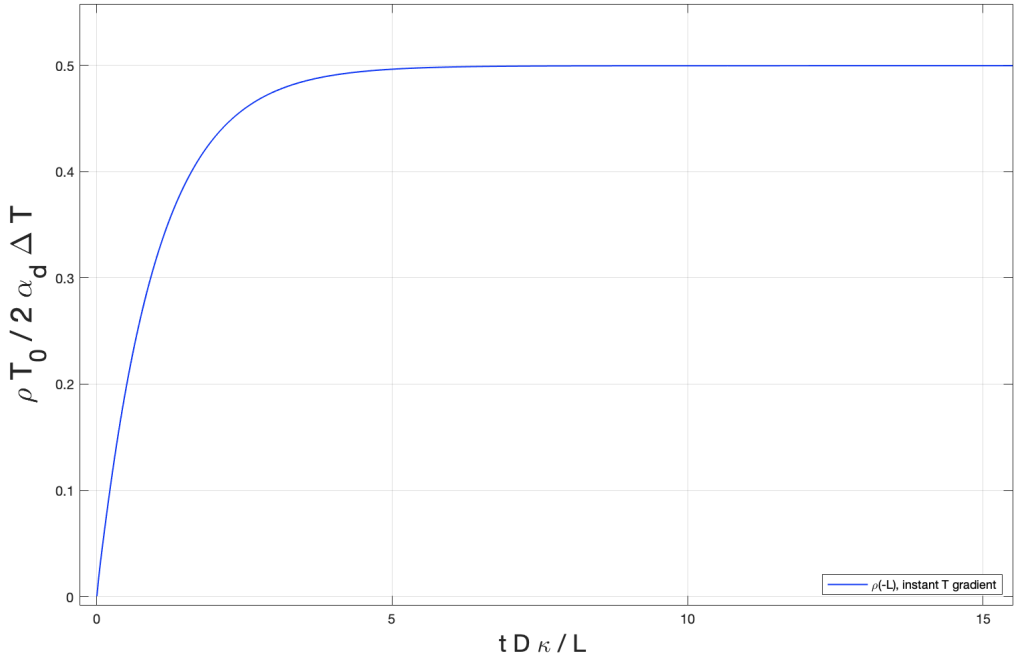

Figure 4.10: Dimensionless charge density in the left electrode $\rho(-L)T_0/2\alpha_d\Delta T$ vs the dimensionless time $tD\kappa/L$.

Regarding the charge density in $-L$, which is taken as a reference value, the EEC does not provide a solution, but a comparison can be made between the numerical and the analytical solution. In this case, the match between them is almost perfect considering the absolute value.

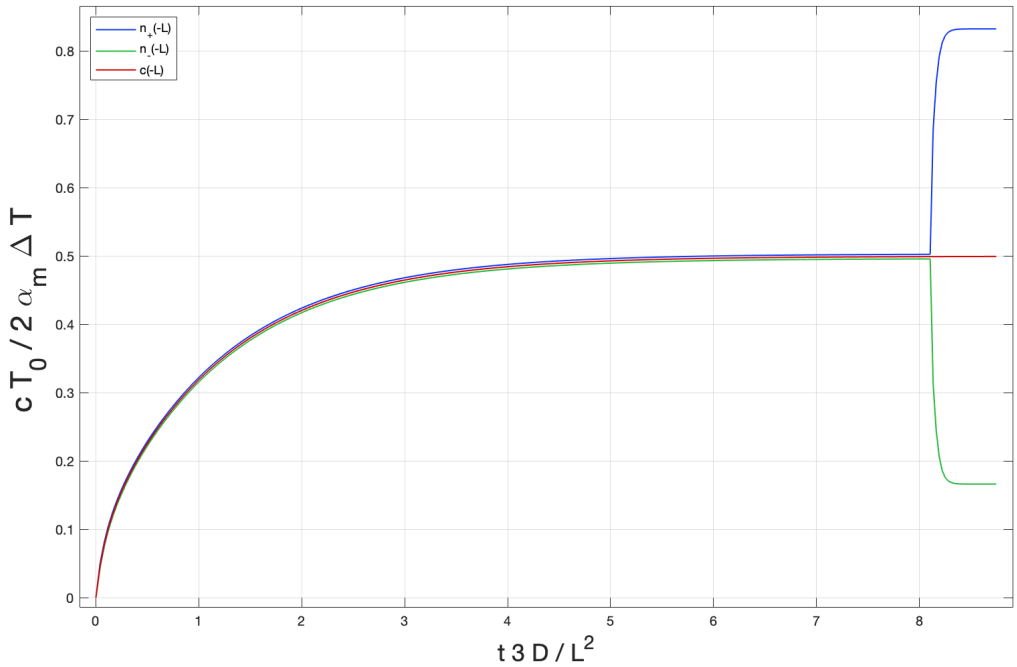

Figure 4.11: Dimensionless neutral density $c(-L)T_0/2\alpha_m\Delta T$ vs the dimensionless time $3Dt/L^2$ (red line). The single positive (blue line) and negative(red line) dimensionless ion densities at the left electrode ($(n_\pm(-L)(n_0-1)T_0/2\alpha_m\Delta T$) are plotted too.

Considering now the behaviour of c in $-L$ during phase ii in figure 4.11, we can observe how the neutral density it is not affected by the change in the boundary conditions, that happens when phase ii is started, and it continues to migrate towards the cold electrode pushed by the Soret force. In particular, a two-step simulation is done and phase ii starts after letting the neutral density reach the steady-state. It is evident how the start of phase ii changes the curves of n_+ and n_-, which are responsible for the charge density build-up at the cold electrode, without affecting the curve for c that follows, as expected, an exponential behaviour with a time constant $\tau_c = L^2/3D$. The big difference existing between τ_ρ and τ_C creates a situation in which it is convenient starting phase ii just after the development of the charge density, without waiting for the neutral charge to reach an equilibrium. This does not permit the full development of the neutral density in the time required to charge the capacitor. The fact that the successive phases start before this full development seems to not create a particular effect on the behaviour of the charge density and the potential.

It could be interesting to analyse the behaviour of this system with an high-frequency cycle, in which the circuit is open and closed and the temperature is varied before the

variables reach the steady state-values, but this goes beyond the scope of this work.

Phase iii

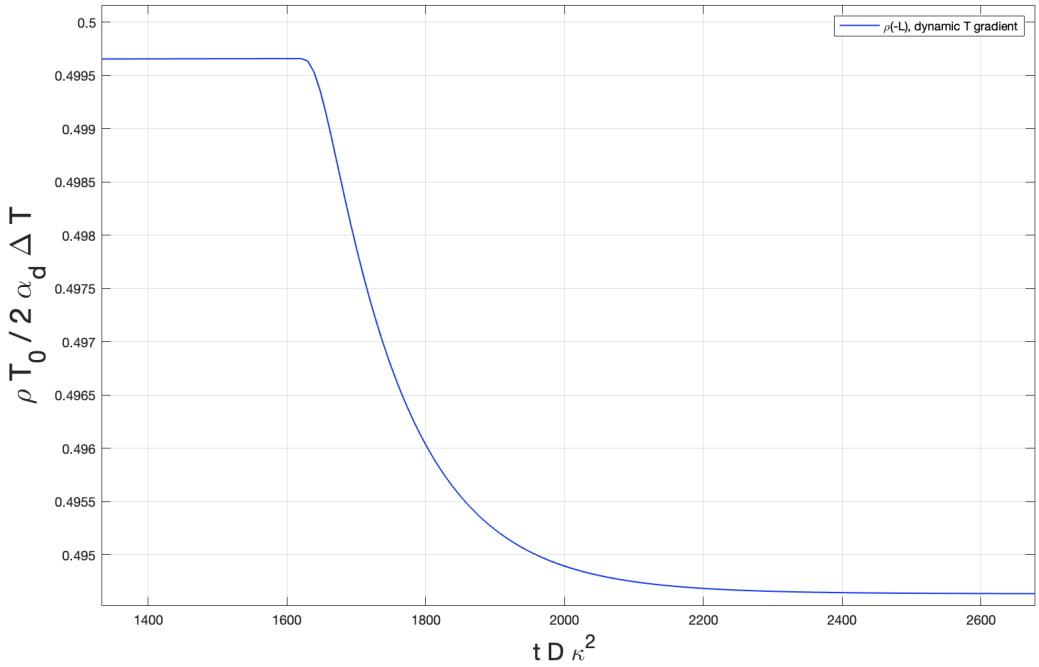

Figure 4.12: Dimensionless charge density at the left electrode $\rho(-L)T_0/2\alpha_d\Delta T$ vs the dimensionless time $tD\kappa^2$.

The dynamics of the phase iii charge density should be the same of phase i with a time constant of $1/D\kappa^2$. Unfortunately, in the numerical simulation visible in figure 4.12, it is only possible to impose initial values with a temperature gradient already set. To simulate phase iii it was instead necessary to start from phase ii and add a step, that used the precedent final state as initial condition. This method does not provide a precise analysis, but, to grasp the behaviour of phase iii, it was necessary. Starting from the steady-state of phase ii and imposing at the right electrode a sudden temperature drop from $T_0 + \Delta T$ to T_0, while imposing the conservation of the surface charge, the system takes time to reach a constant temperature profile. The temperature-time affects greatly the dynamics of phase iii, as it is possible to see in figure 4.12, in which the small drop in the charge density at the left electrode is represented.

It is however relatively less important to understand the behaviour of the third phase because the goal to charge the capacitor completes in phase ii, the rest of the process does not use external energies or inputs. For the reasons exposed so far the phase iii study will not be developed more.

To have a clearer overall picture, figure 4.13 represents the behaviour of the charge density value in $-L$ during the three phases. The figure was plotted superimposing a phase ii-phase iii transition over the phase i dynamics. This was done to overcome the limitations of the program that permits only a two-step dynamic simulation.

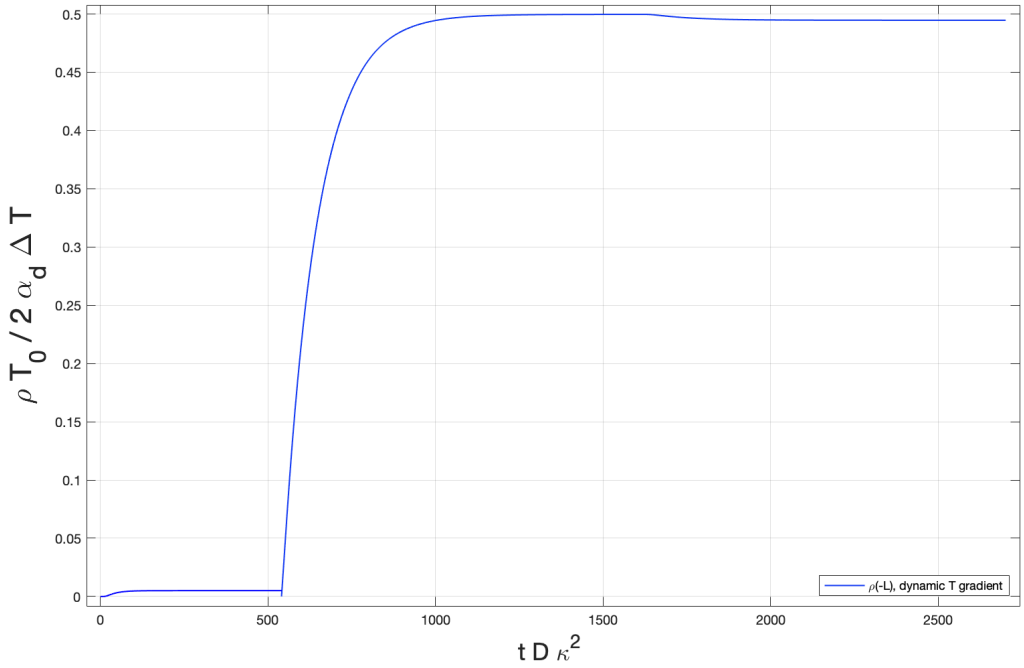

Figure 4.13: Dimensionless charge density at the left electrode $\rho(-L)T_0/2\alpha_d\Delta T$ vs the dimensionless time $tD\kappa^2$.

Despite this problem, the result clears how the charge density initially builds up only due to the Soret effect, then grows when the circuit is open, and finally drops the part related to the temperature effects when the gradient is removed.

Supercapacitor Under Temperature Gradient

If the behaviour of an electrochemical capacitor with planar electrodes is trivial, once the equations are known, the same thing cannot be said for the case of nanoporous electrodes. The various ways in which it is possible to model a nanoporous electrode are summarized in Chapter 2.

In order to obtain a result that is expandable on large scales, and can predict easily the space-dependent and time-dependent behaviour of a nanoporous electrode supercapacitor, subjected to a temperature gradient, the "*stack electrode model*" (SEM) was chosen. This method permits to analyse the impact of a temperature gradient, not only in the bulk electrolyte, but in the nanostructured electrode as well. The possibility to expand the solution to a high number of pores and to macroscopic distances, permits also us to understand what could be the optimal geometry, in terms of pore size and electrodes thickness.

The dynamics can also be well studied using the SEM method, permitting to make the same considerations done with the planar electrode device and so to compare the results. It is also possible to reproduce the system with an EEC, providing a strong tool to model in general an electrolyte in a temperature gradient.

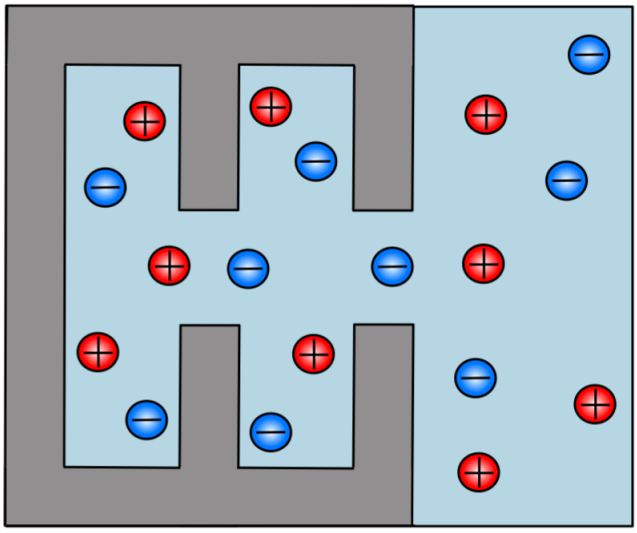

Figure 5.1: Sketch of a nanoporous carbon electrode modelled as simplified in a stack electrode model.

Within the advantages of the SEM, there is the fact that it replicates a simple system in which a neutral macropore goes from the reservoir to the impermeable end of the electrode, with a series of micropores perpendicular to it. This simplification allows us to imagine the system as represented in figure 5.1.

The simple visualization of the system is a key tool that permits to understand if the simulation results are physically reasonable. In fact, the scarce scientific literature present on electrolyte's Seebeck effect is of little use to check the results, letting only to the physical intuition the task to confirm what will be obtained.

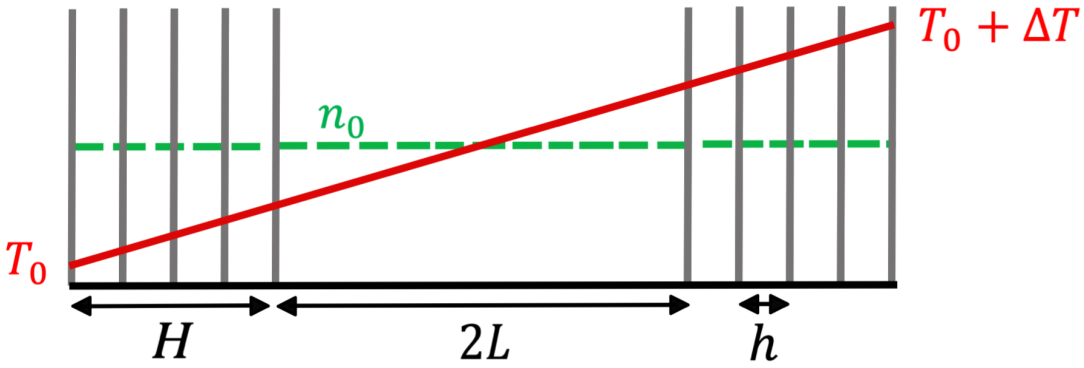

Figure 5.2: Sketch of a stack electrode model in a temperature gradient. The green line represents the initial ion concentration, the red line represents the temperature profile. The cell has a length of $2L + 2H$ in which the origin $x = 0$ is posed in the center, L is half the length of the reservoir, H is the length of the nanoporous carbon electrodes and h is the pore length.

The geometry of the nanoporous electrode is rapidly defined: the reservoir, as for the planar electrode, extends from $-L$ to $+L$, the n stack electrodes will be separated by the length h, going from $-L$ to $-L - H$ and from $+L$ to $+L + H$ respectively. Obviously H can be defined as

$$H = (n - 1)h$$

The electrodes are fully permeable with the exception of the nth ones, which close the system.

Parameters

The presence of a nanoporous electrode arises some questions on the relationship between the thermodynamic parameters in the electrode with respect to their value in the bulk electrolyte.

The thermal conductivity choice becomes important: it modifies the temperature gradient, so its value has a big impact on the overall temperature-related effect in the electrodes. Considering the most common choice of carbon electrodes, it is logical to think that the carbon electrode thermal conductivity is much higher than the one of the aqueous electrolyte, leading to almost no temperature difference in the nanostructure. It is instead

surprising the experimental result of Burehim and al.[66] that found a much lower thermal conductivity than expected. In particular the similarity between the conductivity of the soaked carbon electrode (0.47 $WK^{-1}m^{-1}$) and the electrolyte (TEA-BF4), together with dry carbon conductivity (0.09-0.19 $WK^{-1}m^{-1}$) that is even lower than the soaked one, let think that the main heat driver in the electrode is the electrolyte. This can be physically explained by thinking about the high phonon scattering present in a nanostructured carbon and the low heat transfer at the carbon-electrolyte interface. A complete model that describes this system and can calculate this data is not present in literature, when the electrolyte is different from the one experimentally studied it is therefore only possible to make educated guesses.

The previous considerations are however sufficient to state that it is possible to use as thermal conductivity, for the nanoporous carbon electrode, the one of the electrolyte. This choice simplifies the computational work eliminating a discontinuous derivative without losing excessive precision in the results.

Regarding the other parameters, the choice is related to the space scale studied: remembering that the SEM is a representation of a large macropore that connects the micropores, it is possible to conclude that the diffusion D coefficient is not affected by the nanoporous electrode because the ions are free to move in the macropore. This can be seen as a strong approximation, but considering instead the diffusion coefficient of a bulk nanoporous material it is not correct, because a part of the nanoporosity effect on the ion motion is already included in the presence of the multiple electrodes and because its value is found averaging on multiple pores. The optimal value should be something in between the bulk electrode's and the reservoir's values, but in absence of further theoretical consideration it is more physically reasonable to choose the reservoir's value.

Same considerations can be applied to the Soret coefficient α and dielectric permittivity ε. The value of the latter is affected by the presence of the carbon, but the studies always consider the mean value averaging on the entire bulk electrolyte-electrode system. The standard values are then used in the electrode part, in absence of better theoretical evaluations.

Once the correct theoretical interpretation of the parameters exposed so far will be done, it will be possible to modify the present model obtaining more precise results, without the need to develop entirely a new method.

5.1 Simple System: Two-Electrodes Solution

Before explaining a complete stack electrode model with n electrodes, it is necessary to examine an $n = 2$ system.

This simplification permits to grasp the main differences between a planar and a nanostructured electrode, posing all the new physical effects in an easy and intuitive solution. It is also possible to solve analytically the equivalent electrical circuit for $n = 2$, understanding precisely the relations between the various parameters present. The initial boundary condition are still valid, considering now the new geometry of the problem:

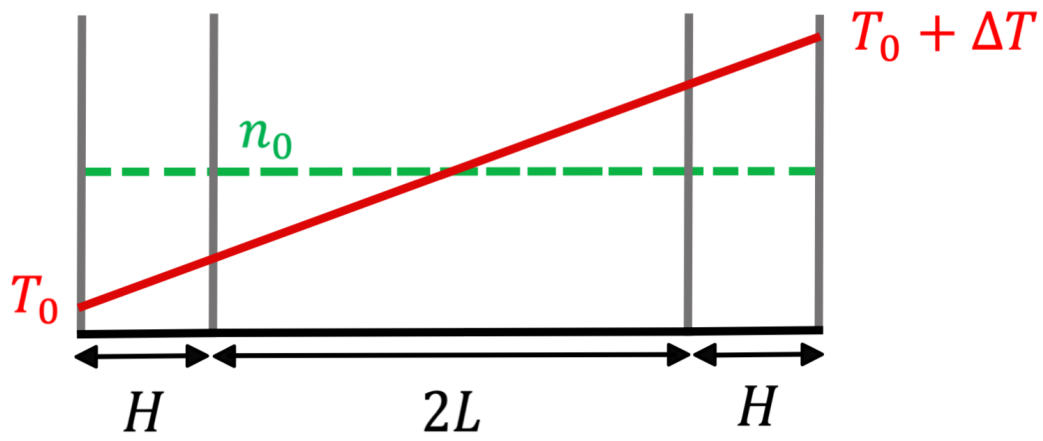

Figure 5.3: Sketch of a two electrode model in a temperature gradient. The green line represent the initial ion concentration n_0, the red line represent the temperature profile. The cell has length of $2L + 2H$ in which $x = 0$ is posed in the center, L is half the length of the reservoir, H is the distance between the electrodes.

$$T(x, t < 0) = T_0$$

$$n_{\pm}(x, t < 0) = n_0$$

$$j_{\pm}(\pm L \pm H, t) = 0$$

The presence of two electrodes per side imposes new boundary conditions, in particular related to the electrical part of the problem. These conditions vary during the phases and are summarized below. It is useful to consider the symmetry of the problem, this allows us to study in-depth just one side of the capacitor knowing that the behaviour of the other electrode will be symmetrical. For these reasons the B.C.s exposed below considers only the left part of the capacitor (the cold one). The outer electrode in $-L - H$ will be referred to as the electrode 2, the inner electrode in $-L$ will be referred to as the electrode 1, and consequently they will be called the variables related to those electrodes.

The new boundary conditions, in the various phases, will be so presented.
Regarding the temperature, the condition for phase i remains the same:

$$T(+L + H, t) = T_0 + \Delta T \, .$$

The major difference between the planar electrodes capacitor and the nanoporous one is instead related to zero surface charge condition of the phase i. It must be remembered indeed that in phase i the overall surface charge in both the nanopours electrodes must be 0 because the electrodes are not connected to each other, this has an important implication for the nanoporous system. In the two-electrodes case this means:

$$\sigma_1 + \sigma_2 = 0 \tag{5.1.1}$$

Moreover, the two electrodes on the same side are connected being part of the same conductive structure. In the approximation of infinite electrically conductive carbon (that holds if compared to the electrolyte conductivity), their potential must be the same:

$$\phi_2(-L-H,t) = \phi_1(-L,t) \tag{5.1.2}$$

It is important to consider that now the inner electrode is in contact with the electrolyte on both sides. This means that an EDL will develop on both sides too, giving the first electrode, in case of fully developed EDLs, double the capacitance of the second, which has only one part facing the electrolyte. The difference in the capacitance is a key factor, that is crucial to understand the particular shapes the charge density and the potential will acquire.

The phase ii is characterized by the connection of the two electrodes. This implies that all the electrodes in the supercapacitor will have the same potential, in particular, it is set to 0 by the ground connection. The electrons can now flow so no surface charge limitation is present. Considering, as usual, the left electrode the B.C. results:

$$\phi_2(-L-H,t) = \phi_1(-L,t) = 0 \tag{5.1.3}$$

The temperature remains the same with the imposition of $T_0 + \Delta T$ in $+L+H$.

The phase iii for nanoporous electrode shows a new equilibration behaviour. Once the temperature gradient is removed in open circuit, the overall surface charge accumulated in the electrodes will be conserved and it will be distributed according to the capacitance of the electrodes. In particular, the electrodes on the same side will still have the same potential

$$\phi_2(-L-H,t) = \phi_1(-L,t)\,, \tag{5.1.4}$$

and regarding the charge equilibration, it is sufficient to state that

$$\sigma_{1,\,phase\,ii} + \sigma_{2,\,phase\,ii} = \sigma_{1,\,phase\,iii} + \sigma_{2,\,phase\,iii} \tag{5.1.5}$$

to have automatically, from the set of the governing equations, the correct redistribution of charges in the various electrodes.

5.1.1 Numerical Results

The presence of a second electrode in the stack arises a series of complications for the analytic solution. In fact, with just two electrodes per side, the system must be divided into three parts, posing the boundary conditions expressed so far, in order to be solved analytically. The linearised PNP equations are so, in principle, solvable for any number of electrodes in steady-state.

The analytical results, that can be obtained with just two electrodes, is however composed by pretty long equations, not simplifiable, from which is hard to grasp any physical interpretations. Moreover, antitransform the Laplace transform calculated, in order to obtain the time-dependent behaviour, is not possible. Imaging to do the same for n electrodes, it is natural to conclude that the analytical solution is not a useful tool for the aim to model a high number of electrodes.

The obvious conclusion is to use again a FEM numerical method and an equivalent electrical circuit, to compare the two and to understand the physics behind the results.

The parameters chosen for the simulation are the same as for the planar electrode except for L and H, which are chosen respectively so that $\kappa L = 75$ and $\kappa H = 25$, to have the same overall length as before.

The numerical results are exposed below

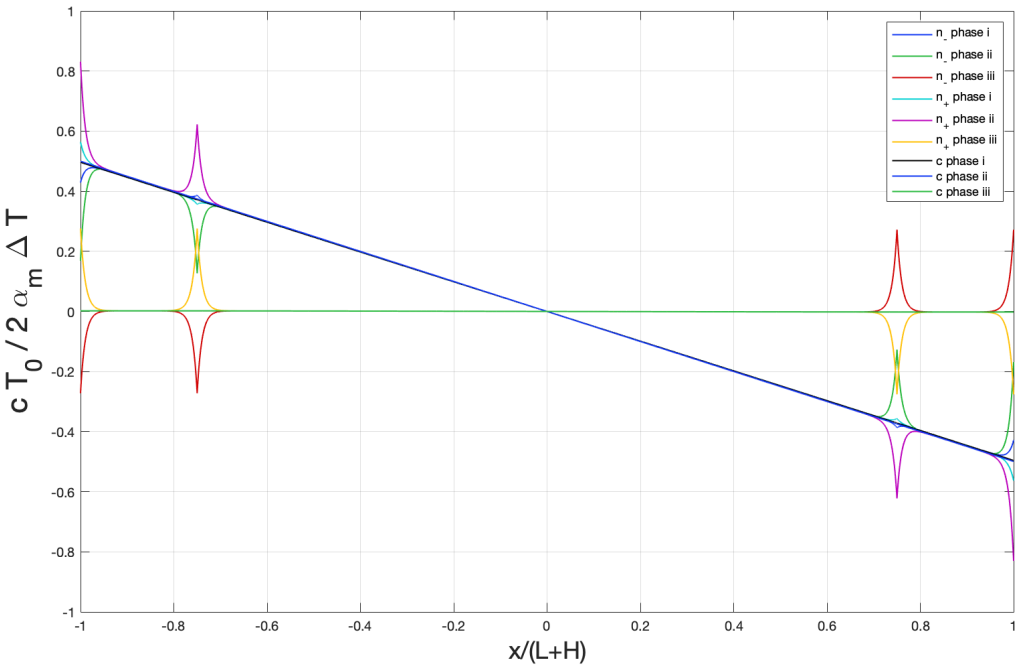

Figure 5.4: Numerical solutions of the dimensionless neutral density $cT_0/2\alpha_m\Delta T$ vs the dimensionless length $x/(L+H)$ during the phases. The ions distribution are also represented in the graph.

As it is possible to see in fig. 5.4, the neutral charge is not affected by the presence of a second electrode so, having the same parameters, it will have the same behaviour as in planar electrode. This statement can be already generalized to any number of electrodes. It is also possible to visualize the ions distributions in phases and to see how they deviate from the perfectly linear graphs in correspondence of the electrodes.

The charge density, pictured in fig. 5.5, has instead a peculiar behaviour: during phase i the first electrode has a negative charge density accumulated on its sides. The origin of this phenomenon must be traced in the condition of charge neutrality during the open circuit phase. It is easier to understand the reasons looking at the figure 5.6.

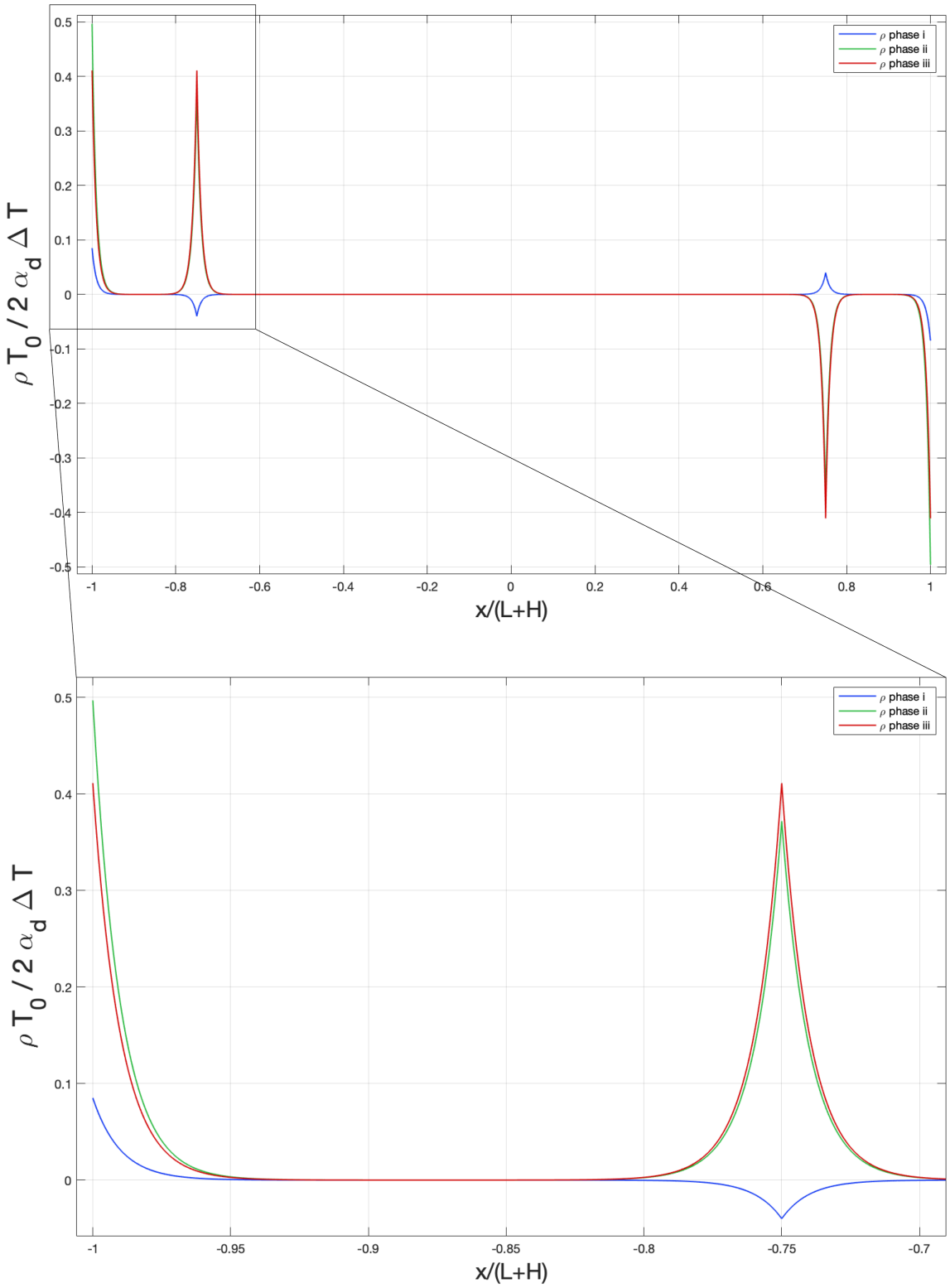

Figure 5.5: Numerical solutions of the dimensionless charge density $\rho T_0/2\alpha_d\Delta T$ vs the dimensionless length $x/(L+H)$. A zoom of the left electrode is also present.

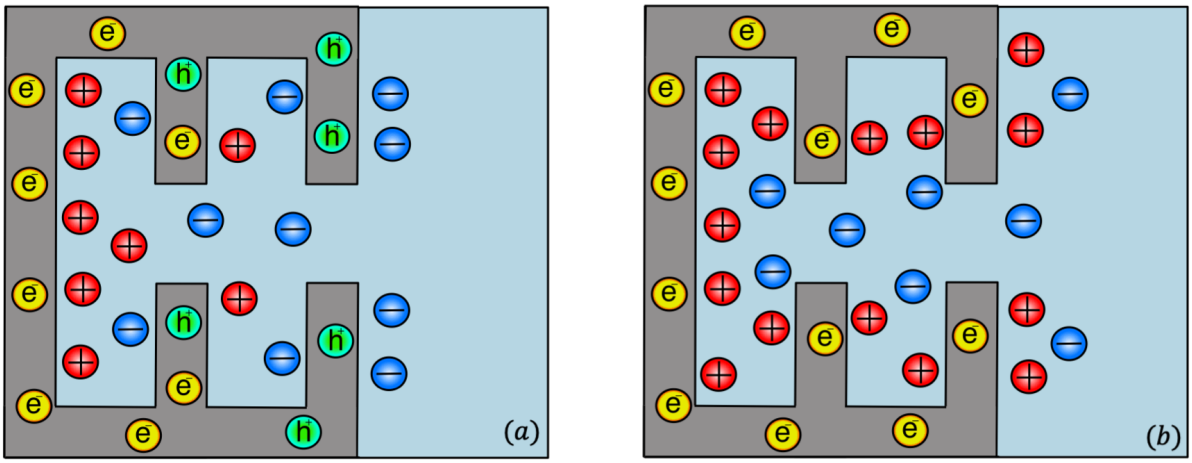

Figure 5.6: Sketch of the model. Phase i representation figure (a), when the conservation of surface charges is present. The holes are meant to represent the average positive charges on that electrodes, not actual holes. Phase ii is represented in figure (b) when the circuit is closed and the electrons can flow freely inside the carbon.

The ions are pushed from the reservoir to the impermeable boundary, ergo to the second electrode. The positive ions, having a higher Soret coefficient, will reach the last electrode in a greater number than the negative ions, attracting the electrons present in the carbon and creating a negative surface charge on the second electrode. Due to the neutrality condition, the first electrode will be positively charged, attracting consequently the negative ions on its surface, until a steady-state condition is reached.

Physically the Soret effect is present in the pore too, especially in this case in which the pore is relatively large. The potential it creates must be balanced by an electric potential that is sufficient when an opposite charges are present in the two electrodes.

Another interesting phenomenon is that, in the nanoporous electrode case, an EDL is developed at the electrodes even during phase i. This, as will be seen, modifies sensibly the dynamics of the phase i.

Concerning the phase ii, the short circuit condition, let the EDLs be fully developed at the end of the transitory. The Soret potential clearly shifts the charge density distribution, now totally positive, against the colder side. It is interesting to notice how the maximum charge density of the second electrode coincides with the one obtained in the planar-electrodes simulation, and consequently, the surface charge accumulated also coincides. The reason relies on the fact that the ions are continuously pushed by the Soret force to the cold electrodes and the main force that stops this motion is the electrostatic repulsion. When an electrode is present and connected to the ground it will be charged minimizing the electrostatic repulsion, independently from the presence of other electrodes connected.

The phase iii is now simply an equilibration phase in which, removing the temperature gradient, the charges equilibrate according to their capacitance. Remembering that the capacitance of the first. Is two times the one of the second electrode, having the two the same potential, it is natural to observe the same values of the peak charge density on the

electrodes.

The superposition of effects is confirmed too: it is observable in the numerical solution and, thinking about the motion of the ions as done in figure 5.6, it is logical to conclude that the charge unbalance developed in phase i will be present in phase ii too and it will be removed in the third phase.

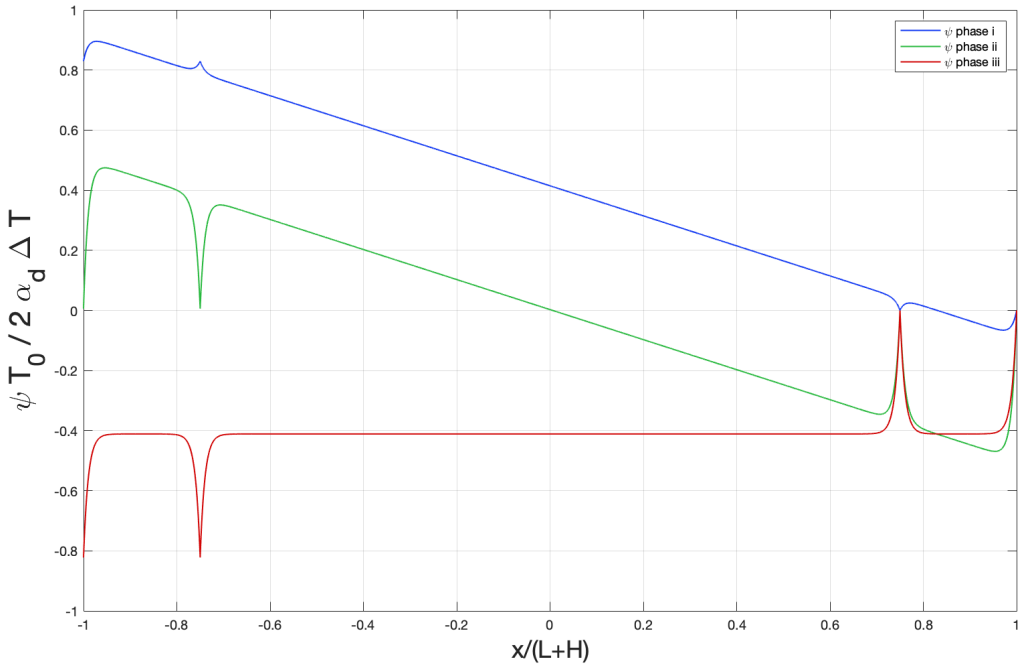

Figure 5.7: Numerical results of the dimensionless potential $\psi T_0/2\alpha_d\Delta T$ vs the dimensionless length $x/(L+H)$.

The results for the potential represented in figure 5.7, are no surprise once the system is understood.

The phase i function presents the same slope as in the planar-electrodes case, with the exception of the peaks corresponding to the electrodes. The two peaks can be interpreted both mathematically and physically: mathematically the necessity to preserve the same slope present in the bulk, combined with the needs to have the same potential in the two points give origin to the peaks; physically they are the results of the double layers created in the process and their pointing up or down is related needed to accommodate respectively for negative and positive ions.

An interesting aspect is that the value of the potential in contact with the second electrode is slightly lower with respect to the planar-electrodes case, due to the formation of a double layer. This small difference is hardly detectable experimentally if a realistic high thickness device is considered, this explains why the experiments show almost the same behaviour for planar and nanostructured electrodes.

Analysing now the phase ii, it is clear how the slope is not modified, and the maximum values near the second electrode are the same observable in the planar electrode case. The overall function is practically the same as the planar electrode case, with the exception of the first electrode presence, which creates a second downward peak.

The phase iii potential is again a simple potential of a charge supercapacitor as found in the work of Lian and Co [40], and the superposition of effects is confirmed.

The numerical results for the two-electrodes set-up have found non-trivial behaviours, especially for the charge density. The similarities with the planar-electrodes case allow to generalize the informations obtained, including the analytical solutions, to a multiple electrodes system, using them to have an idea of the behaviour during the phases.

5.1.2 Equivalent Electrical Circuit

As previously done for the planar-electrodes case, an equivalent electrical circuit for a nanoporous electrodes case, in particular for two electrodes, can be developed.

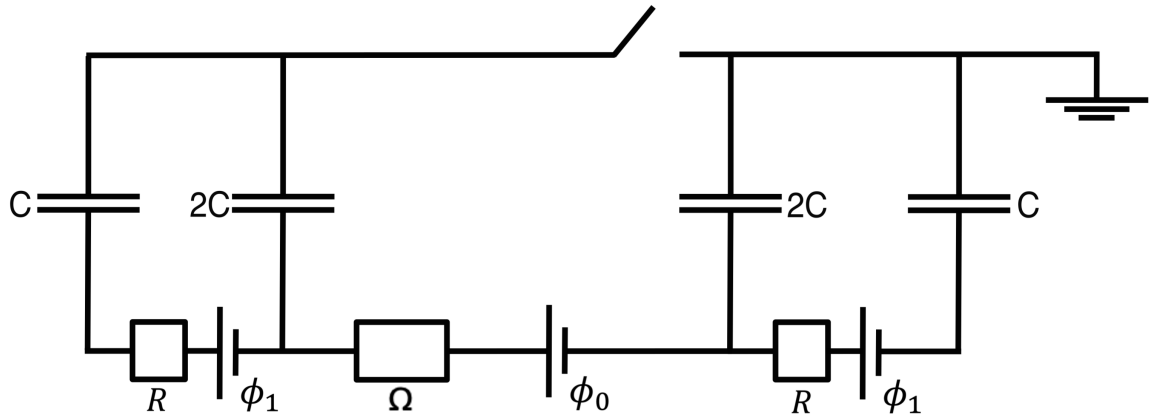

Figure 5.8: Equivalent electrical circuit for a $n = 2$ electrode nanoporous carbon supercapacitor subjected to a temperature gradient.

As represented in figure 5.8 this EEC will have a voltage generator in the reservoir and in between every electrodes, to express the presence of the Seebeck effect in all the electrolyte, including the part in the pores. Of course, the voltage applied by the generators will be proportional to the local temperature difference, so that

$$\Phi_0 = S_e \frac{\Delta T}{L + H} L \tag{5.1.6}$$

$$\Phi_1 = S_e \frac{\Delta T}{2(L + H)} H \tag{5.1.7}$$

Same considerations hold for the resistances present:

$$\Omega = \frac{L}{\sigma_{el}} \tag{5.1.8}$$

$$R = \frac{H}{2\sigma_{el}} \tag{5.1.9}$$

Another difference with respect to the planar-electrodes case, is that the specific capacitance of the capacitors, which accounts for the EDLs developed in the inner electrodes, is double respect to one of the outer capacitors. So that

$$C_1 = 2C_2 = 2\frac{\varepsilon}{\lambda_D} \tag{5.1.10}$$

The circuit can now be solved.

Phase i

Starting from the phase i in which the circuit is open, it appears immediately that, for the two-electrodes set-up, this phase has now a time-dependent solution and the capacitors result charged at the end of the transitory.

The physical charge neutrality condition in the carbon nanostructure is reformulated here in terms of an EEC:

$$Q_1 = 2C\Delta\Psi_1 \tag{5.1.11}$$

$$Q_2 = C\Delta\Psi_2 \tag{5.1.12}$$

$$Q_1 + Q_2 = 0 \tag{5.1.13}$$

Applying Kirchhoff's laws to the left circuits

$$I_1 R = \Delta\Psi_2 - \Delta\Psi_1 + \Phi_1 \tag{5.1.14}$$

Where I_1 is the current flowing, remembering that the direction of the current must be considered carefully because, in this case, it modifies the values of the voltage drops derivatives:

$$I_1 = 2C\Delta\dot{\Psi}_1 \tag{5.1.15}$$

$$I_1 = -C\Delta\dot{\Psi}_2 \tag{5.1.16}$$

Substituting the variables and solving the ordinary differential equation the results are straightforward :

$$\Delta\Psi_1 = \frac{1}{3}\Phi_1(1 - e^{-\frac{3t}{2RC}}) \tag{5.1.17}$$

$$\Delta\Psi_2 = -\frac{2}{3}\Phi_1(1 - e^{-\frac{3t}{2RC}}) \tag{5.1.18}$$

Thus, the time constant of the system is $\tau = 2RC/3$ with $RC = H/\kappa D$. This time constant is very different from the one of the same phase of the planar-electrodes case. This can be explained considering that, in this case, the double layers can be formed in phase i and, as it is known, the formation of an EDL has its particular time constant proportional to the RC time of the system.

To calculate the absolute values of the potential at the ends of the capacitor, the voltage generators Φ_0 and the Φ_1 on the right side must be considered, even if the central circuit is open. This provides us with the values found in figure 5.7.

For example to calculate the voltage measured experimentally it is sufficient to look for the voltage in the outer left electrode:

$$\Delta V = \Phi_0 + \frac{2}{3}\Phi_1 = S_e \frac{\Delta T}{L+H}\left(L + \frac{1}{3}H\right)$$

that, with $H = 1/3 \cdot L$ as in the simulation above, becomes

$$\Delta V = \frac{5}{6} S_e \Delta T$$

demonstrating why the presence of the nanoporous electrodes does not effect excessively the voltage measured in the experiments.

Turning now to discuss the surface charge density, here represented by the values of Q_1 and Q_2, in steady-state we obtain an equal end opposite surface charge in the two electrodes:

$$Q_1 = \frac{2}{3} C\Phi_1 = \frac{1}{12} C S_e \Delta T \ , \ Q_2 = -\frac{2}{3} C\Phi_1 = -\frac{1}{12} C S_e \Delta T$$

as observed in the simulations. Of course, the right circuit behaves symmetrically.

Phase ii

To solve the circuit representing the phase ii, it is sufficient to solve it once it is closed.

Calling I_0 the current flowing in the reservoir resistance Ω, I_1 and I_2 the currents flowing respectively in the inner and the outer capacitors, from the definition of current

$$I_1 = -2C\Delta\dot{\Psi}_1 \ , \ I_2 = -C\Delta\dot{\Psi}_2$$

so that the following system of equations is obtained:

$$I_0 = I_1 + I_2 \tag{5.1.19}$$

$$2\Delta\Psi_1 + \Phi_0 - \Omega I_0 = 0 \tag{5.1.20}$$

$$\Delta\Psi_2 - \Delta\Psi_1 + \Phi_1 - R I_2 = 0 \tag{5.1.21}$$

which can be rewritten in a more convenient form:

$$\Delta\dot{\Psi}_1 = -\frac{I_1}{2C} = -\Delta\Psi_1\left(\frac{1}{\Omega C} + \frac{1}{2RC}\right) + \Delta\Psi_2 \frac{1}{2RC} - \frac{\Phi_0}{2\Omega C} + \frac{\Phi_1}{2RC} \tag{5.1.22}$$

$$\Delta\dot{\Psi}_2 = -\frac{I_2}{C} = \Delta\Psi_1 \frac{1}{RC} - \Delta\Psi_2 \frac{1}{RC} - \frac{\Phi_1}{RC} \tag{5.1.23}$$

With these informations, the system can be solved by substituting the variables, but the matrix form permits to extract useful informations and it can be applied subsequently to more complex solutions.

$$\dot{\begin{pmatrix}\Delta\Psi_1\\ \Delta\Psi_2\end{pmatrix}} = -\frac{1}{2RC}\begin{pmatrix}1+\frac{H}{L} & -1\\ -2 & 2\end{pmatrix}\begin{pmatrix}\Delta\Psi_1\\ \Delta\Psi_2\end{pmatrix} - \frac{\Phi_1}{2RC}\begin{pmatrix}0\\ 2\end{pmatrix} \tag{5.1.24}$$

Where the 0 in the last matrix comes from the fact that

$$\frac{\Phi_0}{2\Omega C} = \frac{\Phi_1}{2RC}\,,$$

because the resistances R and Ω are proportional respectively to H and $2L$ as are the voltages Φ_0 and Φ_1.

This set of equation can be written in state space form as $\dot{X} = Y - MX$ with

$$X \equiv \begin{pmatrix}\Delta\Psi_1\\ \Delta\Psi_2\end{pmatrix},\ Y \equiv -\frac{\Phi_1}{2RC}\begin{pmatrix}0\\ 2\end{pmatrix},\ M \equiv \frac{1}{2RC}\begin{pmatrix}1+\frac{H}{L} & -1\\ -2 & 2\end{pmatrix} \equiv UDU^{-1} \tag{5.1.25}$$

with $UU^{-1} = U^{-1}U = 1$ and $D = \frac{1}{2RC}\begin{pmatrix}\lambda_1 & 0\\ 0 & \lambda_2\end{pmatrix}$.

U is composed by the orthonormal eigenvectors of M, with eigenvalues $\lambda_1\ ,\ \lambda_2$.

The complete solution should consider an initial condition in which the capacitors are charged with the charge calculated in phase i, but this precaution complicates the calculation, without changing the time constants and the final values of the system. For this reason the equations will be solved considering an initial state in which the capacitors are not charged: $X(t=0) = 0$. To find the formal solution to the problem in equation (5.1.24), it is sufficient to find

$$X(t) = U\begin{pmatrix}[1-e^{-\frac{\lambda_1 t}{2RC}}]\frac{1}{\lambda_1} & 0\\ 0 & [1-e^{-\frac{\lambda_2 t}{2RC}}]\frac{1}{\lambda_2}\end{pmatrix}U^{-1}Y \tag{5.1.26}$$

because $U^{-1}\dot{X}(t) = U^{-1}Y - DU^{-1}X(t)$ is solved by $U^{-1}X(t) = e^{-Dt}a + D^{-1}U^{-1}Y$ with the constant a, fixed by the boundary condition $U^{-1}X(t=0) = 0$, to be $a = -D^{-1}U^{-1}Y$.

The time constant of the overall system is determined by the lower eigenvalues of M, which provides the higher characteristic time of the transitory. When the data of the simulation are chosen, so $H = 1/3 \cdot L$, the eigenvalues can be found:

$$\lambda_1 = 3.12\ ,\ \lambda_2 = 0.213\ .$$

Selecting λ_2 because it is the lower one, the time constant is obtained to be

$$\tau = \frac{2RC}{\lambda_2} = 9.38\frac{H}{D\kappa}\ .$$

The following steady-state values are so found:

$$\Delta\Psi_1 = -\frac{\Phi_0}{2} = -\frac{3}{8}S_e\Delta T\ ,\ \Delta\Psi_2 = -\frac{\Phi_0}{2} - \Phi_1 = -\frac{1}{2}S_e\Delta T$$

as expected from the simulations. The final charges accumulated must be explicitly stated because they are the ones conserved in phase iii:

$$Q_1 = 2C\Delta\Psi_1 = -C\Phi_0 = -\frac{3}{4}CS_e\Delta T\ ,\ Q_2 = -C\left(\frac{\Phi_0}{2} + \Phi_1\right) = -\frac{1}{2}CS_e\Delta T$$

Note how the charge in the second electrode is the same as the one found for the planar-electrodes case at the end of phase ii. This means that the presence of other electrodes, so other pores, only improves the final capacitance of the system, as it is known to happen for an externally charged supercapacitor.

Phase iii

The phase iii analysis is now trivial: first, the conservation of the charges is imposed

$$Q_1(phase\,ii) + Q_2(phase\,ii) = Q_1(phase\,iii) + Q_2(phase\,iii) = -C\left(\frac{3}{2}\Phi_0 + \Phi_1\right) \quad (5.1.27)$$

then, the new charges will distribute according to their capacitance:

$$Q_1 = -C\left(\Phi_0 + \frac{2}{3}\Phi_1\right) = -\frac{5}{6}CS_e\Delta T \quad (5.1.28)$$

$$Q_2 = -C\left(\frac{\Phi_0}{2} + \frac{\Phi_1}{3}\right) = -\frac{5}{12}CS_e\Delta T \quad (5.1.29)$$

The time constants of phase iii will be equal to the one of phase i because the circuit representing the equilibration is the same representing the phase i charge. Looking now at the potential measured at the electrodes at the end of phase iii, a circuit analysis reveals it to be

$$\Delta V = -\Phi_0 - \frac{2}{3}\Phi_1 = -\frac{5}{6}S_e\Delta T \quad (5.1.30)$$

exactly equal and opposite to the one of the phase i.

5.1.3 Dynamics

Having now found both the numerical results and the EEC solutions for the two-electrodes set-up, a comparison it is necessary. In this case, the dynamic behaviour of both phases i and ii are described by the EEC so the results can be analysed. Another difference with respect to the planar electrode condition is that the time constants for the phases i and ii are proportional to $H/D\kappa$ that is much greater than the $1/D\kappa^2$ found in the precedent case. This means that the characteristic times related to the heat equation τ_T are comparable to the time constants of the phases i and ii.

Phase i

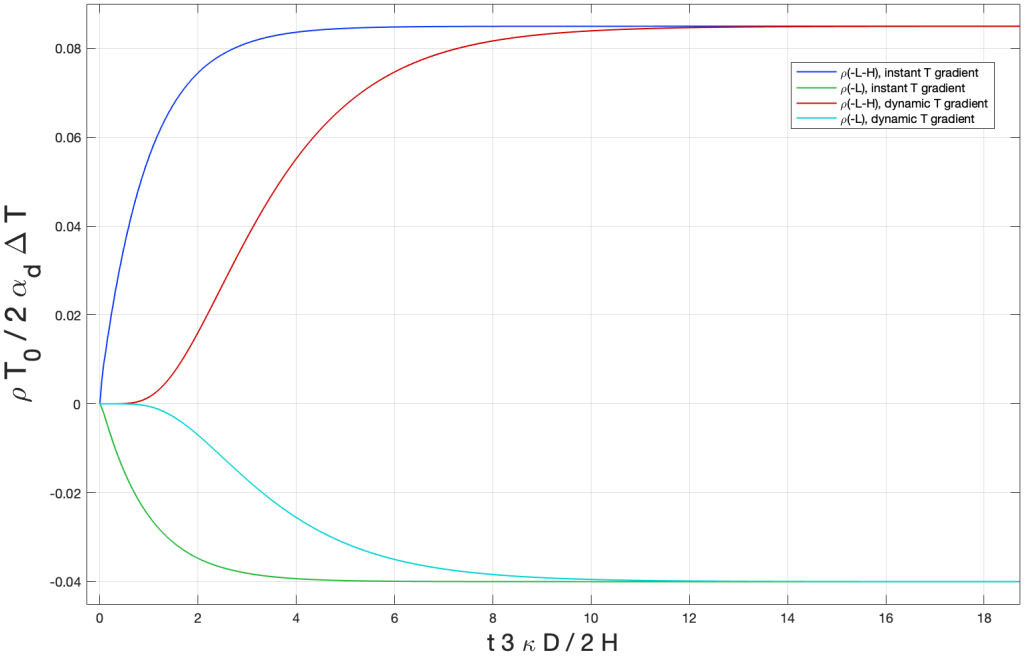

Figure 5.9: Numerical results for the dimensionless charge density $\rho T_0/2\alpha_d\Delta T$ for the first $(-L)$ and the second $(-L-H)$ electrode vs the dimensionless time $t3\kappa D/2H$, during the phase i transitory.

Starting analysing the phase i dynamics of the charge density at the electrodes (fig. 5.9), it is possible to demonstrate numerically that in this case, the temperature-time is of the order of the charge density time, providing a similar solution in the cases of instant temperature gradient and dynamic temperature gradient. For the instantaneous temperature gradient solution it is clearly visible how the charge density perfectly follows the time constant found in the equivalent electrical circuit, taking 5 times $2H/3\kappa D$ to complete the transitory. Regarding the case for a time-dependent heat equation, the precise time constant of the temperature is, using the parameters of the simulation, $\tau_T = 1,60 \cdot 2H/(3\kappa D)$, which explains why the difference is small.

Looking at the surface charge in figure 5.10 it is clear how the dynamics is the same as the charge density one.

In this case, it is also possible to make a comparison between the numerical values and the EEC results. In the circuit representation, the potential generators are immediately turned on, and so the solution of the EEC must be compared to the instant temperature gradient case. The accordance between the EEC and the numerical solution is clear for both the dynamics and the steady-state values, considering also that the surface charge is calculated deriving the potential slope which adds numerical errors.

From the comparison between the charge density and the surface charge, it is more clear the role of the Soret effect on the ions that creates a charge unbalance.

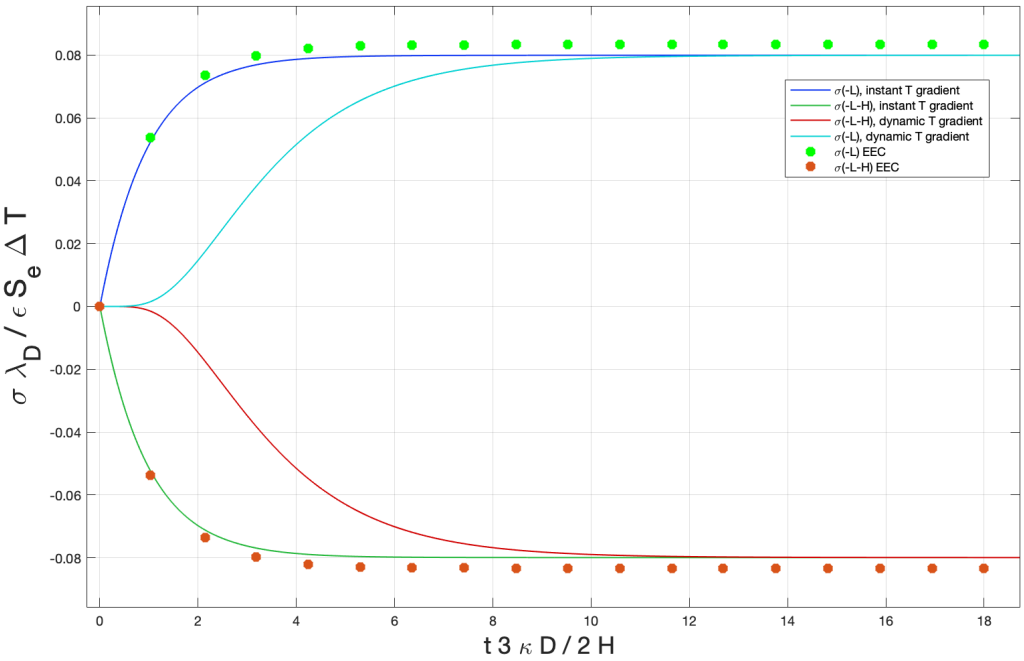

Figure 5.10: Numerical results (solid lines) and equivalent electrical circuit (dots) for the dimensionless surface charge $\sigma\lambda_D/\varepsilon S_e\Delta T$ for the first $(-L)$ and the second $(-L-H)$ electrode, vs the dimensionless time $t3\kappa D/2H$, during the phase i transitory.

Phase ii

The comparison of the phase ii could be done with two different initial conditions: using the results of phase i as starting point or letting the system evolve from a completely discharged state. The second option was chosen for various reasons: first, the FEM simulation program used is not optimized for multi-steps solution in which the boundary conditions changes, leading to a better simulation if all the phases are simulated separately; second, the EEC analytical solution was found from the discharge state for the reasons mentioned above. It is also known that the time constants and the final values are independent from the initial conditions, so the accuracy of the analysis holds for every initial state chosen. Moreover, the supercapacitor can be in principle charged directly in close circuit reproducing the conditions used in this simulation, making this choice also physically valid.

The simulation is also done only for the instantaneous temperature gradient case because the gradient builds up in phase i and it is simple to calculate how the much longer characteristic times of phase ii make negligible the temperature needed to establish the gradient.

The dynamics of the phase ii charge density is well described, as it is possible to see in figure 5.11, and it is well fitted by the EEC time found of $9.38H/D\kappa$.

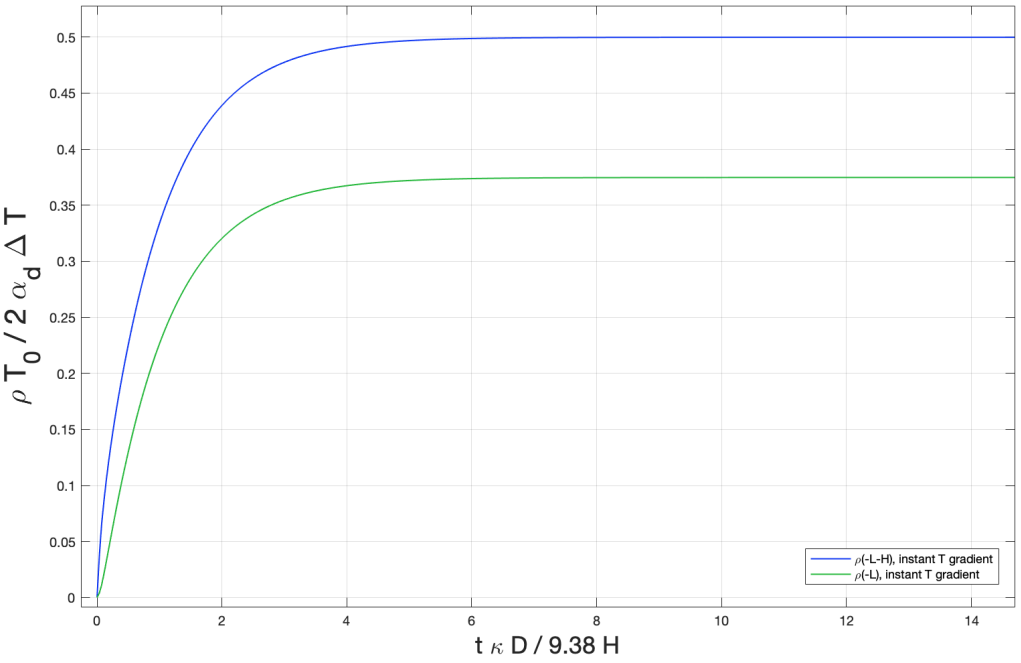

Figure 5.11: Numerical results for the dimensionless charge density $\rho T_0/2\alpha_d\Delta T$ for the first $(-L)$ and the second $(-L-H)$ electrode vs the dimensionless time $t\kappa D/9.38H$, during the phase ii transitory.

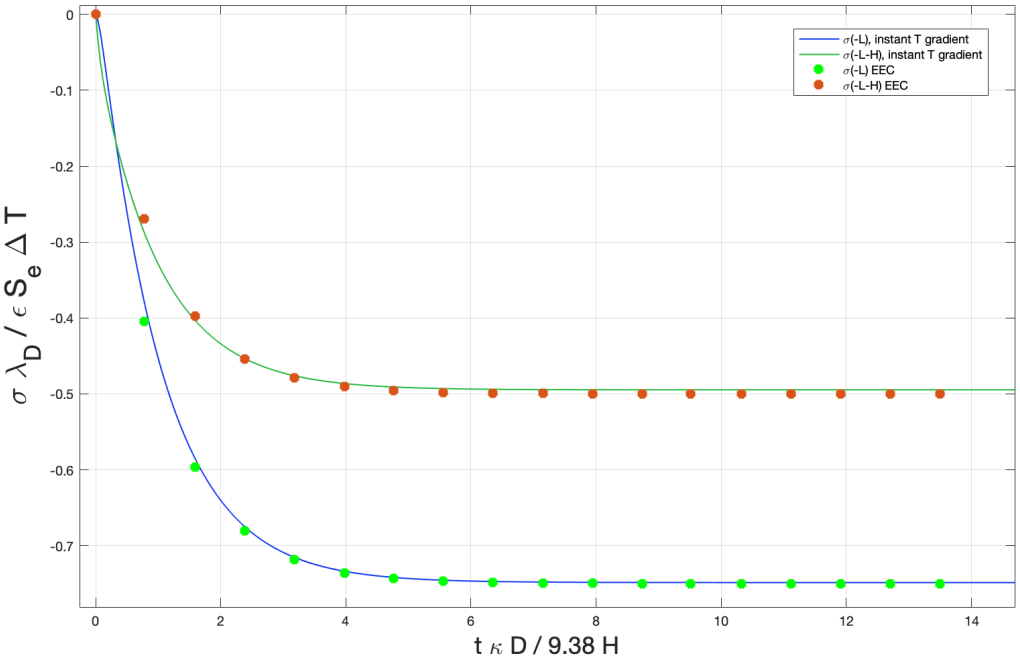

Figure 5.12: Numerical results (solid lines) and equivalent electrical circuit (dots) for the dimensionless surface charge $\sigma\lambda_D/\varepsilon S_e\Delta T$ for the first $(-L)$ and the second $(-L-H)$ electrode vs the dimensionless time $t\kappa D/9.38H$, during the phase ii transitory.

No particular surprise comes from this simulation, the two charge densities grow,

remaining different due to the Soret effect that acts on the ions.

To complete the phase ii analysis a comparison between the surface charge of EEC solution and the numerical results is made in figure 5.12. The two graphs can be perfectly superimposed, confirming the utility of the EEC.

Even if the steady-state results made clear the asymmetries between the electrodes in phase ii, the image of the surface charges makes clearer the particular charging behaviour of a thermally charged supercapacitor. In fact, usually all the electrodes charge with the same amount of surface charge, once the potential is imposed. In this case, it is clearly visible how instead the Soret effect unbalances the surface charges making it imprecise to consider the total capacity of the cell as the sum of the capacity of the pores. This is especially true in the case of a high number of electrodes, as it will be seen in the next section.

Complete cycle

The development of the EEC permits also to diversify the software utilization, so that Simulink® can be used to solve very rapidly all the cycle, including phases iii and iv, thanks to the possibility to virtually open and close circuits.

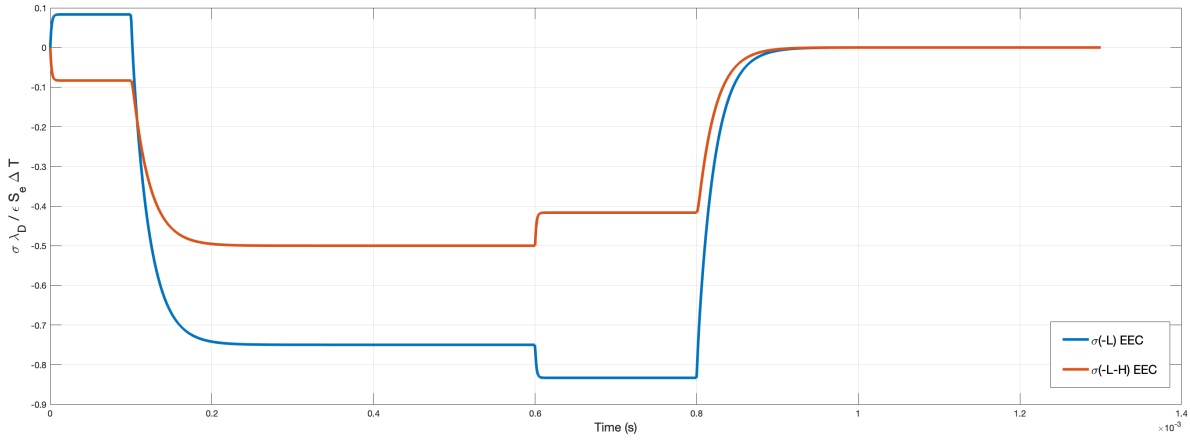

Figure 5.13: Equivalent electrical circuit results for the dimensionless surface charge $\sigma\lambda_D/\varepsilon S_e \Delta T$ of the electrodes vs time (s). The entire charging and discharging cycle is represented.

The figure 5.13 shows a picture of the overall cycle, from the point of view of the surface charge of the electrodes. The four phases are clearly visible, as it is the big difference in characteristic times between the charging and discharging steps (phase ii and iv respectively) and the intermediate steps (phase i and iii).

It is also clearly visible the different behaviours between the charging phase under temperature gradient, which shifts the curves, and the discharging phase in an isothermal system, in which the curves almost superimpose.

To validate further the model it is useful to evaluate the potential difference that could be experimentally measured if a voltmeter is connected at the two sides of the capacitor.

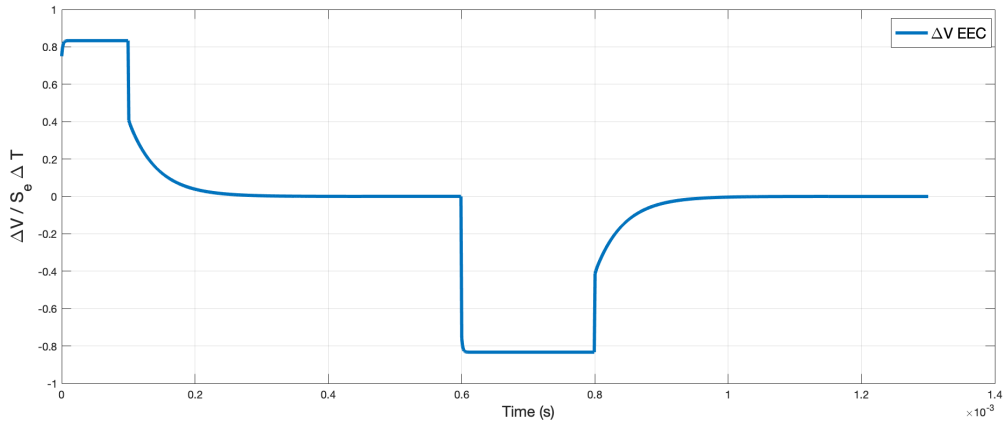

Figure 5.14: Equivalent electrical circuit results for the dimensionless potential difference between the nths electrodes $\Delta V/S_e\Delta T$ vs time (s). The entire charging and discharging cycle is represented.

To observe the dynamics it is necessary to insert a resistance in the upper circuit, that connects the two electrodes. A resistance of the same value of Ω was inserted in the simulated circuit, and the results for the overall cycle are exposed in figure 5.14.

The figure resembles the experiments found in literature, confirming that the method used is capable of model a real system. Of course, the presence of only two electrodes makes the system still far from a real supercapacitor, but the route towards a complete model is clear and it is now just sufficient to expand it to higher numbers of electrodes.

5.2 Advance System: n-Electrodes Solution

Having posed all the physical and mathematical bases in the two-electrodes solution, the next step is to expand the solution for arbitrary n electrodes. The electrodes will be positioned at a distance $h = H/(n-1)$ so that the first electrode ($i = 1$) is posed at $X_1 = \pm L$, the ith electrode is posed at $X_i = \pm L \pm h(i-1)$ and the outer electrode in contact with the electrolyte only on one side is at $X_n = \pm L \pm h(n-1) = \pm L \pm H$.

The boundary conditions for the temperature and the ions limits are the same as before:

$$T(-X_n, t) = T_0 \, , \; T(+X_n, t \geq 0) = T_0 + \Delta T \tag{5.2.1}$$

$$n_{\pm}(x, t < 0) = n_0 \tag{5.2.2}$$

$$j_{\pm}(\pm X_n, t) = 0 \tag{5.2.3}$$

where ΔT is present only in the phases i and ii.

Moreover, the electrical boundary conditions for the various phases are:
Phase i

$$\sum_{i=1}^{n} \sigma_i = 0 \, , \tag{5.2.4}$$

$$\phi_1(\pm X_1, t) = \phi_2(\pm X_2, t) = ... = \phi_i(\pm X_i, t) = ... = \phi_n(\pm X_n, t) \tag{5.2.5}$$

Phase ii

$$\phi_1(\pm X_1, t) = \phi_2(\pm X_2, t) = ... = \phi_i(\pm X_i, t) = ... = \phi_n(\pm X_n, t) = 0 \tag{5.2.6}$$

Phase iii

$$\sum_{i=1}^{n} \sigma_{i,\, phase\ ii} = \sum_{i=1}^{n} \sigma_{i,\, phase\ iii} \, , \tag{5.2.7}$$

$$\phi_1(\pm X_1, t) = \phi_2(\pm X_2, t) = ... = \phi_i(\pm X_i, t) = ... = \phi_n(\pm X_n, t) \tag{5.2.8}$$

5.2.1 Numerical Results

As previously stated the analytical solution for the linearised problem can be found for every n chosen, but it results too complicated to get physical information from it, so the task will be carried out by the numerical simulations.

The parameters chosen in the simulation are the same as for the two-electrodes case, with the exceptions of $n = 5$ so that the effects that multiples electrodes create are present, but the computational time remains similar. Moreover, the lengths are modified: $H = 60\lambda_D$ and $L = 180\lambda_D$, this choice was made in order to preserve the H/L ratio having simultaneously a big enough pore length h to let the EDLs be fully developed. This is

important because the theory constructed so far is valid only if the specific capacitance is approximable with ε/λ_D.

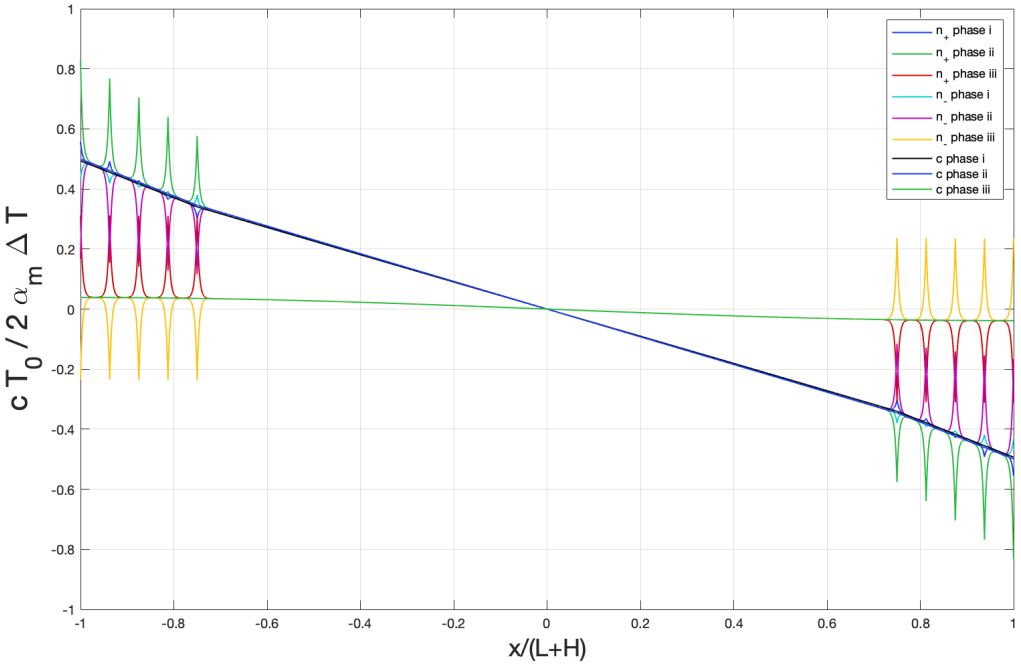

Figure 5.15: Numerical solutions of the dimensionless neutral density $cT_0/2\alpha_m\Delta T$ vs the dimensionless length $x/(L+H)$. The ions' distributions are also represented in the graph.

Starting analysing the c variable graph in the various phases in figure 5.15, comes with no surprise that it is the same as in the previous cases because the neutral charge is not affected by the presence of the electrodes. Of course, the single ions distributions have now peaks in correspondence of the five electrodes.

The charge density behaviour, that can be seen in 5.16, is fairly predictable. The phase i plot is an extension of the two-electrodes results, in which the charge density is shifted towards the outer electrode by the Seebeck effect present in the pores. Regarding the phase ii ρ profile, it confirms the superposition of the effects: it is clear how it is composed by the Seebeck shift and the normal stack charged electrodes plot, visible in phase iii. The maximum value is again $\alpha_d\Delta T/T_0$ (the dimensionless charge density plotted touches 0.5 in the graph) confirming that the presence of other electrodes only adds maximum capacitance for the thermally chargeable supercapacitor.

The potential in figure 5.17 conserves its shape and slope, with local maximum and minimum in correspondence respectively of negative and positive charge density at the electrodes. We can assume this behaviour will be conserved for every number n of electrodes.

It is possible to observe that some characteristics of the two electrodes results are conserved. In particular, the value of the potential in phase i at the nth electrode is the same, as it is the peak value of the potential in second phase near the nth electrode.

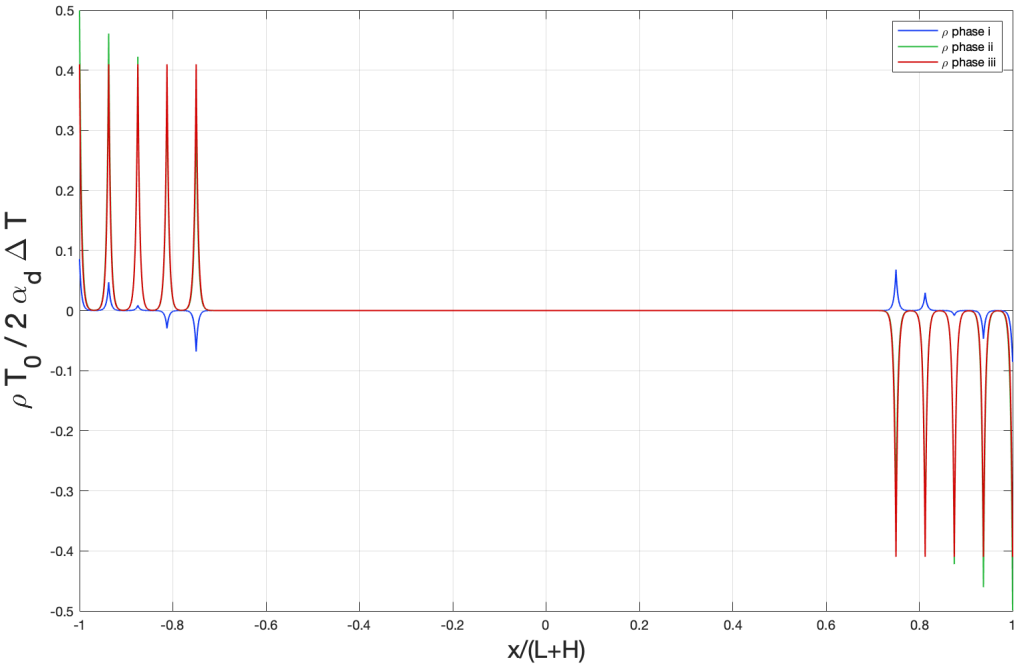

Figure 5.16: Numerical solutions of the dimensionless charge density $\rho T_0/2\alpha_d\Delta T$ vs the dimensionless length $x/(L+H)$.

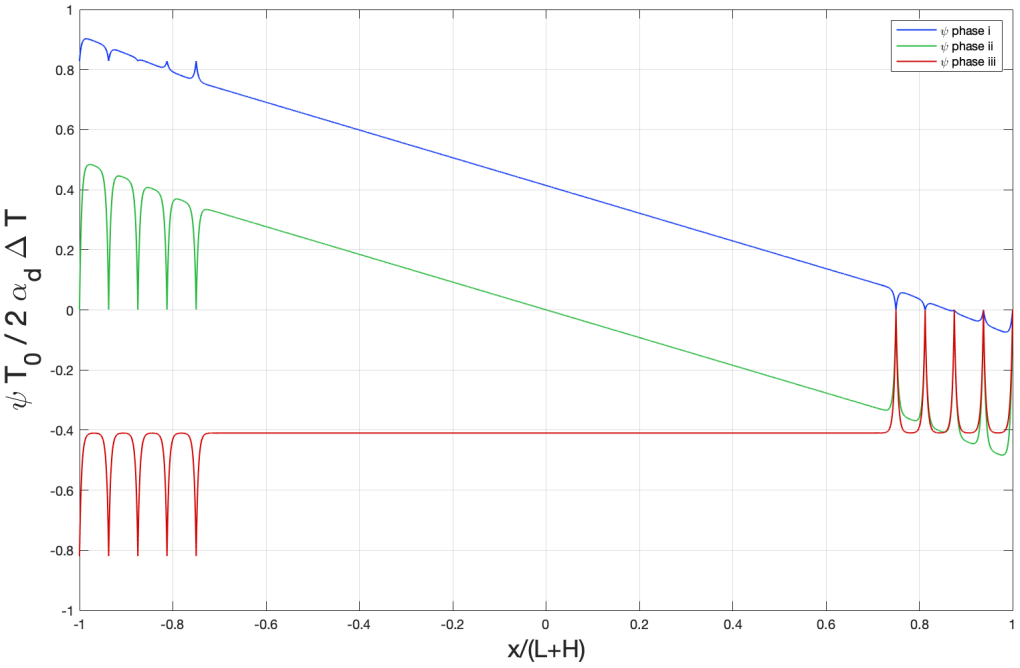

Figure 5.17: Numerical results of the dimensionless potential $\psi T_0/2\alpha_d\Delta T$ vs the dimensionless length $x/(L+H)$.

5.2.2 Equivalent Electrical Circuit

In order to finally complete the model and to be able to predict the outcomes for a broad range of parameters, such as temperature differences, various lengths and high number of electrodes, it is necessary a complete calculation of a circuit with n capacitors per side.

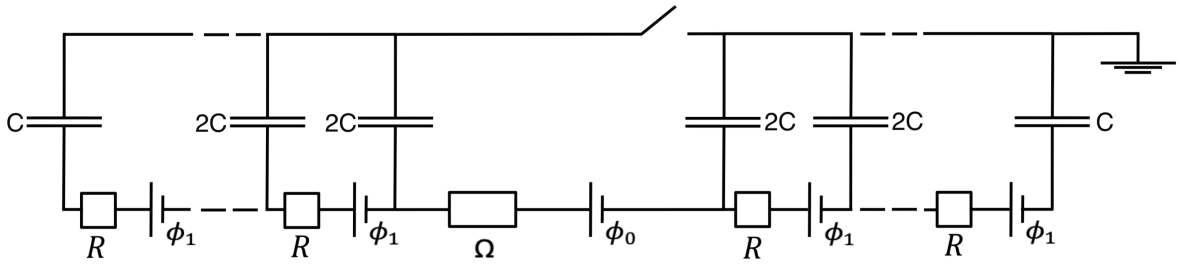

Figure 5.18: Equivalent electrical circuit for the n-electrodes case, the dashed lines represent the numerous electrodes present between the first and the nth one.

The setup is the same as the two electrodes case, but here we have $n-1$ electrodes per side with capacitance $2C$ and the outer nth with capacitance C. Moreover $n-1$ potential generator Φ_1 are present, coupled with $n-1$ resistor of value R.

The values of the generators and the resistances are proportional to h so that:

$$\Phi_1 = S_e \frac{\Delta T}{2(L+H)} h = S_e \frac{\Delta T}{2(L+H)} \frac{H}{n-1} \tag{5.2.9}$$

$$R = \frac{h}{2\sigma_{el}} = \frac{H}{2(n-1)\sigma_{el}} \tag{5.2.10}$$

Obtaining and RC time that is now

$$RC = \frac{H}{(n-1)\kappa D} \tag{5.2.11}$$

Again $\Delta\Psi_i$ stands for the voltage over the capacitor i, Q_i for the charge on the same capacitor and I_i for the current through it. The reservoir part of the circuit is again defined with Φ_0 for the generator, Ω for the resistance and I_0 for the current through it.

The charges are so defined as

$$Q_1(t) = 2C\Delta\Psi_1(t) \tag{5.2.12}$$

...

$$Q_i(t) = 2C\Delta\Psi_i(t) : 2 \leq i \leq n-1 \tag{5.2.13}$$

...

$$Q_{n-1}(t) = 2C\Delta\Psi_{n-1}(t) \tag{5.2.14}$$

$$Q_n(t) = C\Delta\Psi_n(t) \tag{5.2.15}$$

Phase i

Regarding the currents, a distinction must be made between phase i and ii. In phase i, the open circuit condition implies that the current I_1 coming from the charge of the capacitor $i = 1$ flows in the resistance$R$ from the inner to the outer side. The direction of the current flowing in the $= 1$ capacitor is so inverse respect to the currents flowing in the others so that the currents are defined in the following way:

$$I_1 = 2C\Delta\dot{\Psi}_1 \tag{5.2.16}$$

...

$$I_i = -2C\Delta\dot{\Psi}_i : 2 \leq i \leq n-1 \tag{5.2.17}$$

...

$$I_n = -C\Delta\dot{\Psi}_n \tag{5.2.18}$$

The conservation of charges is also imposed in phase i:

$$\sum_{i=1}^{n} Q_i(t) = 0 \tag{5.2.19}$$

from the point of view of the currents this condition implies that the current flowing in the second resistance is $I_1 - I_2$, the one flowing in the ith resistance is $I_1 - I_2 - ... - I_i$ and the current flowing in the last resistance (remembering there are $n-1$ total resistances) is $I_1 - ...I_i - ...I_{n-1} = I_n$.
Using now the Kirchhoff's laws in the various meshes the following system of equations is obtained:

$$RI_1 = -\Delta\Psi_1 + \Delta\Psi_2 + \Phi_1 \tag{5.2.20}$$

$$R(I_1 - I_2) = -\Delta\Psi_2 + \Delta\Psi_3 + \Phi_1 \tag{5.2.21}$$

...

$$R(I_1 - I_2 - ... - I_i) = -\Delta\Psi_i + \Delta\Psi_{i+1} + \Phi_1 : 3 \leq i \leq n-1 \tag{5.2.22}$$

...

$$R(I_1 - I_2 - ... - I_{n-1}) = RI_n = -\Delta\Psi_{n-1} + \Delta\Psi_n + Phi_1 \tag{5.2.23}$$

Using now the definitions of current the system can be rephrased as

$$\Delta\dot{\Psi}_1(t) = \frac{I_1}{2C} = -\frac{\Delta\Psi_1 - \Delta\Psi_2 - \Phi_1}{2RC} \tag{5.2.24}$$

$$\Delta\dot{\Psi}_2(t) = -\frac{I_2}{2C} = -\frac{-\Delta\Psi_1 + 2\Delta\Psi_2 - \Delta\Psi_3}{2RC} \tag{5.2.25}$$

...

$$\Delta\dot{\Psi}_i(t) = -\frac{I_i}{2C} = -\frac{-\Delta\Psi_{i-1} + 2\Delta\Psi_i - \Delta\Psi_{i+1}}{2RC} : 3 \leq i \leq n-1 \tag{5.2.26}$$

...

$$\Delta\dot{\Psi}_{n-1}(t) = -\frac{I_{n-1}}{2C} = -\frac{-\Delta\Psi_{n-2} + 2\Delta\Psi_{n-1} - \Delta\Psi_n}{2RC} \tag{5.2.27}$$

$$\Delta\dot{\Psi}_n(t) = -\frac{I_n}{C} = -\frac{-\Delta\Psi_{n-1} + \Delta\Psi_n + \Phi_1}{RC} \tag{5.2.28}$$

The system can be posed in matrix form:

$$\begin{pmatrix} \Delta\dot{\Psi}_1 \\ \Delta\dot{\Psi}_2 \\ \vdots \\ \Delta\dot{\Psi}_i \\ \vdots \\ \Delta\dot{\Psi}_n \end{pmatrix} = -\frac{1}{2RC} \cdot \begin{pmatrix} 1 & -1 & & & & & \\ -1 & 2 & -1 & & & & \\ & -1 & \ddots & \ddots & & & \\ & & & \ddots & \ddots & & \\ & & & & -1 & 2 & -1 \\ & & & & & -2 & 2 \end{pmatrix} \cdot \begin{pmatrix} \Delta\Psi_1 \\ \Delta\Psi_2 \\ \vdots \\ \Delta\Psi_i \\ \vdots \\ \Delta\Psi_n \end{pmatrix} - \frac{\Phi_1}{2RC} \cdot \begin{pmatrix} -1 \\ 0 \\ \vdots \\ \vdots \\ 0 \\ 2 \end{pmatrix} \tag{5.2.29}$$

The system written above is not made of independent equations because the presence of the charge conservation (eq. 5.2.19) makes the nth equation linearly dependent on the others. The matrices written are instead useful for a comparison with the phase ii solution because the same form is maintained. In order to be able to solve the system for every n number of equations, it is better to rewrite it as an independent set. To do this it is necessary to use equation (5.2.19), rephrased as $\Delta\Psi_n = -2\sum_{i=1}^{n-1}\Delta\Psi_i$ and substitute it in equation (5.2.27) obtaining

$$\Delta\dot{\Psi}_{n-1} = -\frac{2\sum_{i=1}^{n-3}\Delta\Psi_i + \Delta\Psi_{n-2} + 4\Delta\Psi_{n-1}}{2RC} \tag{5.2.30}$$

So that an independent set of $n-1$ equations with $n-1$ variables is found and written in the form $\dot{X} = Y - MX$ with

$$X \equiv \begin{pmatrix} \Delta\Psi_1 \\ \Delta\Psi_2 \\ \vdots \\ \Delta\Psi_i \\ \vdots \\ \Delta\Psi_{n-1} \end{pmatrix}, \; Y \equiv -\frac{\Phi_1}{2RC} \cdot \begin{pmatrix} -1 \\ 0 \\ \vdots \\ \vdots \\ \vdots \\ 0 \end{pmatrix}, \; M \equiv \frac{1}{2RC} \begin{pmatrix} 1 & -1 & & & & & \\ -1 & 2 & -1 & & & & \\ & -1 & \ddots & \ddots & & & \\ & & & \ddots & \ddots & & \\ & & & & -1 & 2 & -1 \\ 2 & 2 & ... & 2 & ... & 1 & 4 \end{pmatrix} \tag{5.2.31}$$

The value of $\Delta\Psi_n$ will be calculated consequently. Notice how the matrix M depends only on R, C and the number of electrodes n, without being affected by the H/L ratio.

The matrix form permits us to use the same method used in the two electrode case (eq. 5.1.26) expandened to $n-1$ equations. The solution therefore is:

$$X(t) = U(1 - e^{-Dt})D^{-1}U^{-1}Y \tag{5.2.32}$$

with

$$1 - e^{-Dt} = 1 - \begin{pmatrix} e^{-\frac{t\lambda_1}{2RC}} & & \\ & \ddots & \\ & & e^{-\frac{t\lambda_n}{2RC}} \end{pmatrix} \tag{5.2.33}$$

where λ_i are the eigenvalues of the matrix M.

To find the time constant as a function of n, the eigenvalues where found numerically from $n = 3$ to $n = 100$. After selecting the smallest eigenvalue $\lambda_- = min\{\lambda_1, ..., \lambda_n\}$, the characteristic time of the system is known to be $\tau_n = 2RC/\lambda_-$. Remembering that i this case $RC = h\lambda_D/D = H\lambda_D/D(n-1)$, it is convenient to plot $1/\lambda_- \cdot 1/(n-1)$ for every n.

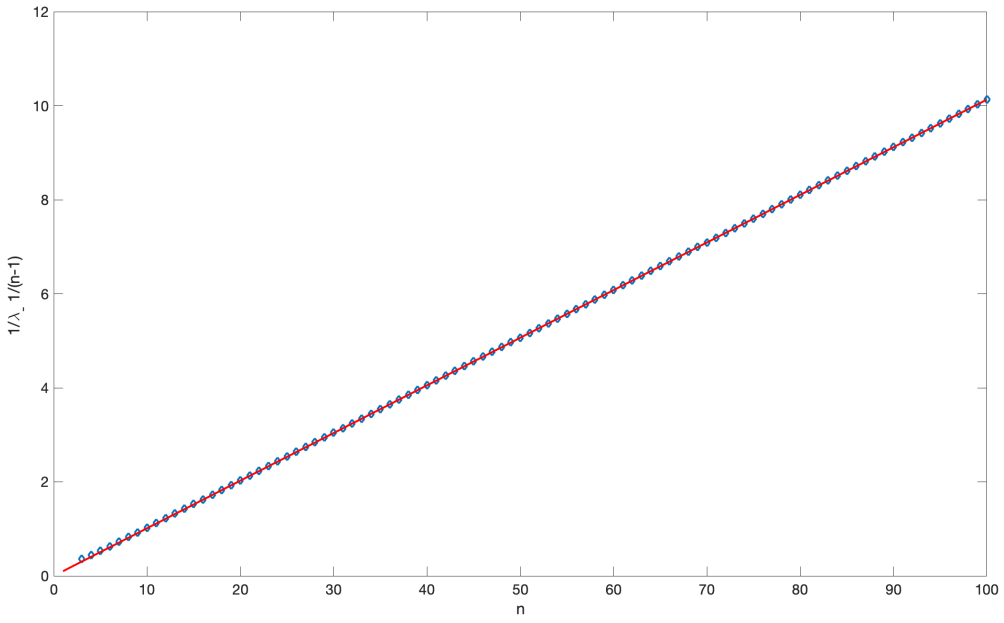

Figure 5.19: $1/\lambda_- \cdot 1/(n-1)$ *vs the number of electrode n (blue diamonds), with the interpolating line (red line).*

So that graphically we can see how

$$1/\lambda_- \cdot 1/(n-1) \simeq 0.1013n \tag{5.2.34}$$

Obtaining now the characteristic time for the phase i $\tau_{n,i}$, as

$$\tau_{n,i} = 2\frac{H\lambda_D}{D}\frac{1}{\lambda_-}\frac{1}{n-1} \tag{5.2.35}$$

That, using the relation (5.2.34), permits to obtain the time constant of the phase i for every number of electrodes:

$$\tau_{n,i} = \frac{H\lambda_D}{D}\cdot 0.2026\cdot n \tag{5.2.36}$$

To obtain the steady-state solution, instead of calculating the complete solution for every n, it is simpler to analyse directly the circuit in the final state in which the capacitors are considered as open circuits and no current is flowing. This simplifies the calculation and, summed with the time constant found, permits to have a clear view of the behaviour of the supercapacitor.

Unfortunately a unique solution, that correlates the geometrical parameters and the number of electrodes to the various charges accumulated in the electrodes, cannot be found. In order to verify the accuracy of the solution, the values of the charges are calculated for $n = 5$ and compared with the results of the simulation. So that, selecting for example the first and the last electrode,

$$Q_1 = 2C\Delta\Psi_1 = 2C\frac{16}{9}\Phi_1 = \frac{32}{9}C\Phi_1\,, \tag{5.2.37}$$

$$Q_5 = C\Delta\Psi_5 = -\frac{20}{9}C\Phi_1\,, \tag{5.2.38}$$

that with the simulation parameters becomes

$$Q_1 = 0.111\,CS_e\Delta T\,, \tag{5.2.39}$$

$$Q_5 = 0.0694\,CS_e\Delta T\,, \tag{5.2.40}$$

which, as it will be seen, is relatively close to the numerical results. The experimentally measurable potential difference is instead

$$\Delta V = \Phi_0 + 4\Phi_1 + \Delta\Psi_5 = \Phi_0 + \Delta\Psi_1 = \Phi_0 + \frac{16}{9}\Phi_1\,, \tag{5.2.41}$$

which, again, applying the definitions of the voltage generators, becomes

$$\Delta V = 0.805 S_e\Delta T \tag{5.2.42}$$

coinciding almost perfectly to the value of the phase i simulation.

Phase ii

The solution for the second phase is similar to the phase ii solution of the two-electrodes system. As in that case, all the currents passing through the capacitors are now pointing upwards so that the currents can be easily defined as

$$I_i = -2C\Delta\dot{\Psi}_i : 1 \leq i \leq n-1 \tag{5.2.43}$$

$$I_n = -C\Delta\dot{\Psi}_n \tag{5.2.44}$$

The Kirchhoff's laws are applied considering, this time, the central mesh: the current passing trough Ω is called again I_0 so that the current through the first resistor R is $I_0 - I_1$ up to the last that is $I_0 - I_1 - ... - I_i - ... - I_{n-1} = I_n$. The mash laws are now:

$$\Omega I_0 = 2\Delta\Psi_1 + \Phi_0 \tag{5.2.45}$$

$$R(I_0 - I_1) = -\Delta\Psi_1 + \Delta\Psi_2 + \Phi_1 \tag{5.2.46}$$

...

$$R(I_0 - I_1 - ... - I_i) = -\Delta\Psi_i + \Delta\Psi_{i+1} + \Phi_1 : 2 \leq i \leq n-1 \tag{5.2.47}$$

...

$$RI_n = -\Delta\Psi_{n-1} + \Delta\Psi_n + \Phi_1 \tag{5.2.48}$$

Combining the above equations with eq. (5.2.43) and eq. (5.2.44), n coupled differential equations are obtained:

$$\Delta\dot{\Psi}_1 = -\frac{I_1}{2C} = -\left(\frac{1}{\Omega C} + \frac{1}{2RC}\right)\Delta\Psi_1 + \frac{1}{2RC}\Delta\Psi_2 - \frac{\Phi_0}{2RC} + \frac{\Phi_1}{2RC} \tag{5.2.49}$$

...

$$\Delta\dot{\Psi}_i = -\frac{I_2}{2C} = -\frac{-\Delta\Psi_{i-1} + 2\Delta\Psi_i - \Delta\Psi_{i+1}}{2RC} : 2 \leq i \leq n-1 \tag{5.2.50}$$

...

$$\Delta\dot{\Psi}_n = -\frac{I_n}{C} = -\frac{-\Delta\Psi_{n-1} + \Delta\Psi_n + \Delta\Phi_1}{RC} \tag{5.2.51}$$

Written in matrix form as

$$\begin{pmatrix} \dot{} \\ \Delta\Psi_1 \\ \Delta\Psi_2 \\ \vdots \\ \Delta\Psi_i \\ \vdots \\ \Delta\Psi_n \end{pmatrix} = -\frac{1}{2RC} \cdot \begin{pmatrix} 1 + \frac{H}{L(n-1)} & -1 & & & & & & \\ -1 & 2 & -1 & & & & & \\ & -1 & \ddots & \ddots & & & & \\ & & & \ddots & \ddots & -1 & & \\ & & & & -1 & 2 & -1 & \\ & & & & & -2 & 2 & \end{pmatrix} \cdot \begin{pmatrix} \Delta\Psi_1 \\ \Delta\Psi_2 \\ \vdots \\ \Delta\Psi_i \\ \vdots \\ \Delta\Psi_n \end{pmatrix} - \frac{\Phi_1}{2RC} \cdot \begin{pmatrix} 0 \\ 0 \\ \vdots \\ \vdots \\ 0 \\ 2 \end{pmatrix} \tag{5.2.52}$$

In which the terms $\frac{\Phi_0}{2RC}$ and $\frac{\Phi_1}{2RC}$ cancels again, the proportion between Ω and R is reflected in the top left term of the dynamic matrix with $H/L(n-1)$ and the other terms of that matrix are the same of the matrices of (5.2.29).

The solution method just used for the phase i can be applied to the system (5.2.52) founding numerically, for every n, H and L selected, the corresponding results.

Studying the matrix M to find the eigenvalues, hence the dynamics of the system, it is simply to observe the agreement with the matrix found by Lian and al. in the first development of the stack electrode model [40]. That matrix share the same scope as the matrix find in this work: describing the charging dynamics of a supercapacitor.

This is a demonstration of how a thermally charged supercapacitor has the same dynamic behaviour as an externally charged one.

In particular the work cited found a relation between the time constant and the geometrical variables of the system, that is still valid:

$$\tau_{n,ii} = \frac{L\lambda_D}{D} \cdot \left[\left(2 + 0.75\frac{H}{L} \right) n - 1 - 0.91\frac{H}{L} \right] \tag{5.2.53}$$

It was obtained finding numerically the smallest eigenvalues of M, $\lambda_- = min\{\lambda_1, ..., \lambda_n\}$, for various n, in order to find different $\tau_n = 2RC/\lambda_-$. Then, observing graphically that τ_n could be written as $\tau_n = L\lambda_D/D \cdot (f_1 + f_2 n)$, where f_1 and f_2 were obtained selecting different H/L and performing two least-squares fits.

It is also important to remember that, in general, $\tau_{n,ii}$ is not the actual time constant for all the electrodes, but it is the late time behaviour of them. In particular, the functions of the surface charge of the different electrodes will contain a sum of exponential decays terms of time constant $\tau_i = 2RC/\lambda_i$, with the slowest term $\tau_{n,ii}$, which guarantees the necessity of wait $\sim 5\tau_{n,ii}$ to have a complete charge.

As previously done, the capacitors are now considered as open circuit to calculate the steady-state solution. For the phase ii it is possible to obtain a general result:

$$\Delta\Psi_i = \frac{\Phi_0}{2} + (i-1)\Phi_1 = \frac{S_e \Delta T}{2(1+\frac{H}{L})} \left(1 + \frac{i-1}{n-1}\frac{H}{L} \right) : 1 \leq i \leq n \tag{5.2.54}$$

It is interesting to notice how for the nth electrode in phase ii the potential is independent on the geometry: $\Delta\Psi_n = S_e\Delta T/2$, confirming what was observed in the simulations.

From the notion of the potential differences, it is possible to calculate the total charge present in the left electrode:

$$Q_{left} = 2C \sum_{i=1}^{n-1} \Delta\Psi_i + C\Delta\Psi_n \tag{5.2.55}$$

substituting,

$$Q_{left} = C \left[\Phi_0 \left(n - \frac{1}{2} \right) + \Phi_1 (n-1)^2 \right] , \tag{5.2.56}$$

considering now the relation between Φ_0 and Φ_1 in the n electrode case,

$$\Phi_0 = \frac{2L(n-1)}{H}\Phi_1 :, \tag{5.2.57}$$

including the definition of Φ_0 (eq. 5.1.6), the total charge of the left electrode as function of the applied temperature difference and geometry of the system is obtained:

$$Q_{left} = \frac{CS_e\Delta T}{1+\frac{H}{L}}\left(n - \frac{1}{2} + \frac{H}{2L}(n-1)\right) \tag{5.2.58}$$

If the complete n electrode circuit is thought as composed by one equivalent capacitor per side, C_{left} and C_{right}, in which the voltage generator in the center apply a voltage equal to $S_e\Delta T$, the potential drop over the two capacitors will be $S_e\Delta T/2$. This permits to divide the total charge accumulated in an electrode by the potential drop across it to obtain the equivalent capacitance of the nanoporous electrode when a temperature gradient is present. Following this route, the left equivalent capacitance is obtained.

$$C_{left} = C\frac{1}{1+\frac{H}{L}}\left(2n - 1 + \frac{H}{L}(n-1)\right) \tag{5.2.59}$$

In the case of a real supercapacitor in which $n >> 1$ the total left equivalent capacitance is approximated as

$$C_{left} \simeq 2nC\frac{1+\frac{H}{2L}}{1+\frac{H}{L}} \tag{5.2.60}$$

This capacitance results quite different from the one of a supercapacitor charged by an external potential, that it $(2n-1)C + C$ which, for high h can be simply approximated as $2nC$.

In particular, in the case of $H/L >> 1$, the thermo-charged supercapacitor reveals a capacitance of nC, which is half the expected one. Conversely, in the case of thin electrodes $(H/L << 1)$ the capacitance is approximable to $2nC$, which is equal to the original one. Intuitively a large electrode will be affected more by the temperature difference inside it, so the actual capacitance will be diminished by a shift in the charge density distribution due to the Seebeck effect. The total capacitance of the two identical capacitors connected in series is simply half the single ones

$$C_{tot} = \frac{C_{left}}{2} = C\frac{1}{2\left(1+\frac{H}{L}\right)}\left(2n - 1 + \frac{H}{L}(n-1)\right) \tag{5.2.61}$$

The experiments are used to measure separately the internal resistance of the circuit and the capacitance and use then the RC value as time constant. For the case here presented the time constant and the total capacitance were found directly from the EEC so that it is is possible inversely to find the effective internal resistance as

$$R_{int} = \frac{\tau_{n,ii}}{C_{tot}} \simeq \Omega\left(1+\frac{H}{L}\right)\frac{2+0.75\frac{H}{L}}{2+\frac{H}{L}}, \tag{5.2.62}$$

where the equivalence $L\lambda_D/D = \Omega C/2$ was used and the approximation for $n >> 1$ was done. This effective internal resistance can be compared to the resistance that is ideally

calculated applying simply the definition of resistance at this geometry

$$R_{ideal} = \frac{L}{A\sigma_{el}}\left(1+\frac{H}{L}\right) = \Omega\left(1+\frac{H}{L}\right)\,, \tag{5.2.63}$$

noticing that a coefficient $(2+0.75H/L)/(2+H/L)$ appears in the effective resistance, showing how the presence of multiples electrodes slow down the dynamics with respect to the expected one.

These conclusions are far from being experimentally proven, but it could results interesting a thick electrodes supercapacitor which capacitance changes if thermally charged (instead of externally charged), but it preserves the same dynamic of an electrically charged one.

Phase iii

All the elements are now posed to calculate the phase iii behaviour of an n electrodes circuit. The fact that the circuit is again open, assure that the dynamic matrix M for phase i is valid to calculate the time dependence of phase iii, obtaining so the exact same time constants τ_n found in equation 5.2.36.

To find the steady state-values, it is sufficient to divide the total charge Q_{tot} by the total capacitance of the electrodes $2C(n-1)+C$ and multiply it by the single capacitance of the electrode i, so that the charge will be distributed in the electrodes according to the capacitance:

$$Q_i = \frac{Q_{tot}}{2C(n-1)+C}\cdot 2C : 1 \leq i \leq (n-1) \tag{5.2.64}$$

$$Q_n = \frac{Q_{tot}}{2C(n-1)+C}\cdot C \tag{5.2.65}$$

from this values the potential difference is readily found for every i:

$$\Delta\Psi_i = \frac{Q_{tot}}{(2n-1)C} = \frac{S_e\Delta T}{1+\frac{H}{L}}\frac{\left[n-\frac{1}{2}+\frac{H}{2L}(n-1)\right]}{2n-1} \tag{5.2.66}$$

The final potential difference measured between the electrodes at the end of the phase iii will be so $\Delta V = 2\Delta\Psi_i$, which if the same parameter of the simulation ($H/L = 1/3$, $n = 5$) are inserted, is

$$\Delta V = 0.8611 S_e \Delta T\,,$$

very close to the value of the phase i and of the simulation (fig. 5.17).

5.2.3 Dynamics

The equivalent electrical circuit model developed and studied must be validated comparing the results with the time-dependent FEM numerical results. The 5 electrode system analysed in the previous sections is now compared with the corresponding EEC.

The figure 5.20 shows three different ways to model the development of the surface charge in phase i: the dynamic simulation in which the temperature gradient builds up

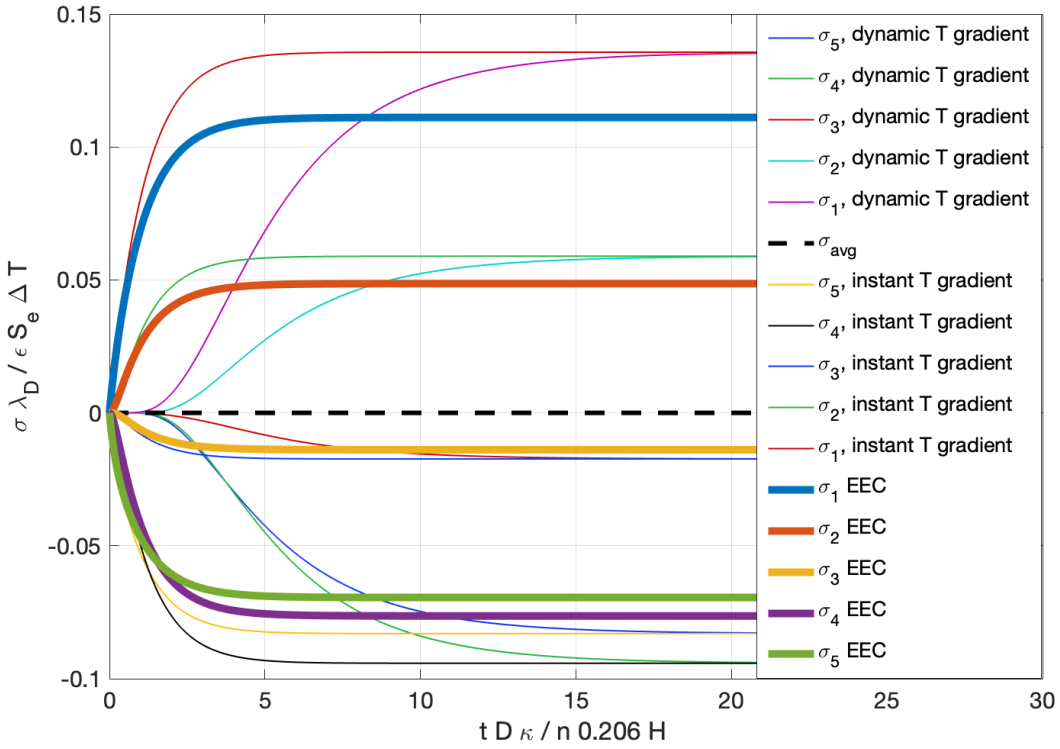

Figure 5.20: Numerical results (thin lines) and equivalent electrical circuit (thick lines) for the dimensionless surface charge $\sigma\lambda_D/\varepsilon S_e\Delta T$ of electrodes vs the dimensionless time $t\kappa D/n0.206H$, during the phase i transitory.

just imposing $T_0+\Delta T$ in $+L+H$, the simulation with instantaneous temperature gradient and the EEC results.

The difference between the time-dependent heat equation results and the time-independent one are comparable to the discrepancies seen in the two-electrodes case. The time required to reach the steady-state is of the same order of magnitude, with a difference of $\sim 10\tau_n$. This comes with no surprises: even if the number of electrodes increases the charging time constant ($\tau_n \sim n$), the selected larger length of the system increases the temperature-time ($\tau_T \sim (L+H)^2$).

The accordance between the EEC and the simulation is good in terms of characteristic times, but it misses some precision in the final steady-state values. The order of magnitude is nevertheless the same, and the differences could arise from the numerical derivative errors. The phase ii graph in figure 5.21 compares the phase ii EEC solution with the simulation results. The accordance of the final steady-state values is now precise, probably due to the sharper peaks of this phase, which permit the derivative near the electrodes to be more precise and less influenced by the point of the mesh used to do it.

The dynamics was studied comparing the time constant resulting directly from the eigenvalues of the matrix that represents the circuit. From those values the time constant of the system results to be $\tau = 6.8L/D\kappa$. This was done in order to be more precise remembering that, as stated in the original article, the precision of the formula (5.2.53) is limited to a high number of electrodes and it deviates for small numbers, as 5. The

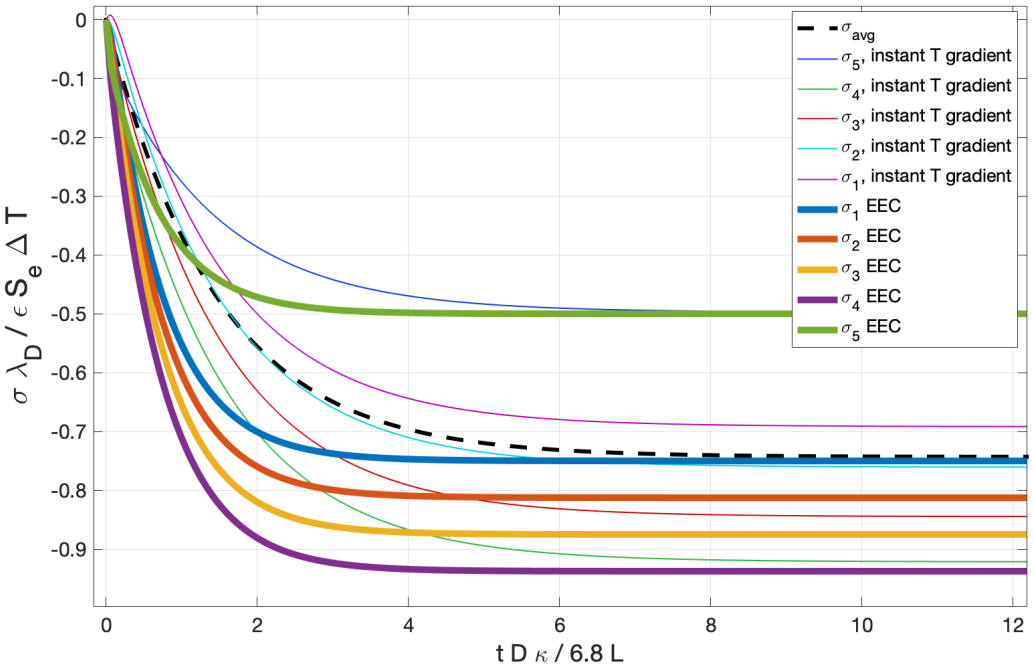

Figure 5.21: Numerical results (thin lines) and equivalent electrical circuit (thick lines) for the dimensionless surface charge $\sigma\lambda_D/\varepsilon S_e\Delta T$ for electrodes vs the dimensionless time $t\kappa D/6.8L$, during the phase ii transitory.

dynamic accordance is not perfect, the simulation required some time constants more to reach the equilibrium, but the discrepancies are acceptable.

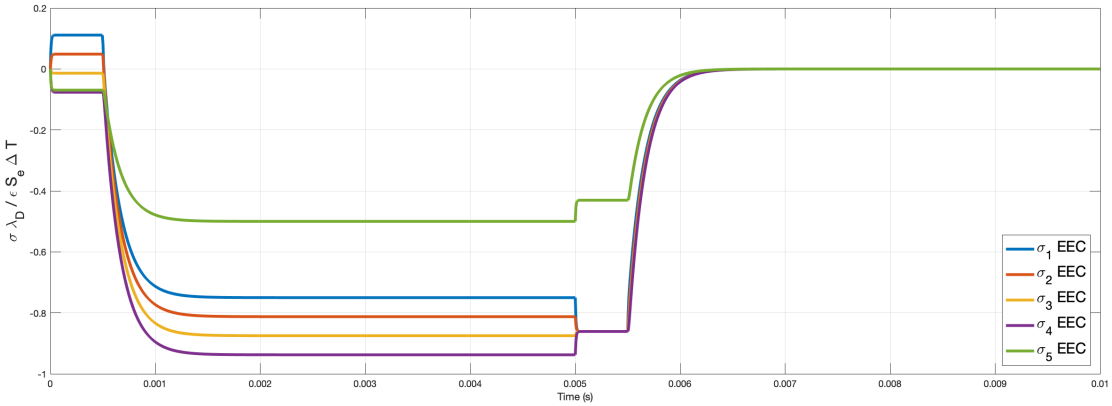

Figure 5.22: Equivalent electrical circuit results for the dimensionless surface charge $\sigma\lambda_D/\varepsilon S_e\Delta T$ of the electrodes vs the time (s). The entire charging and discharging cycle is represented.

The graphs of the charge density are no more necessary and they could result redundant. In the two electrodes system, it was established the dynamic correspondence with the surface charge, and no equivalent circuit can be used for comparison. The same

consideration can be applied to the dynamic behaviour of the neutral density which is not influenced by the presence of more electrodes.

To have a clearer picture of the complete cycle the EEC solution of all the four phases combined is plotted in figure 5.22.

The four phases are clearly distinguishable, and the big difference in the dynamics of phase i and iii with respect to the phase ii and iv is visible. It is also interesting to notice how, in the third phase, the absence of the thermal effects permits the surface charges to be superimposed and to discharge simultaneously.

From these graphs is also simple to imagine the behaviour of a high number of electrodes. Apart from the nth one, which has half the capacitance and it is so separated from the others, all the remaining $n-1$ electrodes will create a beam according to equation (5.2.54), the lines will result separated by a surface charge difference $\Delta\sigma$ of

$$\Delta\sigma = CS_e\Delta T\frac{h}{L+H} \tag{5.2.67}$$

When the temperature gradient is then removed the beam will compact into a single line with every $n-1$ electrode having the same surface charge. They will consequently discharge simultaneously.

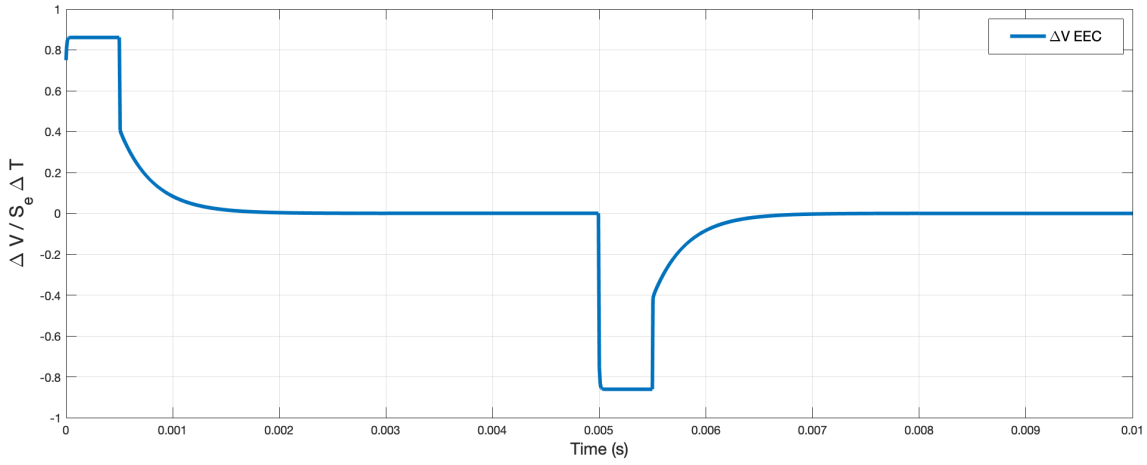

Figure 5.23: Equivalent electrical circuit results for the dimensionless potential difference between the nths electrodes $\Delta V/S_e\Delta T$ vs time (s). The entire charging and discharging cycle is represented.

The figure 5.23 confirms the experimentally measurable voltage difference observed in phase ii, even in this case a resistance of value Ω was posed in the external circuit.

Non-linear Systems

This chapter was developed in the context of the ASPRI project that aims to complete the education with a research-focused approach. Thus, it intends to complete the work done considering cases that go beyond the simple linear approximation used hereto, for these reasons more "extreme" simulations were done. In particular, two non-linear cases were analysed: the case of a high temperature and high concentration of solute, and the case of a pore length that does not permit the full development of the EDLs, so a small pores case.

6.1 High Temperature and High Concentration System

For the first case, the simulations were made with a temperature differences $\Delta T = 80K$ and an initial concentrations of ions $n_0 = 1000\, mol/m^3$. The temperature and concentration dependence of the other parameters must be now taken into account, and the Soret coefficient is expressed in terms of the Eastman heat of transport for more precision ($\alpha_\pm = Q^*_\pm / 2k_B T$). Here are listed the parameters chosen with their dependences:

Parameter	Reference
$D_\pm = 1 \cdot 10^{-9} + 5 \cdot 10^{-11}(T - T_0)\, m^2 s^{-1}$	KCl in water [65]
$Q^*_- = 8.23 \cdot 10^{-22} + 0.07 \cdot 10^{-21}(T - T_0)\, J$	Cl in water [58]
$Q^*_+ = 4.11 \cdot 10^{-21} + 0.07 \cdot 10^{-21}(T - T_0)\, J$	K in water [58]
$k = 0.6 + 1.34 \cdot 10^{-3}(T - T_0)\, W m^{-1} K^{-1}$	Distilled water [67]
$\varepsilon_r(T) = 249.4 - 0.78\, T + 7.2 \cdot 10^{-4}\, T^2$	Distilled water [68]
$\varepsilon_r(n_+, n_-) = 1 - .5 \cdot 10^{-4} \langle n \rangle + 5.1 \cdot 10^{-8} \langle n \rangle^2 - 6.8 \cdot 10^{-11} \langle n \rangle^3$	KCl in water [68]

Where $\langle n \rangle = (n_+ + n_-)/2$. The geometry was also modified to reproduce a thin nanoporous electrodes device: $L = 500\, nm$, $H = 50\, nm$ and $n = 5$, so $h = 12\, nm$.

The presence of a high concentration of ions shortens the Debye Length to $0.3\, nm$ letting the system be approximable with the model developed so far. In particular, the short Debye length permits the EDLs to be fully developed in the smaller pores present here, preserving the main hypothesis made.

6.1.1 Numerical Results

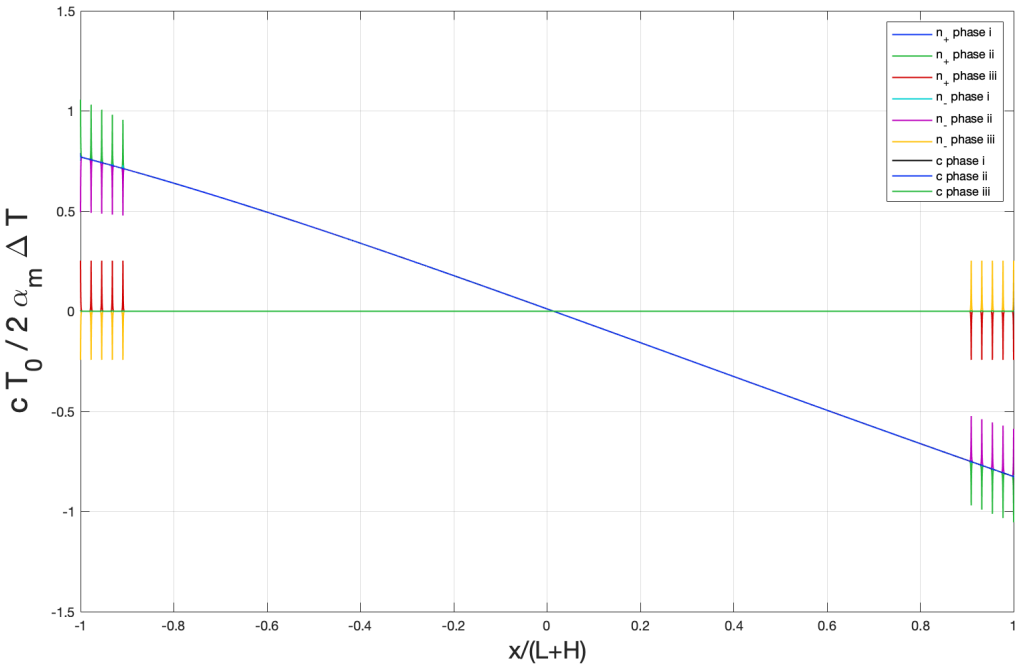

Figure 6.1: Numerical solutions of the dimensionless neutral density $cT_0/2\alpha_m\Delta T$ vs the dimensionless length $x/(L+H)$ during the phases. The ions' distributions are also represented in the graph.

The presence of a high number of non-linearities in the parameters slightly modifies the shape of the neutral concentration graph (fig. 6.1). When the temperature gradient is present the solution is not flat but it is slightly deflected.

The charge density preserves its normal shape in the various phases represented in figure 6.2, but the graph is no more perfectly symmetrical with respect to $x = 0$, due to the temperature dependence of the parameters. In fact, the phase iii results are symmetrical because the temperature difference is removed. The phase i maintains similar shape with respect to the linearizable condition, but the absolute values of the maximum charge density at the outer electrode is lower (0.03 vs 0.1).

The maximum values for phase ii are slightly lower than the usual (0.41 vs 0.5 at the outer electrode, in dimensionless units), the origin of this difference is in the strong dependence of the Debye length from the dielectric constant, that is dependent, in this case, from temperature and concentration. The values of the third phase are instead comparable (0.35 vs 0.41), signalling that the total charge accumulated in this case can be calculated as before.

The charge conservation of the phase ii - phase iii transition is present only in the left electrode. In particular, it is noticeable that in the right electrode the phase ii graph is completely covered by the phase iii graph. This means intuitively that the integral of the charge density (so the surface charge accumulated) is not conserved in the passage between the phases.

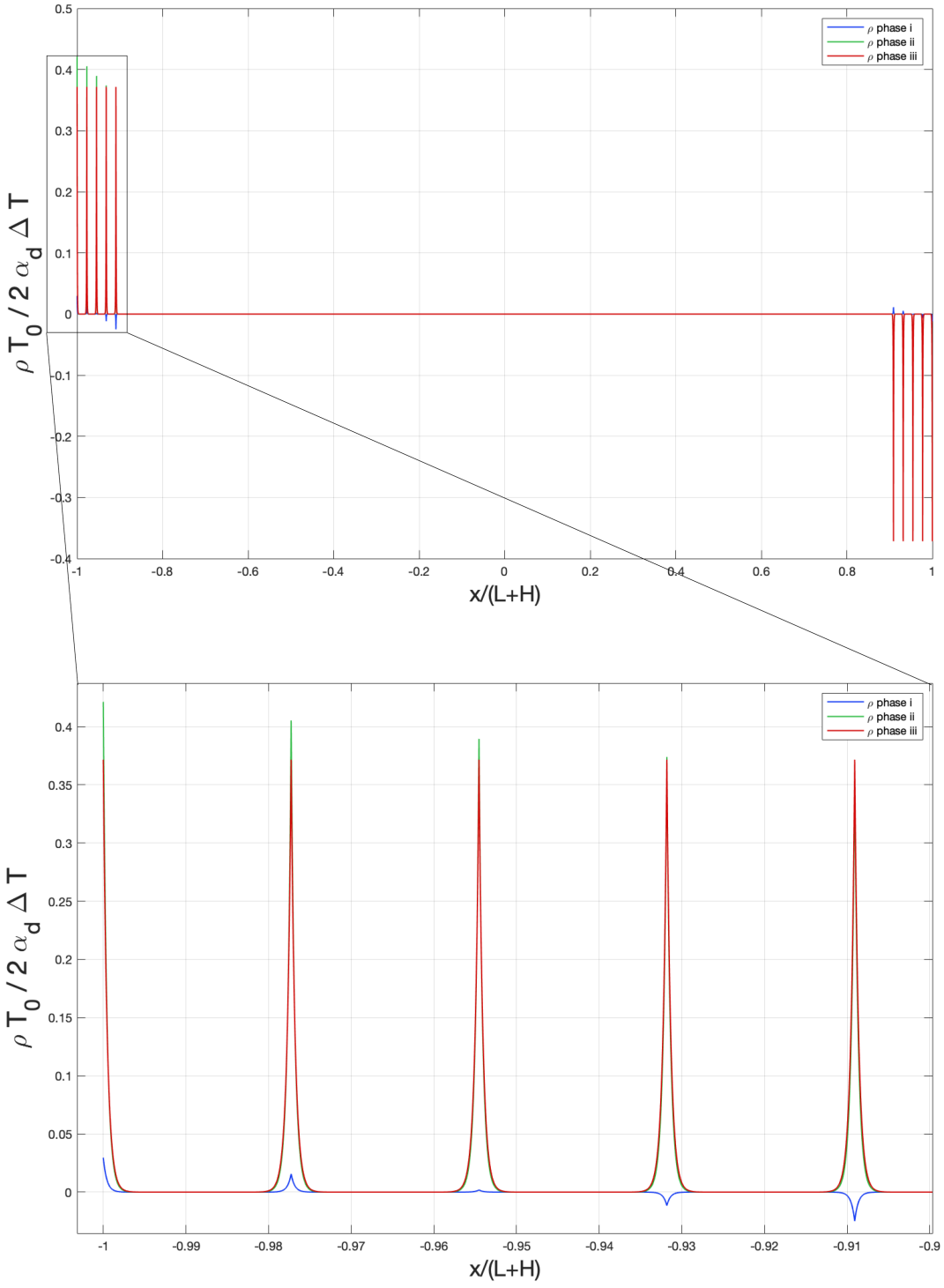

Figure 6.2: Numerical solutions of the dimensionless charge density $\rho T_0/2\alpha_d\Delta T$ vs the dimensionless length $x/(L+H)$. A zoom of the left electrode is also represented.

This has a physical origin: the right electrode is connected to the ground so it can balance its charge with respect to the left one, even after the circuit is open. This means that modelling only the electrode not connected to the ground, to calculate the final

charge present at the end of the charging cycle, permits us to understand the behaviour of the entire device.

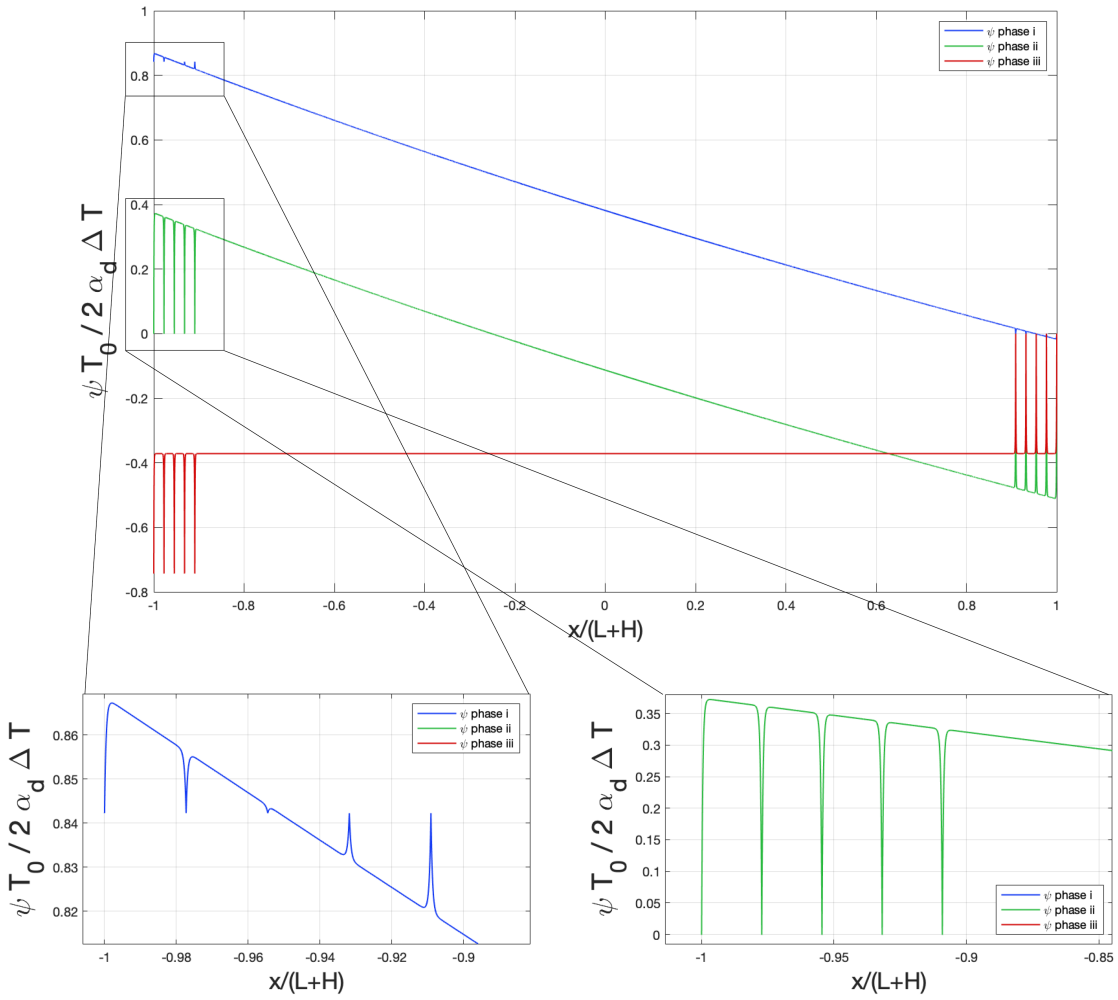

Figure 6.3: Numerical results of the dimensionless potential $\psi T_0/2\alpha_d\Delta T$ vs the dimensionless length $x/(L+H)$. Zooms for the phase i and ii are also represented.

The potential follows the behaviour of the charge density obtaining results similar to the more linear case, but with asymmetries and some differences (fig. 6.3). In phase i, the potential in contact with the outer electrode is practically the same found before, instead, in phase ii, the maximum value of the potential is lower than the one expected from previous simulations, this is linked to the differences in the charge density distribution in phase ii.

The absolute lower value of phase iii is instead similar to the one obtained previously, confirming again the possibility to use the linear EEC model to understand the behaviour of a real system.

6.1.2 Dynamics

Regarding the dynamic behaviour a comparison must be made in order to address the validity of the EEC for a more realistic model. As above, the simulations of the phase i and ii dynamics will be done from the discharged state to have a more precise FEM simulation.

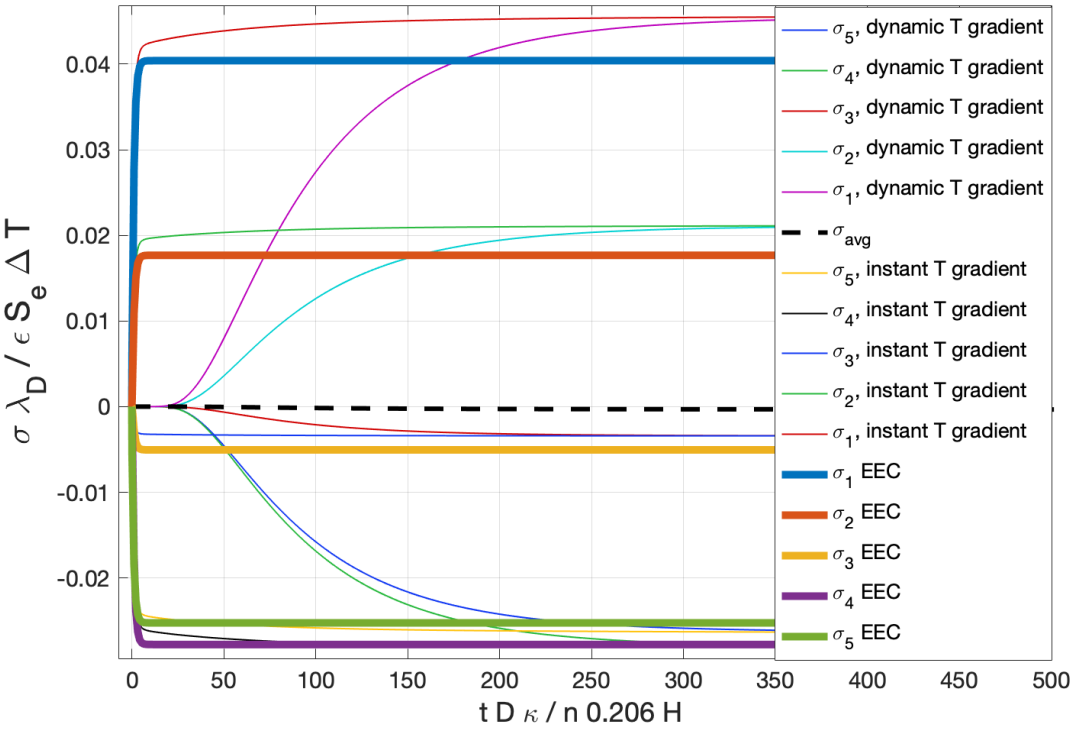

Figure 6.4: Numerical results (thin lines) and equivalent electrical circuit (thick lines) for the dimensionless surface charge $\sigma\lambda_D/\varepsilon S_e\Delta T$ for electrodes vs the dimensionless time $t\kappa D/n0.206H$, during the phase i transitory.

The phase i dynamics (fig. 6.4) is fairly similar to the one observed previously, but the much smaller Debye length ($0.3\,nm$ vs $9.62\,nm$) alters the time needed to reach the equilibrium. The temperature's time constant is now two orders of magnitude bigger than τ_n. From this data some conclusions can be drawn: the role that is played by the time constant of the heat equation depends on the balance between the overall length of the supercapacitor, the concentration, and the number of electrodes. Observing instead the case of the instantaneous temperature gradient, compared to the EEC, it is possible to state that the circuit reproduces clearly the simulation results, both in the dynamics and in the final steady-state values.

A note must be made on the shape of the surface charge plot: taking as reference "σ_1 instant T gradient", it is observable a change in the slope of the function, that deviates from the pure exponential behaviour (visible in the σ_1 EEC) due to the modification of the dielectric constant during the charging, in response to the increase in the local density of ions.

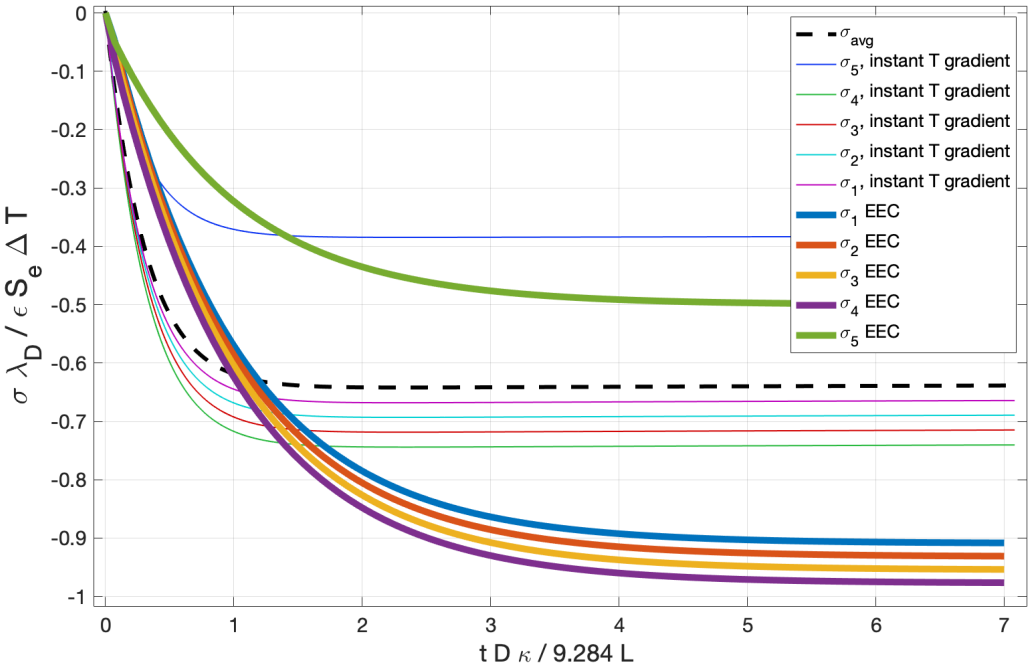

Figure 6.5: Numerical results (thin lines) and equivalent electrical circuit (thick lines) for the dimensionless surface charge $\sigma\lambda_D/\varepsilon S_e\Delta T$ for electrodes vs the dimensionless time $t\kappa D/9.284L$, during the phase ii transitory.

The figure 6.5 shows the comparison between the EEC and the numerical results of phase ii. The vertical axes normalization and the values of the capacitances of the EEC were done with the original parameter, so their values were not affected by the change in temperature and concentrations.

The accordance both on the characteristic times and the absolute steady-state values, it is not complete, but the order of magnitude is respected. This is due to the highly non-linear behaviour of the system with all the parameters dependences. In particular, the difference in the times can be understood with a simple exercise of scaling:

$$\tau_n \sim 1/\kappa \sim \sqrt{\varepsilon}\,,$$

so that it is clear how the presence of a high concentration of ions reduces the dielectric constant and consequently the characteristic times. Regarding the steady state values the situation is similar:

$$\sigma \sim \frac{\varepsilon}{\lambda_D} \sim \sqrt{\varepsilon}\,,$$

which is reduced for the same reasons.

6.2 Small Pores System

To Complete the possible cases that can be simulated, a numerical result in which the double layers are not fully developed must be shown. The parameters, except for $L = 500\,nm$ and $H = 50\,nm$, are the same of the five-electrodes low-temperature analysis, so the temperature dependence is not affecting the symmetry of the system. Having again the Debye length $\lambda_D = 9.62\,nm$ and an $h = 12\,nm$, it is obvious to conclude that the EDLs will overlap in the pores. The simulations show the results listed below.

6.2.1 Numerical Results

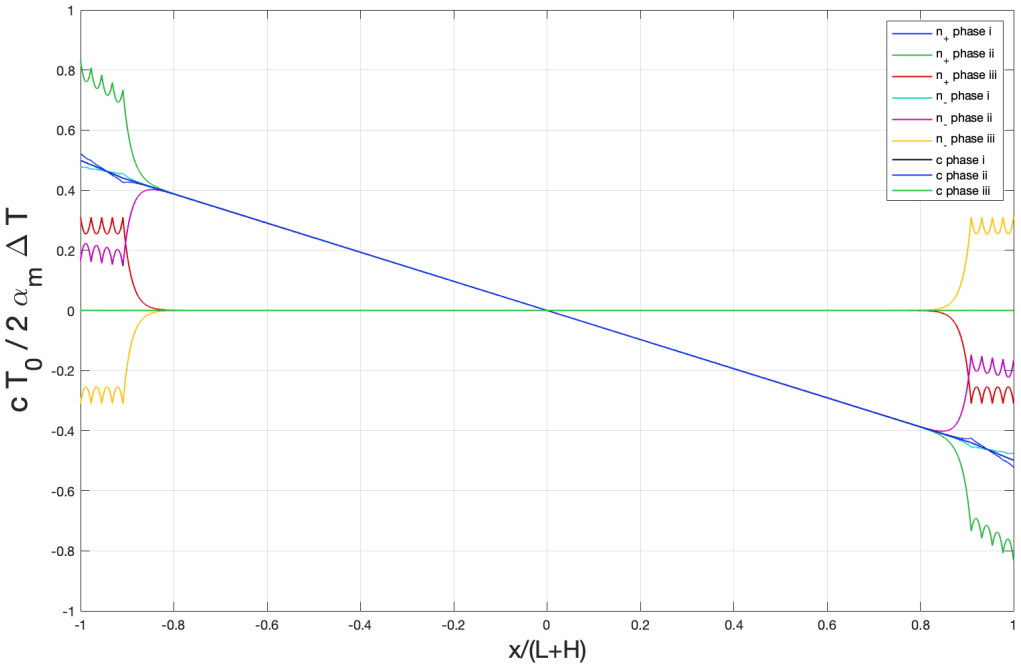

Figure 6.6: Numerical solutions of the dimensionless neutral density $cT_0/2\alpha_m\Delta T$ vs the dimensionless length $x/(L+H)$ during the phases. The ions' distributions are also represented in the graph.

It is now trivial to state that the neutral charge (fig.6.6) is not affected by the new condition and follows a linear trend, but the single ions density profiles are clearly overlapping.

Big differences arise when the charge density is plotted (fig.6.7): during phase i the charge density behaves as expected, with the usual negative and positive parts. In phase ii the maximum of the charge density in the outer electrode is almost identical to the usual one, indicating that this parameter is particularly stable. It is curious that after the equilibration of charges the maximum surface charge is slightly higher than in the non-overlapping EDLs condition, but this does not mean that the surface charge accumulated is higher.

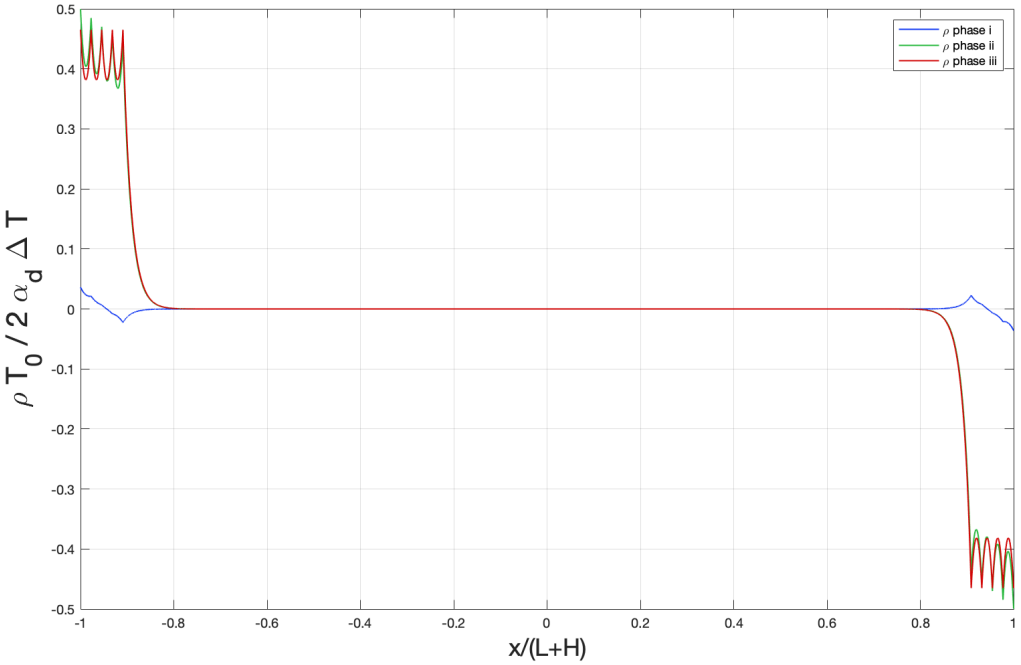

Figure 6.7: Numerical solutions of the dimensionless charge density $\rho T_0/2\alpha_d\Delta T$ vs the dimensionless length $x/(L+H)$.

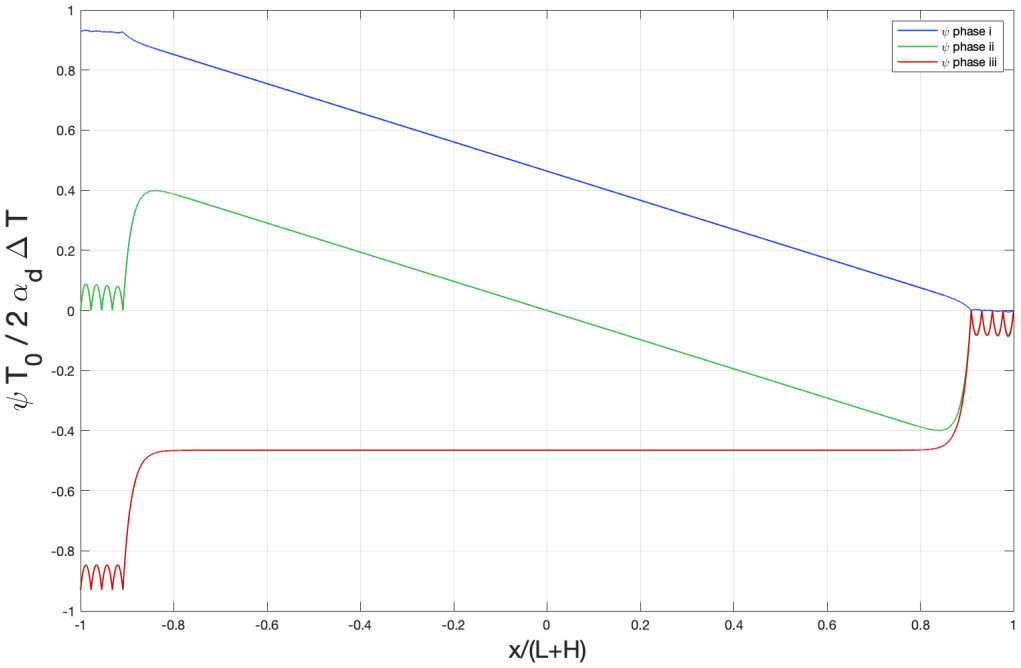

Figure 6.8: Numerical results of the dimensionless potential $\psi T_0/2\alpha_d\Delta T$ vs the dimensionless length $x/(L+H)$.

Looking at the potential (fig. 6.8), in phase i the difficulties in the development of the EDLs create an almost flat profile, with a maximum value higher than previously found. The profile of the potential in phase ii is not trivial, and difficult to understand: the reservoir part is predictable, instead the nanoporous part cannot develop the usual shape, which lets us conclude that a lower surface charge in the electrodes is present. The phase iii potential is however respecting the superposition of effect.

6.2.2 Dynamics

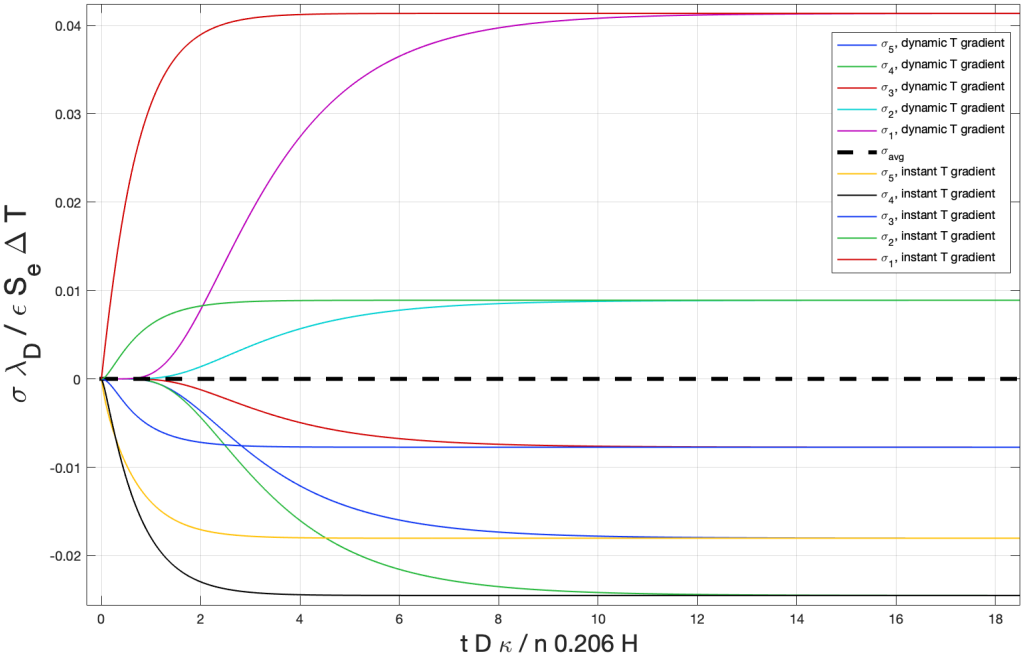

Figure 6.9: Numerical results for the dimensionless surface charge $\sigma\lambda_D/\varepsilon S_e\Delta T$ of the electrodes vs the dimensionless time $t\kappa D/n0.206H$, during the phase i transitory.

In figure 6.9 is shown the dynamic behaviour of phase i for the small pores case, the figure compares only the dynamic temperature gradient to the instantaneous temperature gradient. This choice was made because the approximation used for the capacity in the EEC is completely breached in this case and the comparison has no more sense. It is therefore interesting to notice how, for the time-independent heat equation case, the need to wait $5\tau_{n,i}$ it is perfectly respected and the dynamic temperature case varies the results of some units, but respect the order of magnitude.

The same accordance to the EEC time scale is observable in figure 6.10, which represent the phase ii dynamics.

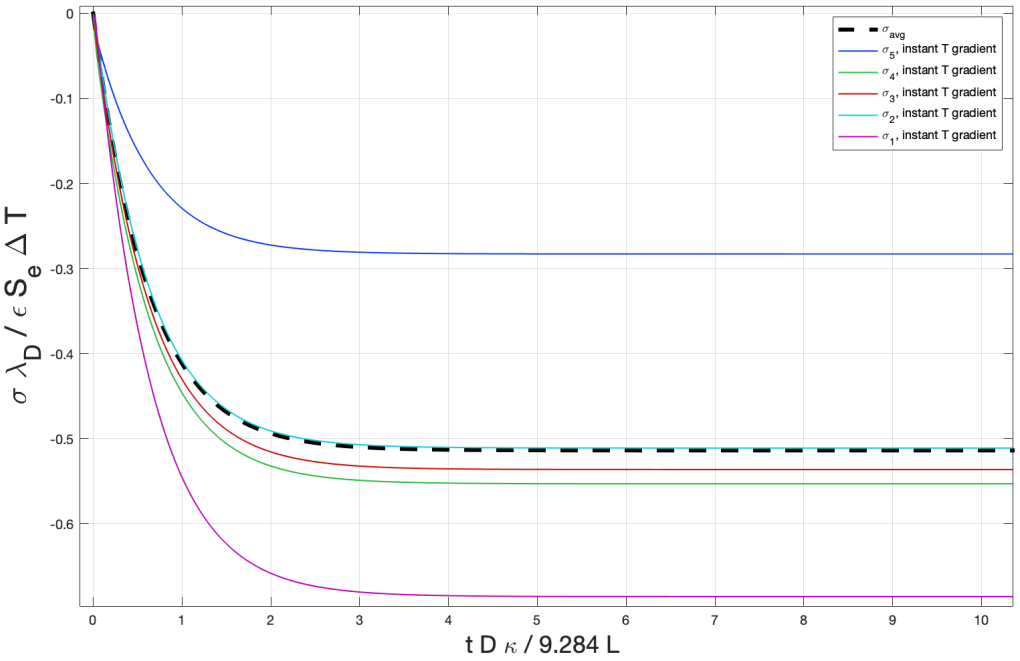

Figure 6.10: Numerical results for the dimensionless surface charge $\sigma\lambda_D/\varepsilon S_e\Delta T$ of the electrodes vs the dimensionless time $t\kappa D/9.284L$, during the phase ii transitory.

Commenting now on the values of the surface charge both in phase i and ii, it is noticeable that they are lower than the ones expected from the EEC. This happens because, when the double layers are not complete, it is not necessary the same amount of surface charge to compensate for the charge density, so the overall capacity accumulated in the electrode is lower, making the system not useful in terms of efficiency.

The physical interpretation of these results it is difficult to state, in general when the EDLs overlaps the system becomes highly non-linear and not analytically solvable.

Moreover, an electrochemical system in which both the potential and the surface charge are not imposed does not have a clear solution, the two related quantities modify themself in order to minimize the free energy, but the stable solution is not trivial. In this case, the origin of both the potential and the surface charge is the Soret effect, which relations with the electrical properties of a system are not totally clear.

Fortunately, this small pores systems are not ideal in order to exploit the maximum energy from a temperature difference, with an exception cited in the introduction: cylindrical pores with a pore diameter of the order of $1\,nm$. This particular case experimentally evaluated and theoretically analysed to provide better specific capacitance can be useful for a thermally chargeable supercapacitor. The idea is that, if the pores can contain only the ions of the same charge, the ions with a higher Soret coefficient could results inserted in the pore, and the ones with lower Soret coefficient remain outside. This could improve a lot the surface charge stored, and consequently the efficiency. Further research is necessary to demonstrate this hypothesis.

An overall conclusion on the limits in which the EEC is valid can be now made. The

time constants found approximate reliably the simulation results, they only deviate in phase i due to the time needed to establish the temperature gradient. This deviation is not so relevant for the aim of the device because the majority of the charging time is spent during phase ii. Moreover, to have optimal accordance with the numerical results, it would be sufficient to use time-dependent voltage generators, which values grow over time following the temperature time constant. Regarding the final values for the potential and the surface charges, the accordance is optimal in case of low a temperature difference, it deviates instead for the high ΔT case, preserving however the order of magnitude. The case of small-pores electrodes deviates greatly from the EEC, but its importance is limited due to the low surface charge this kind of system can contain, which makes it less useful as a device for thermal energy conversion.

Efficiency Analysis

Also this chapter was developed in the context of the ASPRI project, considering important that the physic-focused study done previously was applied to a more engineering point of view.

As declared in the introduction, the need for reliable, cheap ,and sustainable energy sources give the fundamental reason to the work here presented. The system described has the possibility to expand the range of these sources. In order to verify if this is the case, it is so necessary to use the theoretical and numerical analysis made to calculate the efficiency of the thermodynamic cycle. Understanding then if it could be enough to make a thermally rechargeable supercapacitor a useful device to convert low-temperature heat waste into electricity.

Some studies that calculate the efficiency of this kind of cycle were made [33]. The disadvantage of these studies is however the necessity to base their data on the experiments done. In particular, the capacitance and the charging times were taken from literature and the geometries of the device, so the thickness of the nanoporus electrode with respect to the reservoir, and the pore dimensions were fixed. The analysis that this work has done permits now to use the correlation demonstrated, in terms of charging times and the overall charge accumulated, to optimize the efficiency of the device.

The main difference between the efficiency calculation of a thermodynamic cycle of this kind and the one for a solid-state thermoelectric device is that in the first case the efficiency is the ratio between the overall thermal energy used E_{th} and the electrical energy that is used inside a load E_{el}, instead of being the powers' ratio:

$$\eta = \frac{E_{el}}{E_{th}}$$

The evaluation of these energies is less trivial than expected, especially if the aim is to optimize the geometry of the supercapacitor.

7.1 Thermal Energy

The contributions to the thermal energy are four:

- The energy needed to keep the temperature difference between the sides of the supercapacitor, so the heat flux times the time in which the gradient is maintained

- The heat absorbed by the electrolyte during the initial temperature rise. More precisely the heat absorbed by the electrodes should be calculated too, but the carbon electrodes have far less heat capacity than the electrolyte so it can be declarable negligible.

- The Peltier heat: the particle flux generated during the charging process due to the possibility of the ions to move towards the electrode creates a Peltier heat flux.

- The Joule heat, originated from the heat dissipation of the current flow, can be considered to flow in both the direction so that only half of it helps to maintain the temperature difference constant.

The heat flow can be simply calculated considering the thermal conductivity of the electrolyte k and the temperature difference ΔT,

$$q''_{th} = \frac{A}{2(L+H)} k\Delta T \,, \tag{7.1.1}$$

This flux is multiplied by the time required to complete the charging process,

$$E_{flux} = \frac{A}{2(L+H)} k\Delta T t_{ch} \tag{7.1.2}$$

It is so evident how the dynamic study of the system becomes fundamental in order to calculate the efficiency. The charging time t_{ch} is not unique, it depends on the various configurations and timing the phases take but the order of magnitude can be safely considered the one of $5\tau_{n,ii}$.

The heat absorbed by the electrolyte is trivially

$$E_{abs} = A(L+H)\eta_{electrolyte} c_p \Delta T \,, \tag{7.1.3}$$

that strongly depends on the geometry of the cell and the electrolyte choice, so its specific heat capacity c_p and its density $\eta_{electrolyte}$

The Peltier heat is calculated as

$$E_{Pel} = S_e(T_0 + \Delta T) \int_0^{t_{ch}} I_{ch} dt \tag{7.1.4}$$

where I_{ch} is the charging current that flows in the circuit during phase ii. The integral of the current in the charging time is therefore the total charge accumulated by the supercapacitor, that, recalling equation (5.2.58), permits to express the Peltier energy in terms of the geometry of the system

$$E_{Pel} = S_e(T_0 + \Delta T) \frac{ACS_e\Delta T}{2\left(1 + \frac{H}{L}\right)} \left(2n - 1 + \frac{H}{L}(n-1)\right) \simeq \frac{3}{4} S_e^2 (T_0 + \Delta T)\Delta T n A C \,, \tag{7.1.5}$$

in which the approximation was don for high n and $L = H$.

The Joule heat is generated by the current flow in the supercapacitor and can be calculated as

$$E_J = \frac{1}{2} R_{int} \int_0^{t_{ch}} I_{ch}^2 dt \tag{7.1.6}$$

where R_{int} is the total internal resistance of the supercapacitor, that considers the slowdown of the ions due to the presence of multiples electrodes. Considering now a current that decreases exponentially during the charging starting from the initial value $I_0 = S_e \Delta T / R_{int}$, with a time constant $R_{int} C_{tot}$. From this consideration, the value of the Joule heat recovered in the charging process is trivially

$$E_J = \frac{1}{4} S_e^2 \Delta T^2 A C_{tot} \simeq \frac{1}{4} S_e^2 \Delta T^2 n A C \,, \tag{7.1.7}$$

where the time constant was the consider the one of the phase ii previously approximated (eq (5.2.53)), neglecting the phase i timing and other configuration of the circuit in order to obtain simply the right order of magnitude.

The comparison between these energies is fundamental to understand the relative importance for the calculation of the efficiency. The main contribution is intuitively the heat flux energy so it is necessary to compare the others with respect to it.

The ratio between the flux energy and the absorbed one depends on the geometry of the system is

$$\frac{E_{flux}}{E_{abs}} = \frac{k}{\eta_{electrolyte} c_p} \frac{5 \tau_n}{2(L+H)^2} \,, \tag{7.1.8}$$

but it can be easily verified that, for the case of an aqueous electrolyte, so with the parameter used in the simulations, the ratio between the fluxes is about $E_{flux}/E_{abs} = 10^{-6} n/L$. Using now the parameters of a supercapacitor characterized and used to verify the stack electrode model by Lian and al. [40], which shows an equivalent number of electrode $n \sim 6 \cdot 10^5$ the ration becomes $E_{flux}/E_{abs} = 6 \cdot 10^{-1}/L$. The absorbed heat can so be a relevant part of the heat necessary to complete the charging cycle. Help comes from the possibility to recover that energy with complicated thermohydraulic cycles and form the usual dimension of a supercapacitor, which, being of some millimetres, make the absorbed heat thousandths times less than the flux heat, permitting to fully neglect it in these cases.

To have an idea of the order of magnitude of the energy used, taking again the data from Lian's article, the heat used to maintain the temperature gradient it is on the order of $21 \cdot 10^6 \, J$, where the area is chosen to be $1 \, m^2$, the temperature difference $80 \, K$, the conductivity $0.6 \, W m^{-1} K^{-1}$ and the overall length of $3.2 \, mm$.

Another comparison can be made between the Peltier heat and the Joule heat, that, using the approximations made, results simply

$$E_{Pel} = 3 \left(\frac{T_0}{\Delta T} + 1 \right) E_J \,, \tag{7.1.9}$$

To calculate the order of magnitude of these energies it is necessary to do some strong approximations. The value of the Seebeck coefficient S_e and the capacitance of the single nanopore C are related to the electrolyte chosen. To do a general analysis of the efficiency that can be valid for all kinds of thermally rechargeable supercapacitors it is safer to use the maximum values found in literature. The Seebeck coefficient can be so posed to the value of 10 mV/K, the relative dielectric constant to be the same of the water ($\varepsilon_r = 78.5$), the Debye length of the order of the nm and the area of $1 \, m^2$. These

values are not connected in particular to any kind of electrolyte because, for example, the polyelectrolytes or the ionic liquids have those values of Seebeck coefficient, but lower values of the dielectric constant. The result for the Joule and Peltier energies obtained is safely more than the one experimentally expected. With the parameters above declared and a temperature difference of 80 K, the Joule heat is $E_J = 7.5 \cdot 10^4\ J$. Consequently the Peltier heat is $E_{Pel} = 10^6\ J$.

These rounded up values are so negligible with respect to the flux heat, finally giving the possibility to individuate safely in that component of the thermal energy the main one that must be compared to the electrical energy.

7.2 Electrical Energy

The experiment taken as reference highlighted the presence of a leakage current during charging and a loss of charge due to irreversible processes. The model of this work considers instead an ideal case in which no irreversible processes take place. Thus, the electrical energy stored in the thermodynamics cycle is easily calculated as $E_{el} = Q_{tot}^2/2C_{tot}$. However, the particularity of the system analysed affects the modalities in which this energy is used. In particular, the load, so the object that uses the electric energy or the national grid, can be posed in the external circuit either only in the discharging phase or in both the charging and discharging phase. The first case respects the dynamics studied for phase ii so that the charging time, that affects the thermal energy needed, coincides with the one calculated, but the energy is used in the load only in the discharging phase. The second case has the drawback of a longer charging time, so more thermal energy used, but a current pass in the load both in phase ii and iv.

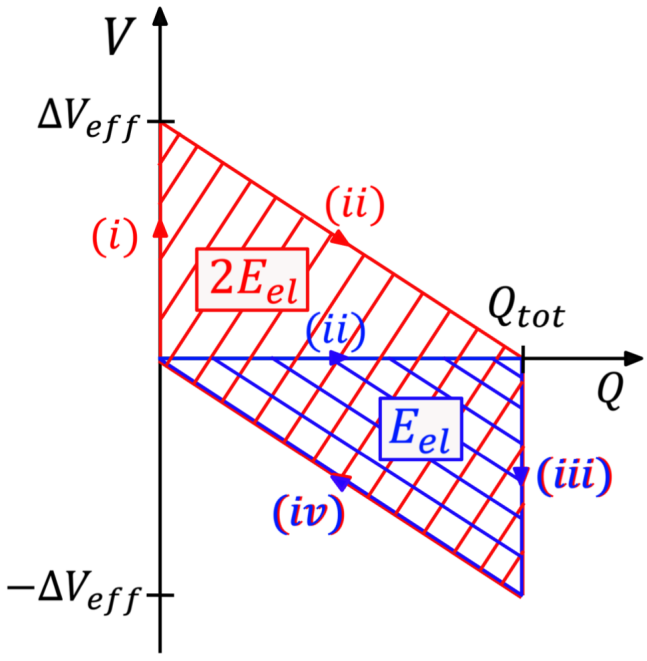

Figure 7.1: Electro-capacitive cycle for thermal energy harvesting.

Another choice that can be made is related to phase i: it is possible to charge the supercapacitor directly with the electrodes connected, avoiding the need for phase i. This saves time, but the potential difference across the cell is not completely developed when the cycle starts. As previously observed the characteristic time of phase i is however some order of magnitude lower than the one of phase ii, so it does not affect excessively the thermal energy needed to charge the supercapacitor. From a grid perspective it is better to pass through phase i before charging the capacitor and let the current flow through the load, in this way the potential during the charging decrease perfectly exponentially. If instead the heat flux is used only for charging and then the load is connected, the phase i can be avoided without risks.

For the sake of clearness, the two kinds o thermodynamics cycles are represented in figure 7.1, in which the various phases are represented in a voltage-charge graph. From the value of the potential differences across the electrodes at the end of phase iii found in equation (5.2.66), the values of the maximum and the minimum of the effective voltage in the graph are respectively

$$\Delta V_{eff} = \pm 2 \frac{S_e \Delta T}{1 + \frac{H}{L}} \frac{\left(n - \frac{1}{2} + \frac{H}{2L}(n-1)\right)}{2n-1} , \tag{7.2.1}$$

and the value of the total charge accumulated is $Q_{tot} = S_e \Delta T C_{tot}$ as previously.

The energy that passes in the load during the charging must be the same that is discharged in the last phase, this explains the symmetry of the graph and the possibility to use the voltage of the last phase as the one of the first. The graph of the short circuit charge is represented so that phase i is absent and the energy used in the load is only the one in the second quadrant. The graphical representation permits so to clearly see that the electric energy exploited in the case in which a load is positioned in phase ii is doubled with respect to the case of short circuit in phase ii.

To be more explicit the electric energy for each quadrant is

$$E^*_{el} = C \frac{(S_e \Delta T)^2}{\left(1 + \frac{H}{L}\right)^2} \frac{\left(n - \frac{1}{2} + \frac{H}{2L}(n-1)\right)^2}{2n-1} \tag{7.2.2}$$

7.3 Efficiency

From the concept of effective internal resistance R_{int}, effective total capacitance C_{tot} and effective potential difference ΔV_{eff} above explained it is possible to restate the dynamic problem in terms of the equivalent circuit in figure 7.2.

This simple circuit permits to calculate the time constant τ_{eff} of the charging and discharging phases as

$$\tau_{eff} = (R_{int} + R_{load}) C_{tot} \tag{7.3.1}$$

where R_{load} is the resistance of the load inserted in the external circuit.

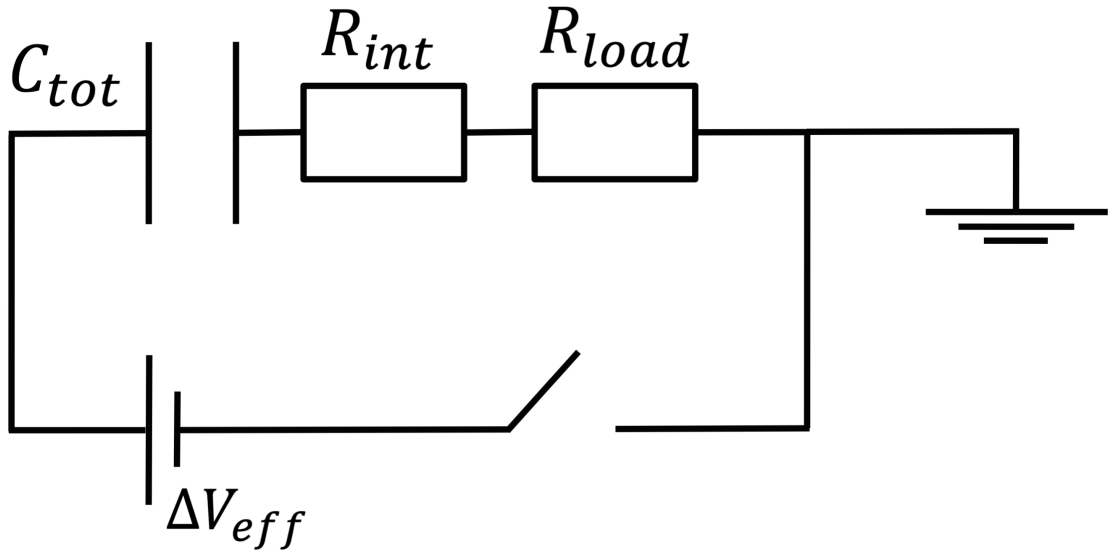

Figure 7.2: Sketch of the equivalent circuit in terms of total capacitance C_{tot}, internal resistance R_{int}, load resistance R_{load} and effective voltage V_{eff}.

Having established that the thermal energy used to maintain the temperature gradient is the main contribution and it depends on the charging time, considering a time of $5\,\tau_{eff}$ to charge the supercapacitor, the thermal energy used is so

$$E_{th} = \frac{A}{2(L+H)} k\Delta T 5\tau_{eff} \tag{7.3.2}$$

τ_{eff} depends on two factors: the value of R_{load} and the choice on whether to pass through phase i or not. It is so possible to define a generic τ_n that depends on this choice and can be written as

$$\tau_n = \frac{L\lambda_D}{D}\left(f\frac{H}{L}n + 2n - 1 - 0.91\frac{H}{L}\right) \tag{7.3.3}$$

the parameter f is 0.75 if phase i is omitted, it is instead 0.95 if phase i is completed. This discrepancy comes from the expression of $\tau_{n,i}$ of eq.(5.2.36), rewritten as $\tau_{n,i} = (L\lambda_D/D)0.2n(H/L)$, and summed to $\tau_{n,ii}$ of eq.(5.2.53). The difference is however small compared to the overall charging time. Once that this choice is made τ_{eff} depends only on the load, in particular it depends on the ratio between the internal resistance and the load resistance $a = R_{load}/R_{int}$, by

$$\tau_{eff} = \tau_n(1+a) \tag{7.3.4}$$

so that the efficiency η becomes

$$\eta = \frac{bLCS_e^2\Delta T\left(2n - 1 + \frac{H}{L}(n-1)\right)^2}{5k\tau_n\left(1+\frac{H}{L}\right)(2n-1)(1+a)} \tag{7.3.5}$$

where b is equal to 1 if the load is connected only in phase iv and it is 2 is it connected in both the charging and discharging phase.

It is so clear that two optimal situations are possible: the absence of the load, so $b = 1$ and $a = 0$ or the presence of a load that has the same resistance of the effective internal one of the supercapacitor, obtaining $b = 2$ and $a = 1$. A bigger load in the charging phase will increase the charging time leading to a more thermally expensive charging. Both these situations lead to the same efficiency, which can be restated as an equivalent dimensionless figure of merit ZT^* which depends only on the properties of the electrolyte multiplied by a geometrical factor G and the Carnot efficiency η_{Carnot}:

$$\eta = ZT^* G \eta_{Carnot} \,, \tag{7.3.6}$$

in which

$$ZT^* = \frac{S_e^2 \sigma_{el}(T_0 + \Delta T)}{k} \,, \tag{7.3.7}$$

$$G = \frac{4}{5} \frac{\left(n - \frac{1}{2} + \frac{H}{2L}(n-1)\right)^2}{(2n-1)(1+\frac{H}{L})(f\frac{H}{L}n + 2n - 1 - 0.91\frac{H}{L})} \,, \tag{7.3.8}$$

$$\eta_{Carnot} = \frac{\Delta T}{T_0 + \Delta T} \tag{7.3.9}$$

The geometrical factor G is so the absent factor of the efficiency analysis done in literature, and it justifies the strong approximations made to calculate the formula for the efficiency. G is a function of the ratio between the electrode dimension, the reservoir dimension and of the number of electrodes. The ratio H/L distinguishes between thick and thin electrodes giving some hints on the optimal geometry, the number of electrodes n is inversely proportional to the pore dimension. This factor does not take into account the physical limits of the problem, for example, the pore dimension cannot be less than about $1\,nm$ and it is known that if it is small enough to limit the development of the EDL the capacitance used is no more valid, so when the evaluation of the optimal geometry is done, some limits on the parameters must be posed.

Before starting the optimization a first look at the formula permits to notice that both the numerator and the denominator are proportional to n^2 and $(H/L)^2$. This means that for low pore dimensions and thick nanoporous electrodes the efficiency reaches a plateau because the gains in the charge accumulated are balanced by the higher charging times and so in the greater thermal energy used.

The limits of the factor G are readily calculated:

- if a planar capacitor is used, $n = 1$ and $H = 0$ so that

$$G = 1/5 = 0.2 \tag{7.3.10}$$

- if a nanoporous electrode capacitor is used, n is much bigger than 1, so that the terms that are not multiplied by n can be neglected, obtaining

$$G \simeq \frac{2}{5} \frac{\left(1 + \frac{H}{2L}\right)^2}{\left(1 + \frac{H}{L}\right)\left(2 + f\frac{H}{L}\right)} \tag{7.3.11}$$

  distinguishing the case for thin nanoporous electrodes ($H/L << 1$) and thick nanoporous electrodes ($H/L >> 1$) we found respectively $G = 1/5 = 0.2$ and

$G = 1/(10f)$ which varies between 0.133 and 0.105 selecting the two different values of f. The function is monotonous and decreasing so that no maximums can be found in this approximation.

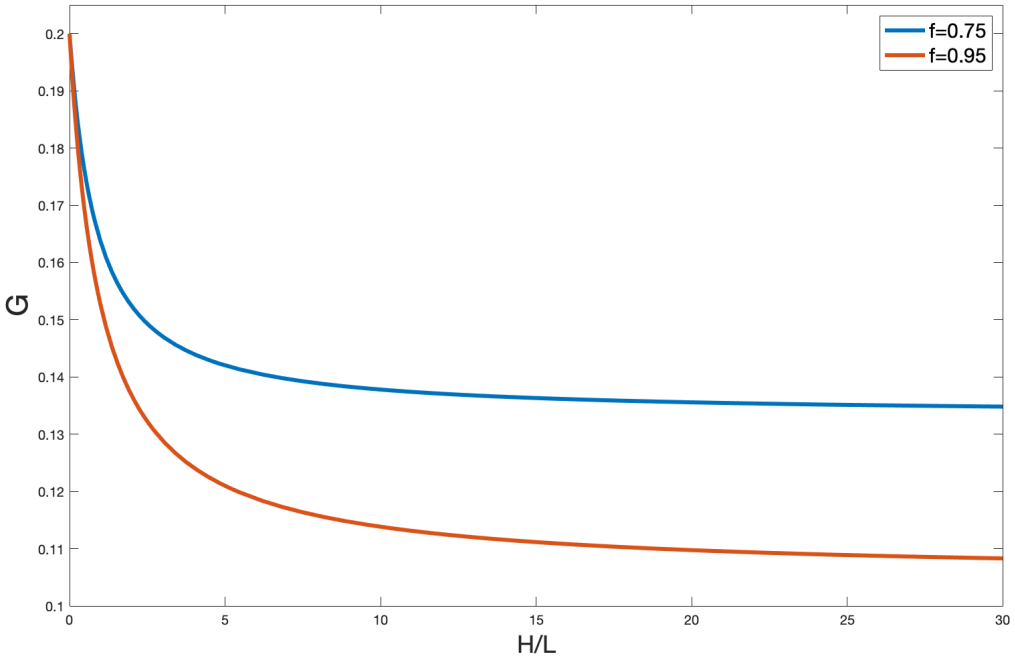

Figure 7.3: Geometrical factor G vs the ratio between the nanoporous electrode and the reservoir length H/L.

These considerations on the geometrical factor lead to the particular conclusion that a planar capacitor can have better efficiency than a nanoporous carbon one. This is partially due to the approximation made, but it is also linked to the intrinsic high charging times of a supercapacitor. However as it is possible to see in figure 7.3 for a thin nanoporous electrode supercapacitor the loss in efficiency is very limited and it is compensated by the practical need to increase the total charge accumulated and the possibility to optimize the dynamics linked to, for example, the thermohydraulic time constants.

The geometrical factor G becomes so a useful tool in order to build a device that can be adapted to the needs of the overall plant, so that it is easy to imagine a supercapacitor with a large reservoir L and a thin nanoporous electrode in which the pores' dimensions are small enough to have a high number of it, but big enough to accommodate for the full development of the EDL.

The dimensionless figure of merit ZT^* is related only to the physical behaviour of the electrolyte, in particular, as for the case of the thermoelectric semiconductors devices, it is proportional to the squared Seebeck coefficient S_e, the electrical conductivity σ_{el} and inversely proportional to the thermal conductivity k.

The big difference with respect to the solid-state case is that the electrical and the thermal conductivity are not strictly related as in the case of the metals in which the

electrons bring both heat and charge linking the two conductivities. The thermal conductivity of molecular liquids is instead much poorly linked to the electrical conductivity, in fact, some models show that the thermal conductivity is directly proportional to the viscosity [69], instead the electrical conductivity is proportional to the mobility and the concentration of the ions. Moreover, the thermal conductivity of the liquids are always on the order of $0.1 - 1\, Wm^{-1}K^{-1}$ and the Seebeck coefficients can reach values of tens of mVK^{-1} which are respectively much lower and much higher than the usual values of a solid material. However these advantages are compensated by the low electrical conductivity of the electrolytes, in fact, that is usually far smaller than the ones of a semiconductor which are of the order of $10^5\ Sm^{-1}$, a typical value of an ionic liquid is for example $0.1 - 3\, Sm^{-1}$ [70], which is similar to the one of a $1\, M$ potassium chloride solution in water that is about $3\, Sm^{-1}$. Some exceptions can be obtained by mixing ionic liquids and water reaching conductivities of even $100\, Sm^{-1}$, but these solutions don't have the high Seebeck coefficient values needed [71].

With the values above cited and considering that the application of the device is in the temperature range of 100 °C so $373\ K$, the dimensionless figure of merit of a hypothetical optimal electrolyte can be 0.373 where a Seebeck coefficient of $10\, mVK^{-1}$, thermal conductivity of $0.1\, Wm^{-1}K^{-1}$ and a conductivity of $1\, Sm^{-1}$ were chosen. This example is made to have a clearer perspective of the actual possible efficiency of this kind of device, which, considering an optimization of the geometrical factor that makes it $G = 0.2$, is in the range of 7% of the Carnot efficiency. It must be noticed that the figure of merit in analysis comes from the EEC, so it holds with good precision only in case of dilute electrolyte in low thermal gradient in which the solution can be linearised. If others types of electrolyte such ionic liquids or polyelectrolytes are chosen, the values obtained can only approximate the order of magnitude. Moreover, as stated above, the system is ideal so a real system, with irreversible processes, will have an even lower efficiency.

In addition, these hypothetical values are not present in the current literature, the best electrolytes present have ZT^* of the order of 10^{-2} which returns the 0.2% of the Carnot efficiency [33].

It is so clear that, in order to have a device that can help in the production of energy, an electrolyte with a figure of merit in the order of the unity must be found. Considering that the thermal conductivity for the liquids cannot be reduced too much, it is necessary to increase the electrical conductivity maintaining the already optimal results for the Seebeck coefficients.

The efficiency formula here calculated can so help principally for the purpose of the geometry optimization, in particular in the choice of thin electrodes. Is instead beyond the scope of this thesis to overcome the limitation of the dimensionless figure of merit, being mainly a matter of materials choices and chemical optimization.

Conclusions and Perspectives

This Thesis Work was developed in the framework of the Seebeck effect in liquid systems. The aim was to understand the microscopic internal behaviour of a supercapacitor charged with low-temperature heat sources. Different methods were applied and modified in order to fulfill the needs of this particular device.
Starting from the linearisation used by Stout and al.[58] to solve the PNP equations between two planar electrodes in open circuit, a novel analytical solution was found for the case of short circuit condition. This solution, confirmed then by numerical simulations, permitted to evaluate the potential and, more importantly, the surface charge accumulated at the electrodes as a function of the temperature difference applied. Consequently, the capacitance of this particular kind of double layer was found to be approximable by the usual Poisson-Boltzmann EDL specific capacitance $C = \varepsilon/\lambda_D$. Thanks to this finding, an equivalent electrical circuit, that represents the electrochemical capacitor, was developed. In particular, this EEC has the new characteristic of having the voltage generator inside the electrolyte part of the circuit, to account for the thermo-voltage that the Seebeck effect produces. This circuit was then numerically validated, both from a dynamic and a steady-state point of view, showing how, with its simple algebraic solution, it is possible to understand the overall behaviour of a complex system such as a thermoelectric capacitor.
The focus was then shifted towards the nanoporous electrodes scenario, modelled with the Stack Electrodes Model (SEM), previously developed by Lian and al. [40]. The SEM was initially simulated in the simple case of a two-electrodes system, finding surprisingly that a negative charge density appears in the cold electrode. This result was firstly considered an error of the boundary conditions imposed, but then, after some discussions in the research group, it was explained considering the balance between the charge conservation in the nanoporous electrode and the potential induced by the Seebeck effect. The two-electrodes setup was so fully simulated and represented by the EEC, in which, in this case, voltage generators were present also between the electrodes.
Thus, with the basis posed by the simple systems studied before, a general solution for an n-electrodes system was found. The dynamics and the steady-state of both the open and closed circuit conditions was then analysed. It was found that the charge dynamics of a thermally recharged supercapacitor coincides with the one of an electrically charged one, confirming the experimental results. This was proven simply by noticing how the ordinary differential equations systems originated by the EEC is solved by a dynamic matrix, that coincides with the one found by Lian and al. The validity of the time constants found is so linked to the validity of Lian's model. Starting from the EEC, it was also possible to evaluate the effective capacitance, noticing how the thermal gradient present inside the

nanoporous electrodes reduces it from its original value, due to the non-constant potential inside the electrodes.
In the context of the deepening of the ASPRI project in which this Thesis was made, the limits of the linear EEC were found, simulating the cases of high temperature gradients, together with high concentrations, and the case of electrodes with small pores. The accordance between the circuit solution and these "extreme" cases is surprisingly good. The circuit can predict the right order of magnitude of both the time constants and the steady-state values in the case of high temperature and high concentrations, explaining instead only the dynamic of the system in the small pores case.
Also in the context of ASPRI project, the efficiency of the thermodynamic cycle was calculated and optimized. The importance of the definition of the charging times is evident when the thermal energy used must be calculated because the majority of the thermal energy is spent for maintaining the thermal flux. The effective capacitance resulted instead fundamental to calculate the actual electrical energy accumulated by the system, that differs from the one expected if a voltage equivalent to $S_e\Delta T$ is applied. These two contributions permitted to find a function for the efficiency which is the product of an equivalent dimensionless figure of merit ZT^*, a geometrical factor G and the Carnot efficiency. The geometrical factor was used to optimize the configuration of the system to obtain the maximum efficiency, in particular, it can be noticed how both the charging time and the electrical energy depends linearly on the number of pores $n-1$, so that in a real supercapacitor these factors compensate each other, leaving only to the proportion between the nanoporous electrodes' thickness and the overall length the task to optimize the efficiency. It was surprisingly found that the optimal configuration consists of either a thin nanoporous electrode or a planar electrode, both of which have $G = 0.2$. Thus, it is ZT^* the factor to work on. Considering that the liquids have already a low thermal conductivity and some experiments showed Seebeck coefficients of the order of $10\,mV$, it is necessary to work on the electrical conductivity that, being different order of magnitude lower than the semiconductor's one, limits the ZT^*.

Beyond the, already cited, lack of knowledge on the origin of the Soret effect, other future researches are hoped to expand and complete the model presented in this work.
The experiments show that the systems with higher Seebeck coefficients are not based on aqueous solvent, but instead on ionic liquids or on polyelectrolytes. The effects of a temperature gradient on these kinds of electrolyte should be investigated and the stack electrodes model should be so adapted.
It is also known that the Seebeck effect is increased, or decreased, by the temperature dependence of the interaction potential between the particles and the surfaces of the electrodes [47]. In certain cases, this interaction is so strong that the same electrolyte can have a negative Seebeck coefficient, instead of a calculated positive one, when a particular material is used as electrode [45]. This added potential should be so taken into account, the EEC developed can be a strong tool to model the system because it should be sufficient to modify the voltage generated to consider the added potential difference.
Furthermore, some experimental measures and their theoretical interpretations show how supercapacitors with an average pores size of some nanometre, when charged, don't develop an EDL at the interface, accommodating only the counterions inside the pore. It should be so investigated if the same effect happens in case the of a thermal charge and if

this can increase the efficiency of the cycle.
Finally, it would be also interesting to evaluate the dynamics of the system if the temperature gradient is alternated harmonically. Considering the high thermal-voltages obtainable, an alternating temperature difference could lead to an alternated voltage which could, in turn, save thermal energy and increase efficiency.

In conclusion, it is hoped that the present Thesis Work could give a contribution to the novel research field of the study of thermoelectric effects in liquids. As highlighted above, multiples routes are being followed with the aim to create a reliable and cheap device that could convert low-temperature heat waste into electricity. The model here developed should so be improved in order to establish if a thermally rechargeable supercapacitor should be one of the paths to follow.

Bibliography

[1] G. Post, M. Roser, and H. Ritchie, 2020. [Online]. Available: https://ourworldindata.org/

[2] C. B. Vining, "An inconvenient truth about thermoelectrics," *Nature Materials*, vol. 8, no. 2, pp. 83–85, 2009, cited By :509. [Online]. Available: www.scopus.com

[3] Y. Yang, J. Loomis, H. Ghasemi, S. W. Lee, Y. J. Wang, Y. Cui, and G. Chen, "Membrane-free battery for harvesting low-grade thermal energy," *Nano Letters*, vol. 14, no. 11, pp. 6578–6583, 2014, cited By :76. [Online]. Available: www.scopus.com

[4] M. Rahimi, A. P. Straub, F. Zhang, X. Zhu, M. Elimelech, C. A. Gorski, and B. E. Logan, "Emerging electrochemical and membrane-based systems to convert low-grade heat to electricity," *Energy and Environmental Science*, vol. 11, no. 2, pp. 276–285, 2018, cited By :48. [Online]. Available: www.scopus.com

[5] J. Huang, B. G. Sumpter, and V. Meunier, "A universal model for nanoporous carbon supercapacitors applicable to diverse pore regimes, carbon materials, and electrolytes," *Chemistry - A European Journal*, vol. 14, no. 22, pp. 6614–6626, 2008, cited By :435. [Online]. Available: www.scopus.com

[6] R. van Roij, *Soft Condensed Mattter Theory.* Utrecht: Utrecht University, 2020.

[7] F. Campana, M. Bianchi, L. Branchini, A. De Pascale, A. Peretto, M. Baresi, A. Fermi, N. Rossetti, and R. Vescovo, "Orc waste heat recovery in european energy intensive industries: Energy and ghg savings," *Energy Conversion and Management*, vol. 76, pp. 244–252, 2013, cited By :140. [Online]. Available: www.scopus.com

[8] K. Murakami and M. Nemoto, "Some experiments and considerations on the behavior of thermomagnetic motors," *IEEE Transactions on Magnetics*, vol. 8, no. 3, pp. 387–389, 1972.

[9] M. F. Dupont, D. R. MacFarlane, and J. M. Pringle, "Thermo-electrochemical cells for waste heat harvesting-progress and perspectives," *Chemical Communications*, vol. 53, no. 47, pp. 6288–6302, 2017, cited By :56. [Online]. Available: www.scopus.com

[10] T.J.Seebeck, "Ueber die magnetische polarisation der metalle und erze durch temperatur- differenz," *Annalen der Physik*, vol. 82, pp. 133–160, 1821. [Online]. Available: www.scopus.com

[11] H. S. Kim, W. Liu, G. Chen, C. . Chu, and Z. Ren, "Relationship between thermoelectric figure of merit and energy conversion efficiency," *Proceedings of the National Academy of Sciences of the United States of America*, vol. 112, no. 27, pp. 8205–8210, 2015, cited By :236. [Online]. Available: www.scopus.com

[12] T. J. Abraham, D. R. MacFarlane, and J. M. Pringle, "Seebeck coefficients in ionic liquids -prospects for thermo-electrochemical cells," *Chemical Communications*, vol. 47, no. 22, pp. 6260–6262, 2011, cited By :103. [Online]. Available: www.scopus.com

[13] A. P. Straub, N. Y. Yip, S. Lin, J. Lee, and M. Elimelech, "Harvesting low-grade heat energy using thermo-osmotic vapour transport through nanoporous membranes," *Nature Energy*, vol. 1, no. 7, 2016, cited By :116. [Online]. Available: www.scopus.com

[14] S. W. Lee, Y. Yang, H.-W. Lee, H. Ghasemi, D. Kraemer, G. Chen, and Y. Cui, "An electrochemical system for efficiently harvesting low-grade heat energy," *Nature Communications*, vol. 5, no. 1, 2014.

[15] B. E. Logan and M. Elimelech, "Membrane-based processes for sustainable power generation using water," *Nature*, vol. 488, no. 7411, pp. 313–319, 2012, cited By :800. [Online]. Available: www.scopus.com

[16] F. Zhang, J. Liu, W. Yang, and B. E. Logan, "A thermally regenerative ammonia-based battery for efficient harvesting of low-grade thermal energy as electrical power," *Energy and Environmental Science*, vol. 8, no. 1, pp. 343–349, 2015, cited By :87. [Online]. Available: www.scopus.com

[17] N. Y. Yip, D. Brogioli, H. V. M. Hamelers, and K. Nijmeijer, "Salinity gradients for sustainable energy: Primer, progress, and prospects," *Environmental Science and Technology*, vol. 50, no. 22, pp. 12 072–12 094, 2016, cited By :100. [Online]. Available: www.scopus.com

[18] J. W. Post, J. Veerman, H. V. M. Hamelers, G. J. W. Euverink, S. J. Metz, K. Nymeijer, and C. J. N. Buisman, "Salinity-gradient power: Evaluation of pressure-retarded osmosis and reverse electrodialysis," *Journal of Membrane Science*, vol. 288, no. 1-2, pp. 218–230, 2007, cited By :376. [Online]. Available: www.scopus.com

[19] M. Tedesco, A. Cipollina, A. Tamburini, I. D. L. Bogle, and G. Micale, "A simulation tool for analysis and design of reverse electrodialysis using concentrated brines," *Chemical Engineering Research and Design*, vol. 93, pp. 441–456, 2015, cited By :92. [Online]. Available: www.scopus.com

[20] D. Brogioli, R. Ziano, R. A. Rica, D. Salerno, O. Kozynchenko, H. V. M. Hamelers, and F. Mantegazza, "Exploiting the spontaneous potential of the electrodes used in the capacitive mixing technique for the extraction of energy from salinity difference," *Energy and Environmental Science*, vol. 5, no. 12, pp. 9870–9880, 2012, cited By :82. [Online]. Available: www.scopus.com

[21] A. P. Straub and M. Elimelech, "Energy efficiency and performance limiting effects in thermo-osmotic energy conversion from low-grade heat," *Environmental Science and Technology*, vol. 51, no. 21, pp. 12 925–12 937, 2017, cited By :31. [Online]. Available: www.scopus.com

[22] T. J. Abraham, D. R. Macfarlane, R. H. Baughman, L. Jin, N. Li, and J. M. Pringle, "Towards ionic liquid-based thermoelectrochemical cells for the harvesting of thermal energy," *Electrochimica Acta*, vol. 113, pp. 87–93, 2013, cited By :39. [Online]. Available: www.scopus.com

[23] R. Hu, B. A. Cola, N. Haram, J. N. Barisci, S. Lee, S. Stoughton, G. Wallace, C. Too, M. Thomas, A. Gestos, M. E. Dela Cruz, J. P. Ferraris, A. A. Zakhidov, and R. H. Baughman, "Harvesting waste thermal energy using a carbon-nanotube-based thermo-electrochemical cell," *Nano Letters*, vol. 10, no. 3, pp. 838–846, 2010, cited By :239. [Online]. Available: www.scopus.com

[24] A. Sosnowska, E. Laux, H. Keppner, T. Puzyn, and M. Bobrowski, "Relatively high-seebeck thermoelectric cells containing ionic liquids supplemented by cobalt redox couple," *Journal of Molecular Liquids*, vol. 316, 2020. [Online]. Available: www.scopus.com

[25] T. Kim, J. S. Lee, G. Lee, H. Yoon, J. Yoon, T. J. Kang, and Y. H. Kim, "High thermopower of ferri/ferrocyanide redox couple in organic-water solutions," *Nano Energy*, vol. 31, pp. 160–167, 2017, cited By :30. [Online]. Available: www.scopus.com

[26] I. Burmistrov, N. Kovyneva, N. Gorshkov, A. Gorokhovsky, A. Durakov, D. Artyukhov, and N. Kiselev, "Development of new electrode materials for thermo-electrochemical cells for waste heat harvesting," *Renewable Energy Focus*, vol. 29, pp. 42–48, 2019, cited By :9. [Online]. Available: www.scopus.com

[27] H. Im, T. Kim, H. Song, J. Choi, J. S. Park, R. Ovalle-Robles, H. D. Yang, K. D. Kihm, R. H. Baughman, H. H. Lee, T. J. Kang, and Y. H. Kim, "High-efficiency electrochemical thermal energy harvester using carbon nanotube aerogel sheet electrodes," *Nature Communications*, vol. 7, 2016, cited By :96. [Online]. Available: www.scopus.com

[28] A. Härtel, M. Janssen, D. Weingarth, V. Presser, and R. Van Roij, "Heat-to-current conversion of low-grade heat from a thermocapacitive cycle by supercapacitors," *Energy and Environmental Science*, vol. 8, no. 8, pp. 2396–2401, 2015, cited By :54. [Online]. Available: www.scopus.com

[29] P. A. Linford, L. Xu, B. Huang, Y. Shao-Horn, and C. V. Thompson, "Multi-cell thermogalvanic systems for harvesting energy from cyclic temperature changes," *Journal of Power Sources*, vol. 399, pp. 429–435, 2018, cited By :1. [Online]. Available: www.scopus.com

[30] D. Reynard, C. R. Dennison, A. Battistel, and H. H. Girault, "Efficiency improvement of an all-vanadium redox flow battery by harvesting low-grade heat," *Journal of Power Sources*, vol. 390, pp. 30–37, 2018, cited By :16. [Online]. Available: www.scopus.com

[31] Y. Yang, S. W. Lee, H. Ghasemi, J. Loomis, X. Li, D. Kraemer, G. Zheng, Y. Cui, and G. Chen, "Charging-free electrochemical system for harvesting low-grade thermal energy," *Proceedings of the National Academy of Sciences of the United States of America*, vol. 111, no. 48, pp. 17 011–17 016, 2014, cited By :98. [Online]. Available: www.scopus.com

[32] I. Atlas and G. Z. Ramon, "Periodic energy conversion in an electric-double-layer capacitor," *Journal of colloid and interface science*, vol. 530, pp. 675–685, 2018, cited By :3. [Online]. Available: www.scopus.com

[33] H. Wang, D. Zhao, Z. U. Khan, S. Puzinas, M. P. Jonsson, M. Berggren, and X. Crispin, "Ionic thermoelectric figure of merit for charging of supercapacitors," *Advanced Electronic Materials*, vol. 3, no. 4, 2017, cited By :27. [Online]. Available: www.scopus.com

[34] D. Zhao, H. Wang, Z. U. Khan, J. C. Chen, R. Gabrielsson, M. P. Jonsson, M. Berggren, and X. Crispin, "Ionic thermoelectric supercapacitors," *Energy and Environmental Science*, vol. 9, no. 4, pp. 1450–1457, 2016, cited By :79. [Online]. Available: www.scopus.com

[35] L. Zhang and X. S. Zhao, "Carbon-based materials as supercapacitor electrodes," *Chemical Society Reviews*, vol. 38, no. 9, pp. 2520–2531, 2009, cited By :4741. [Online]. Available: www.scopus.com

[36] M. Janssen, E. Griffioen, P. M. Biesheuvel, R. Van Roij, and B. Erné, "Coulometry and calorimetry of electric double layer formation in porous electrodes," *Physical Review Letters*, vol. 119, no. 16, 2017, cited By :13. [Online]. Available: www.scopus.com

[37] G. Feng and P. T. Cummings, "Supercapacitor capacitance exhibits oscillatory behavior as a function of nanopore size," *Journal of Physical Chemistry Letters*, vol. 2, no. 22, pp. 2859–2864, 2011, cited By :233. [Online]. Available: www.scopus.com

[38] C. Lian, S. Zhao, H. Liu, and J. Wu, "Time-dependent density functional theory for the charging kinetics of electric double layer containing room-temperature ionic liquids," *Journal of Chemical Physics*, vol. 145, no. 20, 2016, cited By :23. [Online]. Available: www.scopus.com

[39] M. Janssen, A. Härtel, and R. Van Roij, "Boosting capacitive blue-energy and desalination devices with waste heat," *Physical Review Letters*, vol. 113, no. 26, 2014, cited By :41. [Online]. Available: www.scopus.com

[40] C. Lian, M. Janssen, H. Liu, and R. Van Roij, "Blessing and curse: How a supercapacitor's large capacitance causes its slow charging," *Physical Review Letters*, vol. 124, no. 7, 2020, cited By :13. [Online]. Available: www.scopus.com

[41] M. Mirzadeh, F. Gibou, and T. M. Squires, "Enhanced charging kinetics of porous electrodes: Surface conduction as a short-circuit mechanism," *Physical Review Letters*, vol. 113, no. 9, 2014, cited By :36. [Online]. Available: www.scopus.com

[42] W. Kobayashi, A. Kinoshita, and Y. Moritomo, "Seebeck effect in a battery-type thermocell," *Applied Physics Letters*, vol. 107, no. 7, 2015, cited By :5. [Online]. Available: www.scopus.com

[43] A. Al-Zubaidi, X. Ji, and J. Yu, "Thermal charging of supercapacitors: A perspective," *Sustainable Energy and Fuels*, vol. 1, no. 7, pp. 1457–1474, 2017, cited By :13. [Online]. Available: www.scopus.com

[44] Y. Qiao, V. K. Punyamurtual, A. Han, and H. Lim, "Thermal-to-electric energy conversion of a nanoporous carbon," *Journal of Power Sources*, vol. 183, no. 1, pp. 403–405, 2008, cited By :35. [Online]. Available: www.scopus.com

[45] H. Lim, W. Lu, X. Chen, and Y. Qiao, "Effects of ion concentration on thermally-chargeable double-layer supercapacitors," *Nanotechnology*, vol. 24, no. 46, 2013, cited By :16. [Online]. Available: www.scopus.com

[46] H. Lim, Y. Shi, and Y. Qiao, "Thermally chargeable supercapacitor based on nickel-coated nanoporous carbon," *International Journal of Green Energy*, vol. 15, no. 2, pp. 53–56, 2018, cited By :5. [Online]. Available: www.scopus.com

[47] M. Bonetti, S. Nakamae, B. T. Huang, T. J. Salez, C. Wiertel-Gasquet, and M. Roger, "Thermoelectric energy recovery at ionic-liquid/electrode interface," *Journal of Chemical Physics*, vol. 142, no. 24, 2015, cited By :27. [Online]. Available: www.scopus.com

[48] S. L. Kim, H. T. Lin, and C. Yu, "Thermally chargeable solid-state supercapacitor," *Advanced Energy Materials*, vol. 6, no. 18, 2016, cited By :42. [Online]. Available: www.scopus.com

[49] M. Gouy, "Sur la constitution de la charge électrique à la surface d'un électrolyte," *J. Phys. Theor. Appl.*, vol. 9, no. 1, pp. 457–468, 1910.

[50] D. L. Chapman, "Li. a contribution to the theory of electrocapillarity," *The London, Edinburgh, and Dublin philosophical magazine and journal of science*, vol. 25, no. 148, pp. 475–481, 1913.

[51] E. Hückel, "Zur theorie der elektrolyte," in *Ergebnisse der exakten naturwissenschaften*. Springer, 1924, pp. 199–276.

[52] A. Hartel, "Structure of electric double layers in capacitive systems and to what extent (classical) density functional theory describes it," *Journal of Physics Condensed Matter*, vol. 29, no. 42, 2017, cited By :15. [Online]. Available: www.scopus.com

[53] C. Merlet, D. T. Limmer, M. Salanne, R. Van Roij, P. A. Madden, D. Chandler, and B. Rotenberg, "The electric double layer has a life of its own," *Journal of Physical Chemistry C*, vol. 118, no. 32, pp. 18 291–18 298, 2014, cited By :138. [Online]. Available: www.scopus.com

[54] J. J. López-García, J. Horno, and C. Grosse, "Differential capacitance of the diffuse double layer at electrode-electrolyte interfaces considering ions as dielectric spheres: Part i. binary electrolyte solutions," *Journal of colloid and interface science*, vol. 496, pp. 531–539, 2017, cited By :19. [Online]. Available: www.scopus.com

[55] J. N. Agar, C. Y. Mou, and J. . Lin, "Single-ion heat of transport in electrolyte solutions. a hydrodynamic theory," *Journal of Physical Chemistry*, vol. 93, no. 5, pp. 2079–2082, 1989, cited By :91. [Online]. Available: www.scopus.com

[56] E. D. Eastman, "Thermodynamics of non-isothermal systems," *Journal of the American Chemical Society*, vol. 48, no. 6, pp. 1482–1493, 1926, cited By :53. [Online]. Available: www.scopus.com

[57] B. E. Conway, "Ionic hydration in chemistry and biophysics," 1981.

[58] R. F. Stout and A. S. Khair, "Diffuse charge dynamics in ionic thermoelectrochemical systems," *Physical Review E*, vol. 96, no. 2, 2017, cited By :13. [Online]. Available: www.scopus.com

[59] S. Di Lecce, T. Albrecht, and F. Bresme, "A computational approach to calculate the heat of transport of aqueous solutions," *Scientific Reports*, vol. 7, 2017, cited By :14. [Online]. Available: www.scopus.com

[60] M. Janssen, E. Griffioen, P. M. Biesheuvel, R. Van Roij, and B. Erné, "Coulometry and calorimetry of electric double layer formation in porous electrodes," *Physical Review Letters*, vol. 119, no. 16, 2017, cited By :13. [Online]. Available: www.scopus.com

[61] M. Janssen and R. Van Roij, "Reversible heating in electric double layer capacitors," *Physical Review Letters*, vol. 118, no. 9, 2017, cited By :20. [Online]. Available: www.scopus.com

[62] S. A. Putnam and D. G. Cahill, "Transport of nanoscale latex spheres in a temperature gradient," *Langmuir*, vol. 21, no. 12, pp. 5317–5323, 2005, cited By :113. [Online]. Available: www.scopus.com

[63] M. Janssen and M. Bier, "Transient response of an electrolyte to a thermal quench," *Physical Review E*, vol. 99, no. 4, 2019, cited By :5. [Online]. Available: www.scopus.com

[64] A. Majee and A. Würger, "Collective thermoelectrophoresis of charged colloids," *Physical Review E - Statistical, Nonlinear, and Soft Matter Physics*, vol. 83, no. 6, 2011, cited By :36. [Online]. Available: www.scopus.com

[65] C. J. D. Fell and H. P. Hutchison, "Diffusion coefficients for sodium and potassium chlorides in water at elevated temperatures," *Journal of Chemical and Engineering Data*, vol. 16, no. 4, pp. 427–429, 1971, cited By :47. [Online]. Available: www.scopus.com

[66] O. S. Burheim, M. Aslan, J. S. Atchison, and V. Presser, "Thermal conductivity and temperature profiles in carbon electrodes for supercapacitors," *Journal of Power Sources*, vol. 246, pp. 160–166, 2014, cited By :17. [Online]. Available: www.scopus.com

[67] "www.engineeringtoolbox.com," 2020. [Online]. Available: https://www.engineeringtoolbox.com/water-liquid-gas-thermal-conductivity-temperature-pressure-d_2012.html

[68] D. H. Gadani, V. A. Rana, S. P. Bhatnagar, A. N. Prajapati, and A. D. Vyas, "Effect of salinity on the dielectric properties of water," *Indian Journal of Pure and Applied Physics*, vol. 50, no. 6, pp. 405–410, 2012, cited By :65. [Online]. Available: www.scopus.com

[69] K. Rah and B. C. Eu, "Theory of the thermal conductivity of molecular liquids: Nitrogen and carbon dioxide," *Journal of Chemical Physics*, vol. 117, no. 9, pp. 4386–4398, 2002, cited By :17. [Online]. Available: www.scopus.com

[70] A. Pinkert, K. L. Ang, K. N. Marsh, and S. Pang, "Density, viscosity and electrical conductivity of protic alkanolammonium ionic liquids," *Physical Chemistry Chemical Physics*, vol. 13, no. 11, pp. 5136–5143, 2011, cited By :116. [Online]. Available: www.scopus.com

[71] J. Vila, P. Ginés, E. Rilo, O. Cabeza, and L. M. Varela, "Great increase of the electrical conductivity of ionic liquids in aqueous solutions," *Fluid Phase Equilibria*, vol. 247, no. 1-2, pp. 32–39, 2006, cited By :131. [Online]. Available: www.scopus.com